DEPARTMENT OF PHYSICS AND ASTRONOMY
RUPRECHT-KARLS UNIVERSITÄT HEIDELBERG

Master Thesis in Physics
submitted by

MICHAEL DEHABE

born in Freudenstadt (Germany)

2016

CREATING AN OPTICAL MICROTRAP WITH TUNABLE ASPECT RATIO FOR ULTRACOLD FERMIONS

This Master Thesis has been carried out by

MICHAEL DEHABE

at the Physikalisches Institut, under the supervision of

PROF. DR. SELIM JOCHIM

Michael Dehabe: *Creating an optical microtrap with tunable aspect ratio for ultracold Fermions,* © 27 September 2016. (v160929, rev1)

EXAMINERS:
Prof. Dr. Selim Jochim
JProf. Dr. Fred Jendrzejewski

ADDRESS:
Physikalisches Institut
Im Neuenheimer Feld 226
69120 Heidelberg

ABSTRACT

In our experiment, we explore strongly correlated many-body systems of fermionic Lithium in optical potentials. Now, we want to study the emergence of the Anderson orthogonality catastrophe in the crossover from few to many in 1D. We can already prepare few Fermions in the ground state of the optical dipole potential of a focussed Gaussian beam. Such a system is one-dimensional, if the confinement of the elongated trap is much tighter in the radial directions than in the axial direction. However, in the current trap only up to five Fermions can be prepared in the 1D regime. In this thesis, we present and analyse a method, to dynamically increase the aspect ratio of the trap, by truncating the Gaussian beam prior to focussing. We have studied the changes of the profile and its properties depending on the truncation, theoretically and experimentally by measuring intensity profiles in 3D. We have shown, that the aspect ratio can be increased in a controlled way, as expected. For truncation ratios below 0.2, anharmonicites in the axial profile and diffraction patterns emerge, yet both seem negligible for the intended aspect ratios of 10–20 (i. e. truncation ratios around 0.5). This scheme can be used in future experiments to study the emergence of orthogonality in 1D.

ZUSAMMENFASSUNG

Mit unserem Experiment erforschen wir stark korrelierte Vielteilchensysteme mit fermionischem Lithium in optischen Potentialen. Nun wollen wir die Entstehung von Andersons Orthogonalitätskatastrophe im Übergang von wenigen zu vielen Teilchen in 1D untersuchen. Wir können wenige Fermionen im Grundzustand des optischen Dipolpotentials eines fokussierten Gaußschen Strahls präparieren. Ein solches System gilt als eindimensional, wenn die längliche Falle in den radialen Achsen viel stärker eingeengt ist, als in der axialen. Allerdings, können wir in der aktuellen Falle nur bis zu fünf Fermionen in 1D präparieren. In der vorliegenden Arbeit, untersuchen wir eine Methode, die das Aspektverhältnis der Falle dynamisch vergrößert, indem der Gaußsche Strahl vor dem Fokussieren abgeschnitten wird. Die Änderung des Potentials und dessen Eigenschaften in Abhängigkeit vom Abschneiden wurde theoretisch und experimentell untersucht, letzteres durch Messung des Intensitätsprofils in 3D. Wir konnten dabei zeigen, dass sich das Aspektverhältnis auf diese Weise wie erhofft kontrolliert vergrößern lässt. Für Abschneideverhältnisse kleiner als 0.2 wird das axiale Profil anharmonisch und Beugungseffekte nehmen zu. Jedoch erscheinen diese vernachlässigbar für die angestrebten Aspektverhältnisse von 10–20 (also Abschneideverhältnisse um 0.5). Diese Methode kann in Zukunft eingesetzt werden, um die Entstehung der Orthogonalität in 1D zu untersuchen.

Progress lies not in enhancing what is, but in advancing toward what will be.

— Khalil Gibran, *A Handful of Sand on the Shore*

ACKNOWLEDGMENTS

Ich möchte mich bei allen bedanken, die mir während des gesamten Studiums beistanden und mich stets unterstützten. Insbesondere der *Helmut Fischer Stiftung* bin ich für ihre finazielle Unterstützung über mein ganzes Studium hinweg zu Dank verpflichtet; deren Stipendium hat mir erst das Studium in dieser Form ermöglicht.

Ich bedanke mich bei Selim und der gesamten Arbeitsgruppe, dass sie mich so herzlich aufnahmen. Hierbei gilt ein besonderer Dank Andrea für ihre fortwährende Geduld und unermüdliche Hilfe – inbesondere in der letzten Phase meiner Masterarbeit.

Meinen Freunden danke ich, nicht nur für all die schöne Zeit in den vergangenen Jahren, sondern auch für die Unterstützung und den Beistand in den letzten Monaten. Besonders Boris, der in letzter Zeit immer für mich da war.

Bei meiner Familie bedanke ich mich für die maßlose Unterstützung und den Rückhalt in allen Lebenslagen. Meine Familie ist für mich da, wenn ich sie brauche – immer und überall.

Und mein letzter besonderer Dank gilt Andrej, der mir seit geraumer Zeit sehr viel Kraft und Hoffnung spendet.

CONTENTS

LIST OF FIGURES

LIST OF TABLES

LISTINGS

ACRONYMS

BEC	Bose-Einstein condensation
COM	centre-of-mass
DFT	discrete Fourier transform
MOT	magneto-optical trap
NA	numerical aperture
RF	radio-frequency

1 INTRODUCTION

Many-body systems with strong interactions exhibit very interesting phenomena in many fields of physics. A famous example of such a system are high-temperature superconductors. But although they have been discovered decades ago, they still remain little understood [Qui+09]. Strong interactions lead to non-negligible correlations between all particles in the system. As a consequence, the complexity of the system grows very fast with increasing particle number, and becomes quickly far beyond the feasibility of any classical computer [Cir+12].

A concept to approach this problem was proposed by R. Feynman in 1982: the *universal quantum simulator* [Fey82]. The idea is to build an experimental quantum system that exhibits the same Hamiltonian as the problem to study. By evolving the experimental model system in time and measuring its quantum state, the desired solution of the Hamiltonian is obtained.

Major breakthroughs were the achievement of Bose-Einstein condensation (BEC) with dilute atomic gases in 1995 [And+95; Dav+95; Bra+95] and later the creation of a degenerate Fermi gas of neutral atoms in 1999 [DeM99]. It became quickly apparent, that these new systems of ultracold quantum gases are very promising quantum simulators. Their high degree of control and their variability is unsurpassed: They can be created fully decoupled from the environment, and the nature of the interaction between the neutral particles can be varied from attractive to repulsive, with the ability to tune its strength from weak to strong. Furthermore, the particles can be confined by lattices created by lasers [Gri+99], for example, to create a potential landscape, that is similar to that experienced by electrons in solid state crystals.

Interesting highly correlated systems to study are, for example, balanced two-component Fermi gases. Therefore, it is instructive to study the most simple many-body system first: a single particle immersed in a Fermi sea—the so-called *Fermi-impurity problem*, where the impurity acts as a test particle, that probes the interaction of the system. L. D. Landau studied such systems in the thirties in the context of electrons moving in a dielectric crystal [Lan33]. He introduced the concept of the *Fermi polaron*, a quasi-particle resulting from the dressing of the impurity by the excitations of the surrounding particles.

In 1967, P. W. Anderson has found an interesting phenomenon arising in such a system of Fermions with a static impurity [And67]: The ground-state wave function of the system with interaction between the impurity and the Fermi sea, consisting of an infinite number of Fermions, becomes orthogonal to the wave function of the same system without interaction. Intriguingly, this orthogonality occurs already for infinitesimally small interaction strengths. Later it became apparent, that systems exist for which the orthog-

onality catastrophe does not require a *static* impurity. In one dimension, an orthogonality emerges, when the impurity has the same mass as the particles forming the Fermi sea [Lev+15].

But how does this *Anderson orthogonality catastrophe* arise? The overlap of the two ground state wave functions with and without interaction does not vanish in systems with only a few particles interacting with the impurity. Both limiting cases, the few-Fermion and the many-body system with infinitely many particles, can be described theoretically very well. Yet, it is completely unclear, how the system develops in this *crossover from few to many*.

In our experiment, we are able to deterministically prepare a system of few Fermions and increase the number atom by atom [Wen+13]. Therefore, we have the experimental prerequisites to study the development of a system in the crossover from few to many. To study the emergence of the orthogonality catastrophe, it only remains to ensure a quasi-one-dimensional system through this crossover.

The particles in our experiment are confined in the optical dipole potential of a tightly focussed infrared laser beam. This *microtrap* can be considered one-dimensional, as long as two degrees of freedom are frozen out [Idz+06].

The aspect ratio of the trap in the current setup allows only to prepare at most five particles in the one-dimensional regime. The aim of this thesis is to introduce and characterize a method, which allows to increase the aspect ratio dynamically without altering the setup. The basic idea behind it is the truncation of the laser beam prior to focussing. Hereby reducing the incident size will increase the size at the focus, leading to a larger aspect ratio. Hence, we can use our experimental apparatus, that ensures the deterministic preparation of few Fermions with high-fidelity, and change the aspect ratio to the desired value. In the following, the properties of the resulting trap due to this method are studied and discussed in detail.

We will start this thesis with the theoretical discussion of few-Fermion systems, with regard to the impurity problem and the orthogonality catastrophe. We will have a closer look at two particles in a harmonic trap, as this system is analytically solvable and gives crucial physical insights, despite its simplicity. In Chapter 3, the preparation of the few-Fermion system in our *microtrap* and methods to study it are presented, according to the current status of the experiment.

Then, we present the studies of this thesis in the two subsequent chapters. Firstly, we introduce in Chapter 4 the method to elongate our microtrap by truncating the beam creating it, in order to enable the preparation of more atoms in the 1D regime. Then, numerical simulations are discussed, that predict how the shape and the properties of the trap change, depending on the truncation. By experimentally measure and characterize the focussed truncated beam, its actual properties are finally compared to the theoretical expectations. These experimental measurements, we summarize in Chapter 5.

2

THE EMERGENCE OF ORTHOGONALITY IN FEW FERMION SYSTEMS

In the introduction we have presented strongly interacting many-body systems as a source of interesting phenomena. To get physical insight into such strongly correlated systems, we want to study the most simple example, the so-called *Fermi impurity problem*. This system consists of a single particle, the *impurity*, that is immersed into a gas of infinitely many non-interacting Fermions, which is referred to as *Fermi sea*. The type and the strength of the interaction between impurity and Fermi sea will clearly change the properties system.

The Hamiltonian of the three-dimensional impurity system of N particles with mass m, interacting with an impurity of the same mass, is given by

$$H = \sum_{i=0}^{N} \left[-\frac{\hbar^2}{2m} \nabla^2_{\boldsymbol{r}_i} + V_{\text{trap}}(\boldsymbol{r}_i) \right] + \sum_{i=1}^{N} V_{\text{int}}(\|\boldsymbol{r}_i - \boldsymbol{r}_0\|), \tag{2.1}$$

where $i = 0$ in the summations denotes the impurity, $V_{\text{trap}}(\boldsymbol{r})$ the potential in which the particles are confined[1], and $V_{\text{int}}(\|\boldsymbol{r}\|)$ the interaction potential between the impurity and each of the surrounding particles, that is assumed to depend only on the relative distance between two interacting particles.

[1] *The impurity feels the same potential as the other constituents. It is usually harmonic.*

The interaction term makes this Hamiltonian generally unsolvable. If the interactions were very weak, one could treat the interaction simply with perturbation theory. However, we are interested in strong interactions, where this approximation is not applicable. Only for the case of two particles (i. e. $N = 1$) in a harmonic trapping potential an analytic solution exists [Bus+98; Idz+06]. We will later present the theoretical description of this system, as it gives important insight into the physics of these systems.

In the following, we will briefly discuss a phenomenon, which allows to study the Fermi impurity problem.

2.1 THE ORTHOGONALITY CATASTROPHE

In the late sixties, P. W. Anderson described in his seminal works on the Fermi impurity problem an unexpected phenomenon that emerges in such a system [And67]. Immersing a static impurity into a Fermi sea changes the system substantially: the ground state wave function of the system becomes orthogonal to that without interaction between impurity and Fermi sea. This orthogonality emerges even for infinitesimally small interaction strengths. Nowadays, this effect is referred to as *Anderson orthogonality catastrophe*.

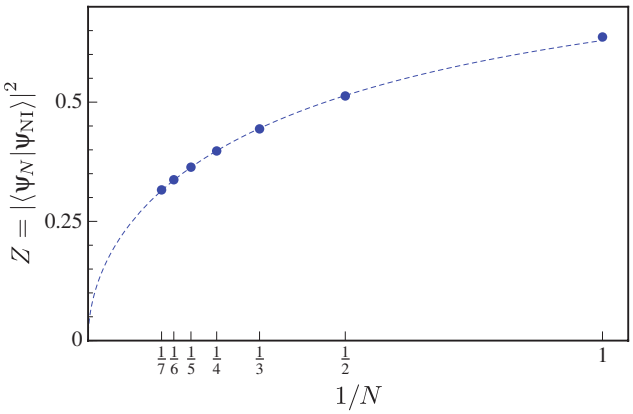

FIGURE 2.1: *Emergence of the orthogonality catastrophe in* 1*D.* When immersing an impurity into a system of N non-interacting Fermions, the quasi-particle residue Z vanishes in the limit $N \to \infty$ for strong interactions between the impurity and the surrounding particles. The quasi-particle residue is defined as the squared overlap of the ground state wave function of the system with interaction to the same system without interaction between impurity and the other constituents. This phenomenon is referred to as *orthogonality catastrophe.* Taken from [Lev+15, p. 6].

Due to this phenomenon, the squared overlap of the ground state wave functions of the system with and without interaction is defined as a quantity called *quasi-particle residue* Z:

$$Z = \|\langle \psi_{\mathrm{NI}} \mid \psi_{\mathrm{I}} \rangle\|^2 , \tag{2.2}$$

where ψ_{NI} represents the ground state wave function of the *non-interacting* and ψ_{I} of the interacting system.

2.1.1 *Orthogonality in one-dimensional systems*

Anderson's early calculations were done for a three-dimensional gas. In that case, orthogonality emerges for any interaction, yet only with a static impurity. Later, it was found that even systems with a light impurity can exhibit an orthogonality catastrophe: In one dimension, it emerges in the impurity system, if the impurity has the same mass as the particles, that form the Fermi sea [Lev+15].

Intriguingly, the quasi-particle residue does not vanish, if the impurity interacts with only a finite number of constituents instead of a Fermi sea. Yet, it is not clear, how the system evolves in the crossover from few to many-body systems, and how the orthogonality catastrophe emerges.

For infinitely strong interactions in one-dimension, the Fermi impurity system has been described theoretically in a recent work by J. Levinsen et al. [Lev+15]. It allows to calculate the quasi-particle residue for this special case, depending on the number N of Fermions in the system interacting with the impurity, which are referred to as *majority particles* (see Figure 2.1).

Our experiment allows the deterministic preparation of few-Fermion systems in a three-dimensional elongated trap. We are able to prepare imbal-

anced mixtures of different spin-species of fermionic atoms with tunable interaction between the species. In other words, we have the experimental prerequisites to study the emergence of the orthogonality catastrophe in the crossover from few to many-body systems. It remains to ensure, that the system behaves as if it were one-dimensional, by freezing out two degrees of freedom. In the next section, we will briefly compare the cases of two particles in a one-dimensional and in an elongated three-dimensional trap. We want to understand under which circumstances both systems behave almost equally, because we can only implement the latter experimentally, although we want to study particles in a 1D system.

2.2 TWO FERMIONS IN A HARMONIC TRAP

The simple case of two atoms in a harmonic trap can be solved analytically. This has been done for a spherically symmetric harmonic confinement [Bus+98]. Despite its simplicity, it gives important insights into the physics of interacting few-Fermion systems. Nevertheless, a fully one-dimensional harmonic trap cannot be realised experimentally. However, a three-dimensional trap can be considered one-dimensional, if two dimensions are much tighter confined than the third, such that two degrees of freedom are *frozen out*. This regime is referred to as *quasi-one-dimensional*. The case of a three-dimensional anisotropic harmonic trap can also be solved analytically [Idz+06]. Such a trap can be realized experimentally, e. g. by focussing an intense laser beam very tightly.

Systems with more than one majority particles have also been solved numerically. Though, in the following subsections, we will only discuss the simple two particle system, as it shows qualitatively the most relevant properties and effects that are crucial to understand one-dimensional few and many-body systems. A more elaborate discussion can be found in [Zür12; Wen13].

2.2.1 *Two particles in a one-dimensional harmonic trap*

We will now very briefly outline the system of two particles in a one-dimensional harmonic trap. An extensive discussion is given in [Bus+98].

We assume the particles in the degenerate Fermi gas to exhibit only contact interaction, which is modelled by a Dirac delta pseudo-potential with strength and type of the interaction being encoded in the s-wave scattering length a. The details about the interaction will be discussed in Section 3.2.1.

The Hamiltonian of the system is given as

$$H_{1D} = -\frac{\hbar^2}{2m}\left(\frac{\partial^2}{\partial z_1^2} + \frac{\partial^2}{\partial z_2^2}\right) + \frac{m}{2}\omega\left(z_1^2 + z_2^2\right) - \frac{\hbar^2}{m\, a_{1D}}\,\delta^{(1)}(z_1 - z_2), \qquad (2.3)$$

where z_1, z_2 denote the position of the first and the second particle, respectively, m the mass of the particles, ω the frequency of the harmonic trap, a_{1D} the one-dimensional s-wave scattering length, and $\delta^{(1)}(x)$ the one-dimen-

sional Dirac delta function. The Hamiltonian consists of the kinetic energies of the two particles in the first term, the harmonic trapping potential for each in the second term, and the one-dimensional contact interaction, as mentioned above, in the last term. Due to the harmonic potential and the dependence of the interaction term on the relative distance between the two particles, it can be solved by a centre-of-mass (COM) separation, with coordinates $Z = (z_1 + z_2)/2$ and $z = z_1 - z_2$, leading to a COM and a relative motion part. The former has the form of a single particle with mass $M = 2m$ in a harmonic oscillator and does not depend on the interaction. The interesting physics is in the Hamiltonian of the relative motion:

$$H_{\text{1D, rel}} = -\frac{\hbar^2}{2\mu}\frac{\partial^2}{\partial z^2} + \frac{\mu}{2}\omega z^2 + g_{\text{1D}}\,\delta^{(1)}(z), \tag{2.4}$$

with the reduced mass $\mu = m/2$ and introducing the *one-dimensional interaction strength* or *coupling strength* $g_{\text{1D}} = -\hbar^2/\mu a_{\text{1D}}$ [Ols98]. Solving the Schroedinger equation for this Hamiltonian, leads to an implicit equation relating energy and one-dimensional coupling strength [Bus+98; Idz+06]:

$$-\frac{1}{g_{\text{1D}}} = \frac{\mu}{2\hbar^2}\frac{\Gamma(-\mathcal{E}/2)}{\Gamma(-\mathcal{E}/2 + 1/2)}, \tag{2.5}$$

where $\Gamma(x)$ denotes the Euler gamma function and $\mathcal{E} = E - \hbar\omega/2$ the energy reduced by the zero-point energy. The obtained energies of different states depending on g_{1D} are plotted in Figure 2.2 (black solid line).

We denote the state with $\mathcal{E} < 0$ (i. e. $E/\hbar\omega_\parallel < 10.5$ in the plot) the *attractive branch*, which provides a bound state, and the state with $0 < \mathcal{E}/\hbar\omega_\parallel < 2$ (i. e. $10.5 < E/\hbar\omega_\parallel < 12.5$ in the plot) the *repulsive branch*[2]. The energy of the attractive branch diverges in the limit $g_{\text{1D}} \to -\infty$.

[2] *The energy scales and offsets have been adapted to the tree-dimensional case, that will be discussed in the next section.*

Now we will look at the experimentally relevant case of a cigar-shaped three-dimensional trap and compare it to the one-dimensional case.

2.2.2 *Two particles in a three-dimensional anisotropic harmonic trap*

In the experiment, we create our potential by tightly focussing a Gaussian laser beam, leading to a three-dimensional elongated trapping potential. In this section we will very shortly summarize the case of a three-dimensional anisotropic harmonic potential with two dimensions confined tighter than the third, which is approximately what we realize experimentally. A thorough discussion is given in [Idz+06].

The Hamiltonian of two particles in an anisotropic harmonic trapping potential in three dimensions has the following form:

$$H = -\frac{\hbar^2}{2m}\nabla_1^2 - \frac{\hbar^2}{2m}\nabla_2^2 + V_{\text{tr}}(\boldsymbol{r}_1) + V_{\text{tr}}(\boldsymbol{r}_2) + V_{\text{int}}(\boldsymbol{r}_1 - \boldsymbol{r}_2) \tag{2.6}$$

with trapping potential $V_{\text{tr}}(\boldsymbol{r})$ and interaction potential $V_{\text{int}}(\boldsymbol{r})$ given as

$$V_{\text{tr}}(\boldsymbol{r}) = \frac{m}{2}\left(\omega_\perp \rho^2 + \omega_\parallel z^2\right), \tag{2.7}$$

$$V_{\text{int}}(\boldsymbol{r}) = \frac{4\pi\hbar^2 a_{\text{3D}}}{m}\,\delta^{(3)}(\boldsymbol{r})\frac{\partial}{\partial r}(r\,\cdot\,), \tag{2.8}$$

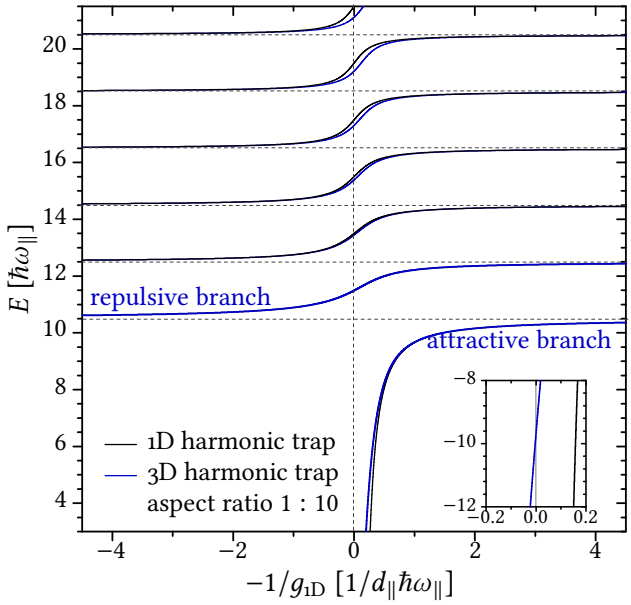

FIGURE 2.2: *Energy of two particles in a harmonic trap.* The energy of two particles in a harmonic trap is plotted depending on the inverse one-dimensional interaction strength g_{1D}. Two different theories are compared: an ideal one-dimensional trap (black) and an anisotropic three-dimensional cigar-shaped trap with aspect ratio $\eta = \omega_\perp/\omega_\parallel = 10$ (blue). The ground state energy is given as $\left(\eta + \frac{1}{2}\right)\hbar\omega_\parallel = 10.5\,\hbar\omega_\parallel$. We denote the state with $E/\hbar\omega_\parallel < 10.5$ the *attractive branch* and the state with $10.5 < E/\hbar\omega_\parallel < 12.5$ the *repulsive branch.* Taken from [Zür12, p. 49] and adapted.

where $\omega_\perp, \omega_\parallel$ are the trapping frequency in radial and axial direction, respectively, a_{3D} the three-dimensional s-wave scattering length, and $\delta^{(3)}(\boldsymbol{r})\frac{\partial}{\partial r}(r\,\cdot)$ the regularized Dirac delta pseudo-potential[3] [Hua+57; Bus+98; Ols98].

[3] *The regularisation is necessary in the three-dimensional case to avoid unphysical divergences in the limit $r \to 0$.*

Analogous to the one-dimensional case, this Hamiltonian can be separated into a COM and a relative motion part with coordinates $\boldsymbol{r} = \boldsymbol{r}_1 - \boldsymbol{r}_2$ and $\boldsymbol{R} = (\boldsymbol{r}_1 + \boldsymbol{r}_2)/2$:

$$H_{\mathrm{COM}} = -\frac{\hbar^2}{2M}\nabla_R^2 + \frac{M}{m}V_{\mathrm{tr}}(\boldsymbol{R}), \tag{2.9}$$

$$H_{\mathrm{rel}} = -\frac{\hbar^2}{2\mu}\nabla_r^2 + \frac{\mu}{m}V_{\mathrm{tr}}(\boldsymbol{r}) + V_{\mathrm{int}}(\boldsymbol{r}), \tag{2.10}$$

with $\mu = m/2$ and $M = 2m$ reduced and total mass, respectively.

Comparable to the one-dimensional system, H_{COM} equals to the Hamiltonian of a single particle with mass M in the three-dimensional harmonic oscillator, and the non-trivial physics is encoded in H_{rel}. For elongated, cigar-shaped traps, i. e. for potentials with an *aspect ratio* $\eta = \omega_\perp/\omega_\parallel \gg 1$, the solution of the Hamiltonian leads to a relation between the energy of the system and the scattering length a_{3D}:

$$-\frac{1}{a_{3D}} = \sqrt{\eta}\,\zeta_{\mathrm{H}}\left(\tfrac{1}{2}, 1 - \tfrac{\mathcal{E}}{2\eta}\right) + \eta\,\frac{\Gamma(-\mathcal{E}/2)}{\Gamma(-\mathcal{E}/2 + 1/2)}, \tag{2.11}$$

where $\mathcal{E} = E - E_0$ denotes the energy shifted by the zero-point oscillation energy $E_0 = \frac{1}{2}\hbar\omega_\parallel + \hbar\omega_\perp$ and $\zeta_{\mathrm{H}}(s, a)$ the Hurwitz zeta function.

The system behaves *quasi-one-dimensionally*, when the trap exhibits a large aspect ratio η and when $|\mathcal{E}|/\hbar\omega_\parallel \ll \eta$. I. e. when the energy of the particles is well below the energy of the first radial excitation, such that the particles effectively do not „feel" the radial dimensions, naively speaking. In order to be able to compare the energies of the one-dimensional trap with the quasi-one-dimensional, cigar-shaped trap, we need a relation between the two coupling strengths. With this assumption, expression (2.11) can be approximated further, so that a comparison with equation (2.5) leads to the following mapping between a_{3D} and g_{1D}: [Bus+98; Idz+06; Ber+03; Ols98; Bol+03]

$$g_{1D} = \frac{2\hbar^2 a_{3D}}{\mu d_\perp^2} \frac{1}{1 + \zeta(1/2)\, a_{3D}/d_\perp}, \tag{2.12}$$

with $d_\perp = \sqrt{\hbar/(\mu\omega_\perp)}$ and $\zeta(x)$ being the Riemann zeta function. This approximation holds for our case, however, it is not generally applicable. For details, see [Idz+06].

Using this relation, one-dimensional and three-dimensional theory can be compared quantitatively. The energies of several states as a function of the one-dimensional interaction strength g_{1D} are plotted for both theories in Figure 2.2. The cigar-shaped anisotropic trap, that was used for the calculation, has an aspect ratio $\eta = 10$ with a ground state energy $E_0 = \left(\eta + \frac{1}{2}\right)\hbar\omega_\parallel = 10.5\,\hbar\omega_\parallel$. In the experiment this will be different, depending on the aspect ratio. Without the changes, suggested in this thesis, the current aspect ratio is $\eta \approx 5$.

This example shows excellent agreement between 1D and 3D theory for the repulsive branch. The relative deviation is less than 1 % [Zür12, pp. 49 sq.]. This proves, that for an aspect ratio $\eta = 10$, we are already in a quasi-one-dimensional regime, where the repulsive branch can be well approximated by the 1D theory. However, there is an important, physical difference between both theories: For $g_{1D} \to -\infty$, the energy of the attractive branch diverges in the 1D theory but in the 3D theory it approaches a finite value (inset of Figure 2.2). As a consequence, the 3D theory exhibits a bound state for interactions $g_{1D} > 0$.

We can conclude, that the aspect ratio determines how well the system is described by 1D theory. High aspect ratios and energies below the energy of the first radial excitation ensure 1D physics. We refer to quasi-one-dimensional systems. Nevertheless, we have to keep in mind, that this is only for two particles true. For more particles, the deviation between both theories increases (see e. g. [Wen13]).

In the following chapter, we will discuss the experimental techniques to prepare a few Fermion system in an elongated, quasi-dimensional trap and to study the emergence of the Anderson orthogonality catastrophe.

3

EXPERIMENTAL METHODS TO PREPARE AND STUDY FEW-FERMION SYSTEMS

In this chapter, we present our experimental techniques to prepare the desired Fermi impurity system in a quasi-one-dimensional trap and to study the Anderson orthogonality catastrophe. Firstly, a method of experimentally measuring the quasi-particle residue is outlined, which allows to experimentally observe the emergence of the orthogonality catastrophe. Our experiment allows to deterministically prepare a spin-imbalanced few-Fermion system with high-fidelity. How this is done, we summarize in the second section. And finally, we will discuss the creation and the properties of the trap confining the few-Fermion system and the limitations it exhibits, that have lead to the studies of this thesis.

3.1 MEASUREMENT OF THE QUASI-PARTICLE RESIDUE

In this section, we will outline very briefly, how the quasi-particle residue can be experimentally measured, in order to study the emergence of the Anderson orthogonality catastrophe.

As discussed in Section 2.1, the quasi-particle residue is given by the overlap of the ground state wave function of the impurity system with and without interaction between impurity and majority particles. The idea to measure this observable is to drive a transition from the state with into a state without interaction—or vice versa[4]. The quasi-particle residue will then be encoded in the properties of this driven transition, as we will see momentarily.

[4] *For simplicity we will assume a transition from interacting to non-interacting.*

The starting point is a mixture of two fermionic species, i. e. an impurity and N majority particles in two different hyperfine states of a fermionic atom. In the initial state, these two species do interact. As a consequence, the energy of the system has additionally a contribution E_{int} due to this interaction. Then the impurity is excited into another hyperfine state, in which it does not interact with the majority particles. Such transitions between hyperfine states can be driven by radio-frequency (RF) fields.

3.1.1 *Rabi oscillations*

To describe the transition of the impurity, we approximate it by an atomic two-state system with the initial state $|\,\mathrm{i}\,\rangle$ and the final state $|\,\mathrm{f}\,\rangle$, with the energies $\hbar\omega_{\mathrm{i}}$ and $\hbar\omega_{\mathrm{f}}$, respectively. For brevity, we assume $\omega_{\mathrm{f}} > \omega_{\mathrm{i}}$ and define the resonance frequency $\omega_0 = \omega_{\mathrm{f}} - \omega_{\mathrm{i}}$.

For the time being, we neglect the majority particles and treat the „isolated“ impurity particle, i. e. in both states it does not interact with other particles. The interaction we will reintroduce later on.

By applying an RF field of frequency ω close to the resonance ω_0, i. e. an oscillating magnetic field, the two states are coupled, leading to the state

$$|\Psi\rangle(t) = c_\mathrm{i}\,\mathrm{e}^{-\mathrm{i}\omega_\mathrm{i}t}\,|\,\mathrm{i}\,\rangle + c_\mathrm{f}\,\mathrm{e}^{-\mathrm{i}\omega_\mathrm{f}t}\,|\,\mathrm{f}\,\rangle\,. \tag{3.1}$$

The field contributes to the Hamiltonian of the system as a time-dependent potential $V_\mathrm{RF}(t)$. Solving the Schrödinger equation, which is usually done by applying the *rotating wave approximation*, i. e. neglecting „fast oscillating“ terms with $\exp\big(-\mathrm{i}\,(\omega_0+\omega)t\big)$, leads to so-called *Rabi oscillations* between the two states. A detailed discussion is beyond the scope of this thesis and can be found in various textbooks, etc. (e. g. [Met+02; Sak+11; Ket+08]).

The frequency of the oscillation is called *Rabi frequency* and is in the case of resonance proportional to the transition matrix element of the magnetic RF transition:

$$\Omega_\mathrm{ff} \propto \left\langle\,\mathrm{f}\,\middle|\,\hat{M}_\mathrm{RF}\,\middle|\,\mathrm{i}\,\right\rangle. \tag{3.2}$$

The index „ff“ is the abbreviation of „free-free“ and indicates that we are currently considering the isolated impurity, without interaction to any other particles in both states. The RF field couples only to the hyperfine structure of the atom, i. e. the „spin“ degree of freedom, such that

$$\Omega_\mathrm{ff} \propto \left\langle\,\xi_\mathrm{f}\,\middle|\,\hat{M}_\mathrm{RF}\,\middle|\,\xi_\mathrm{i}\,\right\rangle\langle\,\psi_\mathrm{f}\,|\,\psi_\mathrm{i}\,\rangle\,, \tag{3.3}$$

where $|\,\xi_k\,\rangle$ denotes the hyperfine structure part and $|\,\psi_k\,\rangle$ the spatial part of the state $|\,k\,\rangle = |\,\psi_k\,\rangle \otimes |\,\xi_k\,\rangle$. In other words, the Rabi frequency is proportional to the overlap of the spatial wave functions of the two states.

When considering the transition between two hyperfine states, that do not differ in the n, j, and l quantum numbers, the spatial wave function is the same for both. In this case, the spatial overlap becomes $\langle\,\psi_\mathrm{f}\,|\,\psi_\mathrm{i}\,\rangle = 1$, leading to

$$\Omega_\mathrm{ff} \propto \left\langle\,\xi_\mathrm{f}\,\middle|\,\hat{M}_\mathrm{RF}\,\middle|\,\xi_\mathrm{i}\,\right\rangle. \tag{3.4}$$

This is sensible, because we prepare mixtures of the lowest hyperfine states of the ground state of ^{6}Li, in our experiment, as we will see in the next section.

Now, we consider the case of the impurity interacting with surrounding particles in the initial state. This changes the properties of the RF transition. The interaction energy E_int shifts the energy of the initial state and thus also the resonance frequency to $\omega_0' = \omega_0 + E_\mathrm{int}/\hbar$. Although the interaction does not affect the inner degrees of freedom of the impurity particle, i. e. its hyperfine wave function, it changes the spatial wave function. Therefore, the Rabi frequency becomes

$$\begin{aligned}\Omega' &\propto \left\langle\,\xi_\mathrm{f}\,\middle|\,\hat{M}_\mathrm{RF}\,\middle|\,\xi_\mathrm{i}\,\right\rangle\left\langle\,\psi_\mathrm{f}\,\middle|\,\psi_\mathrm{i}'\,\right\rangle \\ &= \Omega_\mathrm{ff}\left\langle\,\psi_\mathrm{f}\,\middle|\,\psi_\mathrm{i}'\,\right\rangle.\end{aligned} \tag{3.5}$$

Recalling the definition (2.2) of the *quasi-particle residue* Z, we obtain

$$Z = |\Omega'/\Omega_{\mathrm{ff}}|^2 . \tag{3.6}$$

Hence, the quasi-particle residue of an impurity system with N majority particles can be experimentally obtained, by measuring and comparing the Rabi oscillation of the transition of the impurity into a non-interacting hyperfine state with the same transition of the isolated impurity.

In the following section, we will now present our experimental methods to prepare such a system.

3.2 DETERMINISTIC PREPARATION OF FEW FERMIONS

In our experiment, we prepare an ultracold sample of fermionic ^{6}Li. One of its most important features, that is necessary to have a highly controllable quantum system, is the tunable interaction strength due to a broad magnetic *Feshbach resonance*.

To deterministically prepare a few-Fermion system, we need a procedure, that allows us to control the final number of particles in the trap with high precision. Furthermore, it is crucial, that the system is prepared in the ground state of the trap.

To achieve these requirements, we prepare a very dilute atomic gas at low temperature (i. e. in the nanokelvin regime) in an optical trap, such that the fermionic occupation probability of the lowest energy states in the trap approaches unity. The probability is given by the Fermi-Dirac distribution

$$P(E) = \frac{1}{\exp\left((E-\mu)/k_{\mathrm{B}}T\right)+1}, \tag{3.7}$$

where μ denotes the chemical potential, k_{B} the Boltzmann constant and, T the temperature of the sample. Having prepared a *degenerate Fermi gas* in the trap, the particle number is reduced by applying a magnetic gradient and fine-tuning the trap depth to *spill out* all atoms in the higher excited states. This requires the trap depth to be controlled with much more precision than the energy level spacing of the trap. When finally the few Fermion system is prepared, it has to be probed as well. A single particle detection method ensures that the particle number is measured with high fidelity.

After summarizing the important properties of ^{6}Li in the next subsection, we will discuss the preparation in more detail.

3.2.1 *General properties of fermionic Lithium*

Lithium is the first element in the group of Alkali metals, and therefore the most simple one. It has a single unpaired valence electron, corresponding to a half-filled s-shell, leading to a total angular momentum of $J = S = 1/2$. As we need Fermions in our experiments, we use the fermionic isotope ^{6}Li.

TABLE 3.1: *Position and width of the Feshbach resonances for mixtures of the three lowest hyperfine states of ^6Li.* Taken from [Zür+13].

Mixture	Resonance position B [G]	Width ΔB [G]
$\vert 1\rangle - \vert 2\rangle$	832.18 ± 0.08	262.3 ± 0.3
$\vert 1\rangle - \vert 3\rangle$	689.68 ± 0.08	166.6 ± 0.3
$\vert 2\rangle - \vert 3\rangle$	809.76 ± 0.05	200.2 ± 0.5

It has a nuclear spin of $I = 1$. The optical transition used for the preparation, that will be discussed in the following subsection, is between the states $2\,^2S_{1/2}, F = 3/2$ and $2\,^2P_{3/2}$ which is known as $D2$-line with a wavelength $\lambda = 670.977\,\text{nm}$ and a natural line width $\Gamma_{D2} = 5.87\,\text{MHz}$ [Geho3]. The ground state of ^{6}Li is $2\,^2S_{1/2}$, it splits into the six hyperfine states $F = 1/2, m_F = \pm 1/2$ and $F = 3/2, m_F = \pm 1/2, \pm 3/2$. While most of these states are degenerate, applying a magnetic background field leads to a *Zeeman splitting* into two triplets at high magnetic fields above ~100 G (i. e. in the *Paschen-Back regime*), as electronic and nuclear spin decouple. According to convention, these states are named from $\vert 1\rangle$ to $\vert 6\rangle$ with increasing energy. For our experiment, only the three lowest, i. e., $\vert 1\rangle$, $\vert 2\rangle$, and $\vert 3\rangle$, are relevant, because only mixtures of these are stable against collisions.

3.2.1.1 *Feshbach resonances*

As already mentioned, we work with a very dilute fermionic gas at extremely low temperatures—i. e. a degenerate Fermi gas. The de Broglie wavelength of particles in such a system is much larger than the interparticle spacing. As a consequence, only two-body collisions are relevant and these can be approximated by contact interactions, exp with a Dirac δ pseudo-potential as in equations (2.3) and (2.8). The strength of the interaction with this pseudo-potential is given by the s-wave scattering length a.

Crucially, the scattering length diverges at certain magnetic fields—so-called *magnetic Feshbach resonances* [Fes62]—and can be tuned from negative to positive values over these resonances by applying different magnetic fields. This allows to control type and strength of the interaction between different hyperfine states.

The Feshbach resonances for ^{6}Li with mixtures of the states $\vert 1\rangle$ to $\vert 3\rangle$ are at fields between 650 and 850 G. In Figure 3.1 the scattering lengths of the three mixtures are plotted against the magnetic offset field and Table 3.1 lists the positions of the associated resonances.

A rigorous and more thorough discussion of collisions and Feshbach resonances can be found in [Sak+11; Chi+10; Wen13] as it is beyond the scope of this thesis.

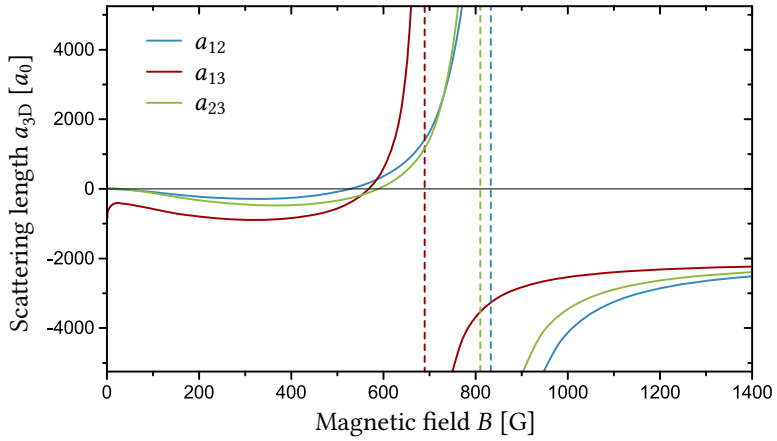

FIGURE 3.1: *Feshbach resonances for mixtures of the three lowest hyperfine states of ^{6}Li.* The scattering length a_{3D} depending on the magnetic offset field B is plotted as multiples of the Bohr radius a_0 for the possible mixtures of the three lowest Zeeman hyperfine states of ^{6}Li. The positions of the resonances are listed in Table 3.1. Taken from [Wen13, p. 30] and adapted.

3.2.2 *Preparation of an ultracold Fermi gas*

The basic techniques of preparing a degenerate Fermi gas of ^{6}Li in our experiment are extensively discussed in previous theses [Ser11; Zür12; Wen13; Ber13; Mur15]. In this section we will very shortly summarize the important steps. A sketch of the whole experimental setup is shown in Figure 3.2.

In the end, we want a sample of few Fermions in the ground state of our quasi-one-dimensional trapping potential. To reach this point, solid ^{6}Li has to be transformed into a dilute atomic gas at very low temperatures.

After being heated into an *atomic vapour* in an oven, the Lithium atoms enter the experimental vacuum chamber as an atomic beam. Before they can be captured by a *magneto-optical trap* (MOT), the atoms are slowed using a *Zeeman slower* [Met+02]. The MOT confines the gas and cools it down into the microkelvin regime. The MOT cannot cool the gas below ~200 µK, due to an inherent heating rate (*Doppler limit*). However, degeneracy requires even lower temperatures. To overcome this limitation, the atoms are transferred into a crossed-beam *optical dipole trap* [Gri+99], where the atoms are cooled down further by *evaporative cooling* [Met+02; Ket+08].

This cooling technique reduces the temperature by several orders of magnitude and thereby increases the phase space density further towards degeneracy, although it also reduces the number of particles in the sample. Eventually a sample of the order of 10^4 atoms per spin state with a degeneracy of $T/T_F \approx 0.5$ [Zür12] is obtained, where T_F denotes the Fermi temperature, which corresponds to the energy of the highest excited particle in the trap.

A high vacuum of approximately 10^{-12} mbar in the experimental chamber ensures long lifetimes of the ultracold atomic samples.

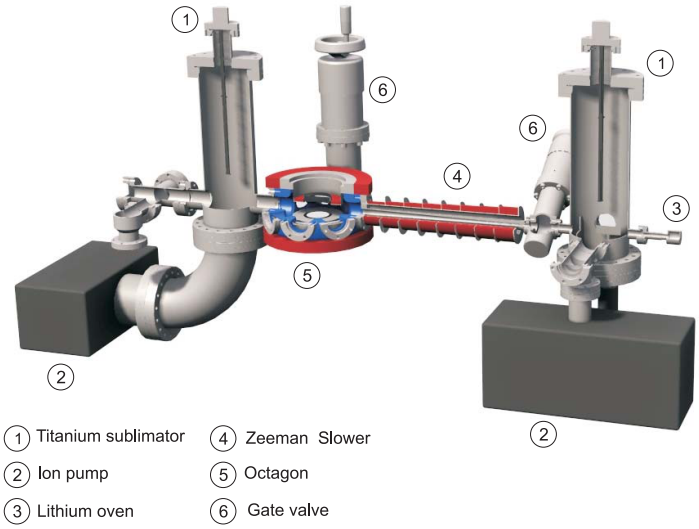

FIGURE 3.2: *The experimental system with oven and vacuum chamber.* The ^{6}Li atoms evaporated in an oven (1) enter the experimental vacuum chamber (5) as an atomic beam, after being slowed down using a Zeeman slower (4). Taken from [Ser07, p. 32].

3.2.2.1 *The dimple trick: Deterministic preparation of a degenerate Fermi gas*

The degeneracy of the sample achieved so far is not sufficient for a deterministic preparation of single particles in the ground state with high fidelity. I. e. the occupation probability of the lowest states, given by (3.7), is still to far from unity. The so-called *dimple trick* increases the degeneracy further:

The crossed-beam dipole trap, that serves as a reservoir, is superimposed with a tightly focussed laser beam. The resulting additional optical dipole trap has a much smaller volume than the reservoir, but its power is chosen such that it is much deeper. Due to its small size, we call this „dimple“ in the reservoir *microtrap*. As a consequence of the different proportions of the two traps, far less energy levels fit in the microtrap than in the reservoir. Hence, when ramped up adiabatically, the thermalisation will alter particle number and temperature only negligibly. On the other hand, the Fermi energy is governed by the depth of the microtrap, as the latter is much deeper, i. e. $T_\mathrm{F} \approx T_{\mathrm{F,\,dimple}}$, and hence the degeneracy is given as $T/T_\mathrm{F} \approx T/T_{\mathrm{F,\,dimple}} \approx 0.08$ [Ser+11], which is almost an improvement by a factor of 10. Using the Fermi-Dirac distribution (3.7), the occupation probability of the lowest state can be shown to exceed 0.9999 [Ser+11], and is thus sufficiently high.

The microtrap, that is used as a dimple to increase the degeneracy of the system, is also the quasi-one-dimensional trap, with which the 1D Fermi impurity problem is studied. We will discuss the microtrap in Section 3.3 in more detail, as it is the main object of study in this thesis.

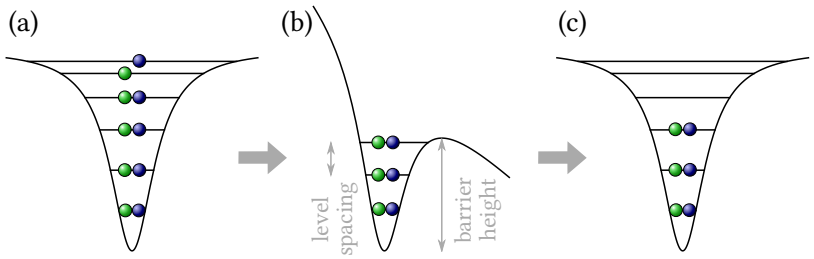

FIGURE 3.3: *Schematic of the spilling technique.* To reduce the particles of the prepared degenerate Fermi gas in the microtrap (a) to a fixed number, a linear magnetic field gradient is applied, and the trap depth is adjusted, such that the the upper states get unbound and the particles in these leave the trap (b). After turning the gradient off, the desired number of particles remains (c). Taken from [Zür12, p. 14] and adapted.

3.2.2.2 *The spilling technique: Deterministic preparation of a few Fermion system*

When the reservoir is turned off, only a few hundred bound states in the microtrap remain, which corresponds to the same number of particles in each spin state, due to the Pauli exclusion principle. The idea to prepare a fixed number of few Fermions in the trap is to control the number of states in the trap with high precision. This is achieved by modifying the potential: The optical dipole potential of the focussed beam is superimposed with the linear potential of a magnetic field gradient of $\partial B/\partial z = 31\,\mathrm{G\,cm^{-1}}$ [Ber13, pp. 53 sq.], which is produced by the *Feshbach coils*, i. e. the coils used to create the magnetic fields to tune the interaction strength via Feshbach resonances. The resulting potential is sketched in Figure 3.3, (b). As a consequence, the upper states in trap above the resulting potential barrier become unbound, and all atoms occupying these leave the trap after some time. To further fine tune the number of states, the trap depth is modified, i. e. it is reduced, such that only the wanted number of particles remain. Finally, the linear potential is turned off, and we obtain a well defined state of a fixed number of atoms with a certain fidelity. We call this method *spilling process*. The procedure results always in an even number of particles in the trap, as we are working with a two-state spin mixture and the energy levels in trap are twofold-degenerate in the spin states.

3.2.2.3 *Preparation of imbalanced few-Fermion systems*

When applying a magnetic field gradient, it couples to the magnetic moment $\boldsymbol{\mu}$ of atoms in its vicinity. The potential due to the resulting force, is given as

$$V_{\mathrm{mag}}(z) = -\boldsymbol{\mu} \cdot \boldsymbol{B}(z) = \mu \frac{\partial B}{\partial z} z. \tag{3.8}$$

At high magnetic offset fields, as used for the preceding procedure[5], the moments of both spin states are approximately equal, such that atoms in both states experience the same spilling potential explained previously. However,

[5] *To control the collisions of the spin mixture in terms of a Feshbach resonance, high magnetic offset fields are applied.*

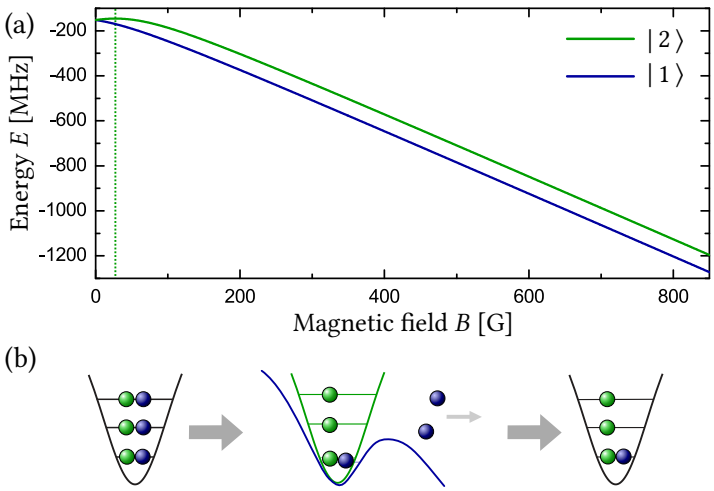

FIGURE 3.4: *Zeeman shift of the two lowest hyperfine states of ^{6}Li and schematic of the imbalanced spilling.* (a) Magnetic field dependence of the energy of the two lowest hyperfine states of ^{6}Li due to the Zeeman effect. The dotted vertical green line marks the field where the magnetic moment of state $|2\rangle$ vanishes. (b) To create an imbalanced system the magnetic offset field is chosen such that the magnetic moment of state $|1\rangle$ vanishes and therefore is not affected by the applied magnetic spilling gradient in contrast to state $|1\rangle$. Taken from [Wen13, p. 84] and adapted.

when applying low magnetic offset fields, the magnetic moments differ significantly between the two lowest hyperfine states of ^{6}Li, that are prepared. The moment for atoms in state $|2\rangle$ vanishes at a field of ~27 G as shown in the dependence of the energy on the magnetic field in Figure 3.4, (a). When this offset field is combined with another spilling, atoms in state $|2\rangle$ do not experience the additional linear potential due to the magnetic field gradient. Therefore, only atoms in state $|1\rangle$ are removed from the trap. The whole procedure is sketched in Figure 3.4, (b). Subsequent Landau-Zener passages or π-pulses allow a transfer of the populations to other hyperfine states, if necessary, such that an imbalanced few-Fermion system with the desired spin mixtures is finally obtained.

3.2.3 *High-Fidelity Single Atom Detection*

So far, we have only discussed the deterministic preparation of few-Fermion systems, but equally important is a single atom detection method with high fidelity. A common option would be absorption imaging. However, the absorption signal of single atoms is very weak, such that the signal-to-noise ratio is far to low.

The method we are using is fluorescence imaging. To finally measure the number of atoms, they are recaptured into a MOT, and the scattered photons are collected on a CCD camera. By choosing long exposure times, the number of collected photons can be increased significantly, leading to a high signal-to-noise ratio.

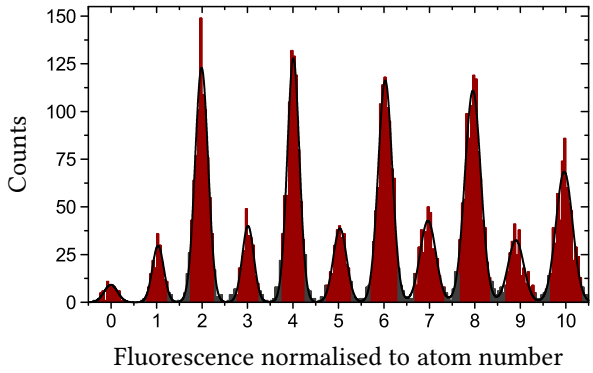

FIGURE 3.5: . The histograms for the preparation of one to eight particles in the trap have been calculated and combined in this plot. It can be seen that single particles can be distinguished with high fidelity. The measured fluorescence signal has been normalized to the measured particle number. Taken from [Ser+11, Supporting Online Material] and adapted.

To show that the different particle numbers can be distinguished unambiguously, the histograms of the detected fluorescence signal for one to eight prepared particles are shown in Figure 3.5. Each histogram is obtained by taking fluorescence images and counting the number of pixels corresponding to each value of the fluorescence signal. By doing this for the preparation of different numbers of particles, one obtains a mapping between fluorescence signal and particle number, as the signals of the different preparations are clearly distinguishable. A detailed discussion of the detection process can be found in [Ser+11, Supporting Online Material].

Currently, an alternative scheme for site-resolved single particle detection is being developed, using an EMCCD camera, as the described process discards the spatial information [Bec16].

3.3 CREATION OF THE CONFINING POTENTIAL

To study the one-dimensional Fermi impurity problem, we prepare a degenerate Fermi gas and subsequently reduce the number of particles in a controlled way. As discussed previously, a *microtrap*, produced by a tightly focussed laser beam, is used to ensure high degeneracy. But finally, it serves as the quasi-one-dimensional trap of the systems to study. In Section 2.2 we have seen, that the aspect ratio η, which is the ratio between the radial $\omega_\perp$ and the axial frequency of the trap, determines how well the system is described by one-dimensional theory.

Hence, we will discuss now the microtrap in more detail. The design of the microtrap, together with the current setup, does not allow the preparation of more than five majority atoms due to the low aspect ratio of the trap of 5. We will discuss this limitation in the next chapter. The method to remedy it, is the main part of this thesis.

TABLE 3.2: *The nominal design parameters of the high-resolution objective.* Taken from [Ser11, p. 80].

Property	$\lambda = 1064\,\mathrm{nm}$	$\lambda = 671\,\mathrm{nm}$
focal length [mm]	20.3	20.3
image distance	∞	∞
diameter field of view [µm]	200	200
max. diffraction limited NA	0.6	0.6
entrance apert. diameter at max. NA [mm]	24.4	24.4
resolution [µm]	1.08	0.68
waist of focus [µm]	0.72	0.45

3.3.1 *The high-resolution objective to create the microtrap*

A high-resolution objective is used to create the microtrap. Additionally, it is crucial for the final probing of the few-Fermion system, as it is also used to recollect the scattered photons of the fluorescence imaging (see Section 3.2.3). Therefore, it is optimized for two wavelengths: The optical potential requires the wavelength $\lambda = 1064\,\mathrm{nm}$ and the imaging $\lambda = 671\,\mathrm{nm}$. The objective was designed and tested in the context of previous theses [Ber13; Ser11]. The high numerical aperture (NA) of 0.6 ensures a very high resolution and that as many photons as possible (~10 %) can be recollected for the fluorescence imaging [Ser11, pp. 73 sq.]. Because it is placed outside of the vacuum chamber, it was designed to have an effective focal length of $f = 20.3\,\mathrm{mm}$[6]. The nominal design parameters of the objective are listed in Table 3.2.

[6] *The window of the vacuum chamber is included in the design.*

3.3.2 *Optical setup*

To ensure maximal performance of the objective and to use its whole numerical aperture, the incident beam needs a sufficiently large beam waist. The simplified optical setup, that is important for this thesis, is sketched in Figure 3.6. The first step is the power stabilisation of the laser light (not included in the sketch). A small fraction of the light is extracted and focussed onto a photodiode. The latter is connected to a feedback control loop and stabilizes the laser power within the quality of the loop. Thereafter, the beam, with an initial waist of 1.23 mm [Kli12, pp. 27 sq.], is expanded to a waist of 9.95 mm, using a telescope consisting of an aspheric lens with $f_1 = 18.5\,\mathrm{mm}$ and a spheric lens with $f_2 = 300\,\mathrm{mm}$. Finally, the beam is focussed with the objective through the window of the vacuum chamber where the microtrap is created.

Also shown is a circular aperture that truncates the beam prior to focussing. This feature will be explained in Chapter 4.

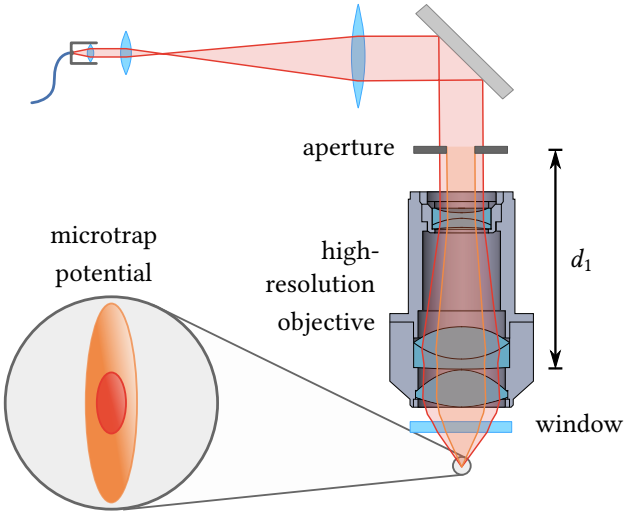

FIGURE 3.6: *Sketch of the simplified setup for the creation of the microtrap with the objective.* An incident Gaussian beam is expanded to a waist of $w_0 = 9.95\,\text{mm}$ using a telescope, truncated by a circular aperture of radius a, and finally focused by our high-resolution objective with an effective focal length $f = 20.3\,\text{mm}$. Objective and aperture are separated by a distance d_1. The effect of the truncation on the potential of the microtrap is illustrated in the inset. Based on a sketch from [Ber13, p. 33].

3.3.3 *Characterization of the focus*

Size and shape of the beam focus determine the optical dipole potential, that makes up the microtrap, and hence the physics of the whole system. Before discussing the potential in more detail in Section 3.3.4, we will estimate the size of the focus at first.

When focussing a Gaussian beam with a thin lens of focal length f, the size of the new waist is given by the magnification of the system, whithin the framework of Gaussian beam optics [Sal+07; IDE]:

$$w_0' = M w_0 \quad \text{with} \qquad (3.9)$$
$$M = \frac{1}{\sqrt{1 + (f/z_\text{R})}},$$

where w_0 denotes the waist and $z_\text{R} = \pi w_0^2/\lambda$ the Rayleigh range of the incoming beam. This naive calculation results in a beam waist at the focus of $w_0' = 0.69\,\mu\text{m}$.

If also taking the limited numerical aperture of the objective, i. e. its finite entrance aperture r_in, into account, we need to consider the truncation of the incident beam. In this case, the waist at the focus depends on the illumination of the entrance aperture, and hence [IDE]

$$w_0' = K(r_\text{in}) \frac{\lambda}{2\,\text{NA}}, \qquad (3.10)$$

where $K(r_\text{in})$ is the illumination coefficient depending on the entrance aperture radius r_in and NA the numerical aperture of the objective. For a given

truncation radius a and a Gaussian beam of waist w_0, the coefficient K is given as [IDE, p. A166]

$$K(a) = 0.82 + \frac{0.32}{(w_0/a - 0.28)^{1.82}} - \frac{0.27}{(w_0/a - 0.28)^{1.89}}. \tag{3.11}$$

Using these formulae, the expected waist at the focus results to $w_0' = 0.83\,\mu\text{m}$.

However, experimental measurements have shown, that the actual waist is around 1.2 µm and thus significantly larger than this expected value. More details on this are given in Appendix C.

3.3.4 *Optical dipole potential*

The confinement of the atoms in the microtrap is due to the optical dipole potential, that is induced by the light field of the focussed beam[7]. To grasp the physical properties of the potential, we neglect for now the finite entrance aperture of the objective and assume the beam to be ideally Gaussian[8]. Therefore, the intensity distribution has the shape [Sal+07; Gri+99]

$$I(\rho, z) = \frac{2P}{\pi w^2(z)} \exp\left(-2\frac{\rho^2}{w^2(z)}\right) \quad \text{with} \tag{3.12}$$
$$w(z) = w_0\sqrt{1 + \left(\frac{z}{z_\text{R}}\right)^2},$$

where P denotes the power of the beam, $\rho^2 = x^2 + y^2$ the radial coordinate, and z the axial coordinate along the beam propagation. The axial profile $I_\parallel(z) = I(\rho = 0, z)$ has a Lorentzian shape with half-width $2z_\text{R}$.

The optical dipole potential is related to the light intensity according to[9] [Gri+99, p. 4]

$$U_\text{dip}(\boldsymbol{r}) = -\frac{3\pi c^2}{2\omega_0^2}\left(\frac{\Gamma}{\omega_0 - \omega} + \frac{\Gamma}{\omega_0 + \omega}\right) I(\boldsymbol{r}), \tag{3.13}$$

where ω_0 denotes the atomic resonance frequency, ω the light frequency, and Γ the natural line width of the optical transition (see Section 3.2.1). The trap depth is given as $U_0 = U_\text{dip}(\rho = 0, z = 0)$.

As we prepare only a few particles in the ground state of the trap, the wave function of the system does only spread over a small region around the trap centre. Therefore, the actual potential is well described by a harmonic potential, which was also assumed for the calculations in Chapter 2, given as

$$U_{\text{dip, ho}}(\rho, z) = \frac{1}{2} m_\text{Li}\left(\omega_\perp^2\rho^2 + \omega_\parallel^2 z^2\right), \tag{3.14}$$

with m_Li the mass of ^{6}Li, and the trap frequencies $\omega_\perp^2 = 4U_0/(m_\text{Li}w_0^2)$ in radial and $\omega_\parallel^2 = 2U_0/(m_\text{Li}z_\text{R}^2)$ in axial direction. Hence, the aspect ratio of a Gaussian dipole trap is given as

$$\eta = \frac{\omega_\perp}{\omega_\parallel} = \sqrt{\frac{4U_0/(m_\text{Li}w_0^2)}{2U_0/(m_\text{Li}z_\text{R}^2)}} = \sqrt{\frac{2z_\text{R}^2}{w_0^2}} = \frac{\pi\sqrt{2}}{\lambda} w_0. \tag{3.15}$$

[7] *The light has to be red-detuned with respect to the atomic resonance frequency of ^{6}Li, if an intensity maximum should be the trapping centre [Gri+99].*

[8] *This corresponds to the* transverse electromagnetic mode *TEM_{00}.*

[9] *For brevity, we neglect the multi-level energy structure of the Alkali atoms.*

In other words, the aspect ratio of the trap increases linearly with the beam waist.

3.3.5 *Challenges and limitations*

These insights of the potential of a focussed laser beam reveal the problem of this choice to confine few-Fermion systems. Focussing an incident beam with large waist, in order to exploit the full NA of our high-resolution objective, results in a very small beam waist. As we have seen previously, this leads to small aspect ratio of the optical dipole potential. However, in Chapter 2 we have stated, that a large aspect ratio is crucial to ensure the system to be in the quasi-one-dimensional regime.

In the next chapter, we will present and discuss a method to remedy this limitation without changing the whole setup. The idea is to truncate the incident beam prior to focussing, leading to larger waist at the focus (see Figure 3.6). Nevertheless, this might lead to other questions, as it is not clear how it changes the shape of the potential. Especially, emerging anharmonicities are of concern, because they change the physical properties of the trap, like the energy spacing and the wave functions of the trapped atoms.

4

SIMULATION: FOCUSING OF A TRUNCATED GAUSSIAN BEAM

In Chapter 2, we discussed the properties of two particles in a harmonic trap—for the desired one-dimensional and the experimentally relevant three-dimensional case. Our final aim is to study 1D physics with our cigar-shaped three-dimensional trap. Hence, it is important to fulfil the conditions, discussed in Section 2.2, that are necessary to make the 3D system behave as similarly to the 1D case as possible. I. e. the trapping potential of the focussed laser beam needs an aspect ratio $\eta \gg 1$ and the number of prepared particles has to be below the aspect ratio.

Currently, the microtrap has an aspect ratio $\eta \approx 5$ due to the small waist of the beam creating it. Thus, using this microtrap at most four majority particles can be prepared, while being in the 1D regime. To advance deeper into the crossover from few to many, we must increase the aspect ratio of the trap to be able to prepare more majority particles.

We have seen in the end of the last chapter, that the aspect ratio of a Gaussian beam depends linearly on its waist, according to (3.15). Increasing the aspect ratio, requires a larger beam waist at the focus of the objective. In the following, we will discuss a method to achieve this.

4.1 A METHOD TO INCREASE THE SIZE OF A FOCUSSED BEAM

The technically most simple idea to increase the waist, is a truncation of the beam with a circular aperture prior to focussing. Naively, one would first think of just decreasing the size of the incident beam. Yet, the advantage of the truncation method is, that it allows the trap to be changed on-the-fly by just varying the aperture radius—and we want to change the aspect ratio during the experimental sequence—whereas the naive approach requires the whole optical setup to be changed. However, clipping the outer region of the incident Gaussian beam does not have the same effect as changing incident beam waist: We expect diffraction effects to emerge.

The profile at the focal plane of an imaging lens, arising from the diffraction of an aperture in front of the lens, is well known and can be easily described by theory[10] But the diffraction along the propagation of the beam (i. e. the axial axis) is highly non-trivial. There is neither an intuitive description nor a quantitative analytical expression describing the axial profile. In the end we will see, that an approximative description exist, albeit it is only valid for a special case.

To understand, how the profile—especially the aspect ratio—of the microtrap changes depending on the truncation of the beam prior to focussing, a numerical simulation has been carried out. The whole description of these

[10] *E. g. the theory of* Fraunhofer diffraction. *It gives a good qualitative and quantitative description, although several approximations are assumed.*

calculations is within the framework of *Fourier optics* which will be introduced and explained in the following.

4.2 A QUALITATIVE APPROACH TO THE DESCRIPTION OF A FOCUSSED TRUNCATED GAUSSIAN BEAM

Before we use the more elaborate theory, we want to try a simple and naive approach. In Section 3.3.3 we used already the empirical formula (3.10) together with (3.11) that gives the waist at the focal plane of a truncated Gaussian beam depending on the aperture radius a[11]. Assuming that the focussed truncated beam is still described by a Gaussian, the aspect ratio depending on the aperture radius a can be calculated according to (3.15): The aspect ratio η is then simply given as

[11] *The NA in* (3.11) *is given in this case by* $\sin(a/f)$*, with the focal length* f *and the aperture radius* a*.*

$$\eta(a) = \frac{\pi\sqrt{2}}{\lambda}\, w_0(a) = \frac{\pi\sqrt{2}}{\sin(a/f)}\, K(a), \tag{4.1}$$

where $K(a)$ is given by (3.11). The obtained aspect ratio as a function of the aperture radius a is shown in Figure 4.5 as solid line. In comparison with the results of the following exact calculations, we will see later, that this first approach can only qualitatively the describe change of the aspect ratio.

4.3 EXACT CALCULATION OF A FOCUSSED TRUNCATED GAUSSIAN BEAM

The preceding approach gives us a feeling, how the properties of the trap change due to truncation. However, it is too naive to allow more insight. Due to diffraction, it is apparent that the beam cannot keep the shape of a Gaussian after truncation.

In this section, we want to understand in detail, how the intensity profile of a focussed Gaussian beam changes around the focus, when it is truncated by a circular aperture beforehand. As already mentioned, the concept of *Fourier optics* is used and will be introduced in the following.

For the whole derivation we do not use the usual small angle approximation, i. e. $\sin\theta \approx \theta$, known as the *paraxial approximation*, because our setup is designed to use the maximal numerical aperture $\mathrm{NA} = 0.6$ of the objective. The error, when using this approximation is given as

$$\Delta = \frac{|\sin\theta - \theta|}{\sin\theta} = \frac{|\mathrm{NA} - \arcsin \mathrm{NA}|}{\mathrm{NA}} \approx 7\,\%. \tag{4.2}$$

A priori, it is not clear which deviations the approximation would have on the whole profile, on the calculated trap frequencies and on the aspect ratio. But we do not expect the paraxial approximation to yield correct results, As we are doing precision measurements, we need accurate predictions, and hence we will avoid this approximation.

In order to be able to calculate anything in our complex setup, we have to make some idealized assumptions. The high-resolution objective, that consists of several lenses and other optical components, is simulated by a

single hyperbolic thin lens in an aperture with the effective focal length of the objective. The aperture of the beam truncation is assumed to be infinitely thin, and perfectly centred and circular.

4.3.1 *Basic principles*

In Fourier optics it is assumed, that light can be described by a complex scalar field propagating in space as waves. The polarization of light and its electromagnetic nature are neglected. The important principle is the description of the propagation of light in terms of harmonic analysis—i. e. *Fourier analysis*. By treating every point of the light field as the point-like source of a spherical wave, the propagation of the whole field can be reduced to the well known propagation of spherical waves. The concept of Fourier optics is discussed in more detail in [Sal+07].

The propagator of a spherical wave in free space is simply[12]

$$H_0(\boldsymbol{\nu}_\perp; d) = \exp\left(2\pi \mathrm{i}\, d \nu_z\right) = \exp\left(2\pi \mathrm{i}\, d \sqrt{\lambda^{-2} - \nu_\perp^2}\right), \tag{4.3}$$

[12] *We assume the propagation of the field to be along the z axis.*

with $k_z = 2\pi\nu_z$ the z component of the wave vector expressed as spatial frequency ν_z and $\boldsymbol{\nu}_\perp^2 = \nu_x^2 + \nu_y^2$ the spacial frequency in the radial plane, and λ the wavelength of the light. The parameter d specifies the propagation distance.

Therefore, the procedure to calculate the field after some distance d consists of the following steps: Transforming the field into Fourier space, propagating its harmonic components according to (4.3) for a distance d, and then retransforming it into real space again. The resulting field U' at the plane $z = d$ that propagated from the incident field U at $z = 0$ is given as

$$\begin{aligned} U'(\boldsymbol{\rho}') &= \mathcal{F}^{-1}\left\{\mathcal{F}\{U\}\, H_0(;d)\right\}(\boldsymbol{\rho}') \\ &= \int \mathrm{d}\boldsymbol{\nu}_\perp\, \mathrm{e}^{2\pi\mathrm{i}\,\boldsymbol{\rho}'\cdot\boldsymbol{\nu}_\perp} H_0(\boldsymbol{\nu}_\perp; d) \int \mathrm{d}\boldsymbol{\rho}\, \mathrm{e}^{-2\pi\mathrm{i}\,\boldsymbol{\rho}\cdot\boldsymbol{\nu}_\perp} U(\boldsymbol{\rho}), \end{aligned} \tag{4.4}$$

where $\mathcal{F}(f)$ denotes the Fourier transform of f and $\boldsymbol{\rho}^2 = x^2 + y^2$ the radial coordinate.

4.3.2 *The setup*

After having specified the basic procedure, we can now go through the experimental setup. The whole simulation, sketched in Figure 4.1, can be split into the following steps:

- Incident Gaussian beam
- Propagation in free space for distance d_0
- Truncation by circular aperture with radius a
- Propagation in free space for distance d_1

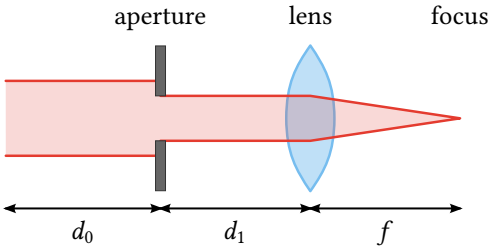

FIGURE 4.1: *Sketch of the setup for the simulation.* An incident Gaussian beam is clipped by a circular aperture of radius a and then focused by an ideal lens of focal length f after propagating in free space for a distance d_1.

- Focusing with a lens of focal length f and an additional vignetting with radius r_{in}
- Propagation in free space for distance d_2

The starting point is a monochromatic Gaussian beam of wavelength $\lambda = 1064\,\text{nm}$ and beam waist $w_0 = 9.95\,\text{mm}$ as described in the previous chapter. The filed is given by[13]

[13] *For simplicity we fix the initial overall phase to zero.*

$$U_0(\boldsymbol{\rho}) = \sqrt{\frac{2P_{\text{in}}}{\pi w_0^2}}\ \exp\left(-\rho^2/w_0^2\right), \tag{4.5}$$

such that is normalized with respect to the power of the incident light P_{in} via the condition $\int \mathrm{d}\boldsymbol{\rho}\ |U_0(\boldsymbol{\rho})|^2 = P_{\text{in}}$.

We omit the first propagation in free space, as it is negligible for beams with such a large waist. The effect of the circular aperture[14] with radius a is achieved by multiplying the field with its transmittance T_{ap}, i. e.

[14] *It is assumed to be infinitely thin.*

$$\begin{aligned} U_1(\boldsymbol{\rho}) &= U_0(\boldsymbol{\rho}) \times T_{\text{ap}}(\boldsymbol{\rho}; a) \quad \text{with} \\ T_{\text{ap}}(\boldsymbol{\rho}; a) &= \begin{cases} 1 & \text{if } \|\boldsymbol{\rho}\| \leqslant a \\ 0 & \text{else.} \end{cases} \end{aligned} \tag{4.6}$$

The next step is a propagation for a distance d_1 in free space:

$$\begin{aligned} U_2(\boldsymbol{\rho}') &= \mathcal{F}^{-1}\left\{\mathcal{F}\{U_1\}\, H_0(;d_1)\right\}(\boldsymbol{\rho}') \\ &= \int \mathrm{d}\boldsymbol{\nu}_\perp\, \mathrm{e}^{2\pi\mathrm{i}\,\boldsymbol{\rho}'\cdot\boldsymbol{\nu}_\perp}\, \exp\left(2\pi\mathrm{i}\, d_1 \sqrt{\lambda^{-2} - \nu_\perp^2}\right) \\ &\quad \times \int \mathrm{d}\boldsymbol{\rho}\, \mathrm{e}^{-2\pi\mathrm{i}\,\boldsymbol{\rho}\cdot\boldsymbol{\nu}_\perp}\, U_1(\boldsymbol{\rho}) \end{aligned} \tag{4.7}$$

The focusing properties of the objective are simulated by an aberration free hyperbolic biconvex lens of width Δ_0 and the same focal length $f = 20.3\,\text{mm}$ of the objective (see Table 3.2). Within the framework of Fourier optics, the lens simply imprints a phase pattern on the field which comes from the varying width $\Delta(\boldsymbol{\rho})$ of the lens in the radial plane [Sal+07]. Additionally, the vignetting effect of the opening aperture of the objective is

taken into account by multiplying the transmittance of a circular aperture T_{lens} with radius $r_{\text{in}} = 12.2\,\text{mm}$:

$$\begin{aligned} U_3(\boldsymbol{\rho}') &= U_2(\boldsymbol{\rho}') \times P_{\text{lens}}(\boldsymbol{\rho}') \\ &= U_2(\boldsymbol{\rho}')\, \mathrm{e}^{2\pi \mathrm{i}\, \lambda^{-1} \Delta_0}\, \mathrm{e}^{2\pi \mathrm{i}\, \lambda^{-1}(n-1)\Delta(\boldsymbol{\rho}')}\, T_{\text{lens}}(\boldsymbol{\rho}'; r_{\text{in}}), \end{aligned} \tag{4.8}$$

where n denotes the index of refraction of the lens. The thickness $\Delta(\boldsymbol{\rho})$ of an aberration free hyperbolic lens is given by [Pru+08]

$$\begin{aligned} \Delta(\boldsymbol{\rho}) = &\left[\Delta_0 - \frac{\rho^2}{R_1 \left(1 + \sqrt{1 + \rho^2 / R_1^2}\right)} + \frac{\rho^2}{R_2 \left(1 + \sqrt{1 + \rho^2 / R_2^2}\right)} \right] \\ &\times \begin{cases} 1 & \text{if } \|\boldsymbol{\rho}\| \leqslant r_{\text{lens}} \\ 0 & \text{else.} \end{cases} \end{aligned} \tag{4.9}$$

where $R_1 = -R_2 := R = 2f\,(n-1)$ denote the radii of the lens surfaces, and r_{lens} the radius and n the index of refraction of the lens.

The last step is simply another propagation in free space of the field U_3 as explained before. And the intensity is then finally $I(\rho) = U_{\text{final}}^2(\rho)$[15].

It is important to emphasize again, that no paraxial approximation has been used. None of the previous expressions includes any mathematical approximations except for the simplification and idealization of the optical components[16].

All these expressions cannot be solved analytically due to the numerous Fourier transformations, but the results can be calculated numerically using *discrete Fourier transform* (DFT) algorithms [Coo+65]. The numerical implementation has been done using the *Python* programming language[17]. In the following, the results of these calculations will be discussed.

[15] *As the whole system is radially symmetric, the intensity only depends on $\rho = \|\boldsymbol{\rho}\|$. Hence $I(\boldsymbol{\rho}) \equiv I(\rho)$.*

[16] *Additionally, we neglected the polarization of the light, by assuming a complex scalar field instead of an electro-magnetic vector field.*

[17] *The mainly used Python modules are `numpy` and `scipy`.*

4.3.3 *Results*

For the calculation, the complex-valued light field is discretized by a two-dimensional finite coordinate grid. In other words, the coordinates $\boldsymbol{\rho}$ and $\boldsymbol{\nu}_\perp$ are only evaluated for values of defined two-dimensional arrays with step sizes $\delta\rho$ and $\delta\nu$, respectively, between the values. In order to achieve reasonable results and to minimize numerical artefacts due to the discretization, the parameters (limits and step size) of the coordinate grid in real space have to be chosen well. The important physical parameters, that can be varied, are the aperture radius a and the distance between aperture and lens d_1.

Due to the large incident beam waist of 9.95 mm, the limits have to be in the order of tens of millimetres. In the end however, they can be reduced depending on the aperture radius a, because the field drops fast to zero for coordinates $\rho > a$. In Section 3.3 we have seen that the waist at the focus is around $\sim 1\,\mu\text{m}$. Therefore, the step size has to be in the order of a few hundred nanometres. As a consequence, we need at least in the order of 10^4 elements in each dimension of the coordinate grid, which makes in total

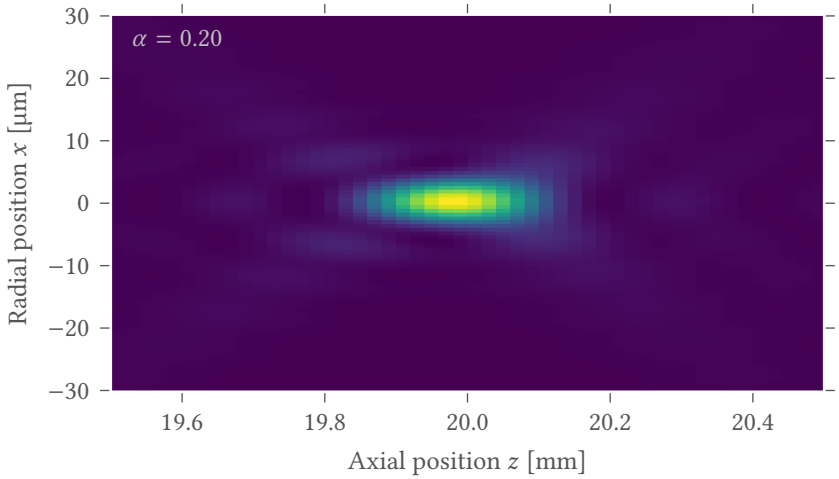

FIGURE 4.2: *Calculated profile in the zx-plane for the exact simulation.* A cut through the profile of the beam around the focus for a truncation ratio $\alpha = 0.20$ and a distance $d_1 = f$ between lens and aperture.

10^8 elements. Calculations with these large complex-valued arrays require a computer with very large internal memory and lead to very long computation times.

With our given resources, the aforementioned constraints have shown to imply a largest feasible aperture radius of $a = 2.0\,\text{mm}$, which corresponds to a truncation ratio $\alpha = a/w_0 = 0.20$. Therefore, we cannot derive quantitative results from these simulations for large truncation ratios. In the next section we will use a simplified approach to estimate quantitative results.

A profile cut in the zx plane around the focus, for $a = 2.0\,\text{mm}$ and $d_1 = f$, is shown in Figure 4.2. It can be seen, that fringes appear around the focus due to the diffraction of the aperture. In the radial plane, the profile resembles the well known *Airy disc*, which appears in the diffraction pattern at the focus of a circular aperture with a plane wave in terms of Fraunhofer diffraction. This is not surprising, as a Gaussian can be well approximated by a plane wave for small truncation ratios α. Interesting and non-trivial is however the axial profile and the emerging maxima around the central peak in the zx cut. Besides the side maxima on the radial and on the axial axes, there are also maxima on the „diagonal“ axes. In the three-dimensional profile, the latter appear as tori with increased intensity, i. e. the cuts in the radial plane are rings with high intensity and a minimum in the centre.

4.3.3.1 *Axial symmetry of the profile*

An important result of these simulations are the observations of the changing symmetry of the axial profile with the distance between lens and aperture d_1 and with the aperture radius a.

A symmetric axial profile is obtained, if the aperture is in the focal plane in front of the lens. When it is further apart or nearer to the lens, the profile

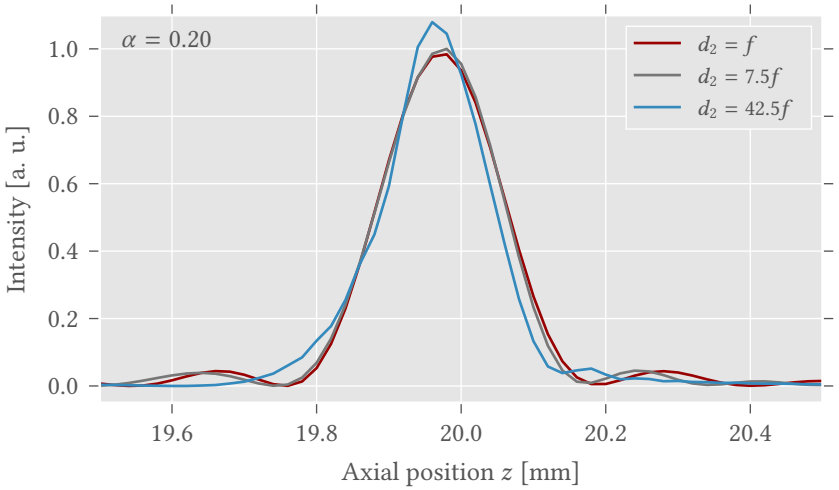

FIGURE 4.3: *Comparison of axial profiles around the focus for different distances between lens and aperture.* For a distance between lens and aperture $d_1 = f$ (red), the profile is symmetric around the focal plane. For larger distances $d_1 > f$ the profile becomes more and more asymmetric (grey, blue). The calculations are done for a truncation ratio $\alpha = 0.20$.

becomes asymmetric. The extent of the asymmetry depends strongly on the truncation ratio of the aperture.

To illustrate this effect, Figure 4.3 shows the axial profile at the focus for three different configurations of d_1. The simulation was done for a truncation ratio $\alpha = 0.20$. For $d_1 = f$, the profile is symmetric around the focal plane, but for distances $d_1 > f$ it gets stretched towards the lens.

The conclusion of these observations is, that ideally, the aperture should be placed in the focal plane. As this is not possible due to the size of the objective (it has a length of ~120 mm, but the focal length is ~20 mm), the distance between these two components should be as small as possible.

4.4 APPROXIMATE MODEL OF THE FOCUSSED TRUNCATED GAUSSIAN BEAM

We cannot do the exact calculations to obtain the profile of the microtrap for a sufficiently wide range of the truncation ratio (i. e. for large truncation ratios). The reason are numerical limitations discussed in the previous section.

Fortunately, for a limited special case and using the paraxial approximation, in [Hor+03] it has been shown, that an approximate analytic expression of the three-dimensional profile of a focused truncated Gaussian beam exist. Within this model, the axial intensity distributions is given by the expression

$$\begin{aligned} I_{\parallel}(z) &\equiv I(\rho = 0, z) \\ &= I_0 \left[1 - \frac{u_a/2}{\pi N_a}\right]^2 \frac{\alpha^4}{\alpha^4 + (u_a/2)^2} \frac{\cosh \alpha^2 - \cos(u_a/2)}{\cosh \alpha^2 - 1}, \end{aligned} \tag{4.10}$$

with

$$u_a\big|_{\rho=0} = 2\pi N_a \frac{(z-f)/f}{1+(z-f)/f}, \tag{4.11}$$

$$I_0 = \left[\frac{\pi a^2 A}{\lambda f^2}\frac{1-\mathrm{e}^{-\alpha^2}}{\alpha^2}\right]^2, \tag{4.12}$$

$$N_a = \frac{a^2}{\lambda f}. \tag{4.13}$$

And the radial intensity distribution is given as

$$I_\perp(\rho) \equiv I(\rho, z=f) = \left[2\mathrm{e}^{-\alpha^2}\frac{\pi A}{\lambda}\frac{a^2}{f^2}\sum_{n=1}^{\infty}\frac{\mathrm{J}_n(v_a)}{v_a^n}\left(2\alpha^2\right)^{n-1}\right]^2, \tag{4.14}$$

with

$$v_a\big|_{z=f} = 2\pi N_a \left.\frac{\rho/a}{1+(z-f)/f}\right|_{z=f} = 2\pi N_a \frac{\rho}{a}, \tag{4.15}$$

where J_n denote the Bessel functions. The amplitude A has to be chosen such that $\int \mathrm{d}\rho\, I_\perp(\rho) \stackrel{!}{=} P_{\mathrm{in}}$ with the power of the incident beam P_{in}.

These expressions are only valid for the special case, where the aperture is directly in the lens plane, i. e. $d_1 = 0$. As the paraxial approximation is used for the derivation, it is *a priori* not expected, that the formulae describe our system with high numerical aperture for large truncation ratios very well—especially as in reality we will have $d_1 \gg 0$. Nevertheless, the results will give an estimate of the emerging features due to diffraction, of the trap frequencies, and of the aspect ratios of the trap for different aperture radii.

The profiles of this simplified approach are qualitatively very similar to those of the exact calculation in the previous section. And they exhibit the discussed asymmetry due to $d_1 \neq f$, as expected. In Figure 4.4 the axial and radial profiles are compared for the exact calculation with the same parameters. The theory agrees astonishingly well with the exact calculation. The only strong deviation is at the minima, where the numerical calculation does not drop to zero as the theory does. But most probably, this deviation is just a numerical artefact.

4.4.1 *Aspect ratios*

To get the aspect ratio depending on the aperture radius, we calculated the axial and radial profiles for a set of radii a and fitted them quadratically around the maximum. The fits were done with the function

$$f(x) = -k\,(x-x_0)^2 + c, \tag{4.16}$$

such that $\omega_\perp^2 \propto k_\perp$ and $\omega_\parallel^2 \propto k_\parallel$ holds for the trapping frequencies. Hence, the aspect ratio is given by

$$\eta = \omega_\perp/\omega_\parallel = \sqrt{k_\perp/k_\parallel}. \tag{4.17}$$

The obtained aspect ratios are plotted in Figure 4.5.

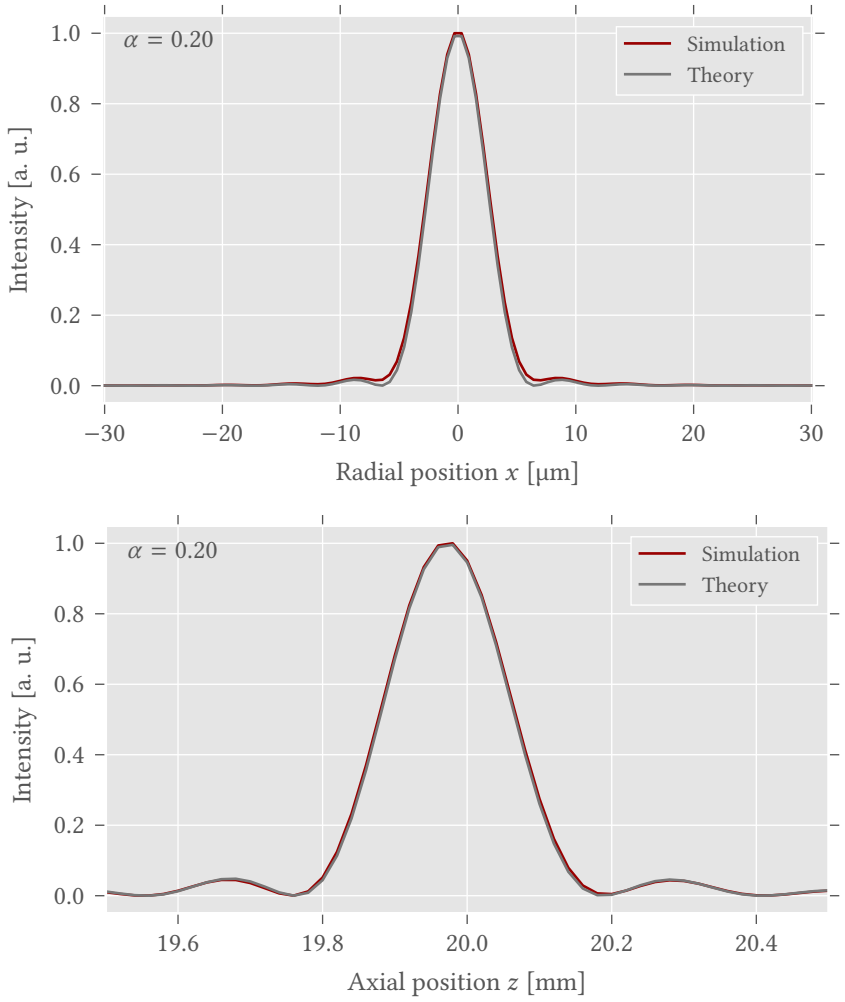

FIGURE 4.4: *Comparison of the radial and axial profiles between the exact calculation and the simplified theory.* In the upper diagram a cut through the profile in radial direction is shown and in the lower diagram a cut in axial direction. The calculation has been done for a truncation ratio of $\alpha = 0.20$

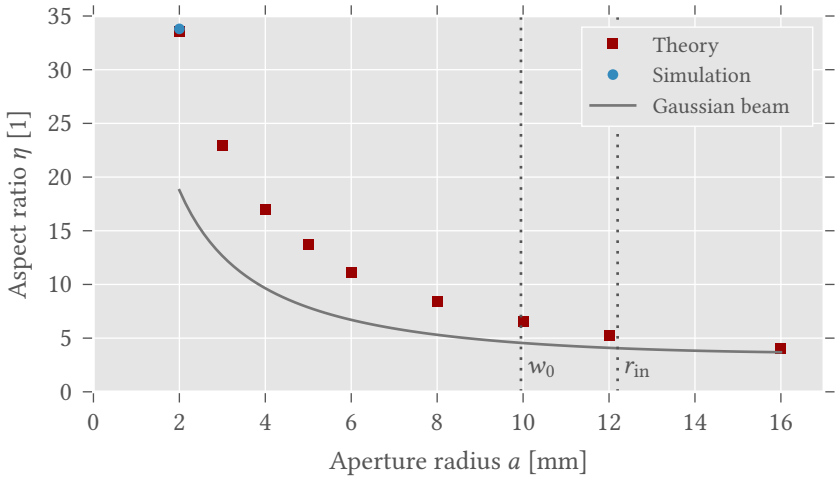

FIGURE 4.5: *Aspect ratios of the focussed truncated beam as a function of the aperture radius for the approximate theory.* Using the approximate theoretical model from [Hor+03], the aspect ratios of the trapping potential of the focussed truncated Gaussian beam have been calculated (red). For comparison, a data point of the exact simulation and the initial naive approach (4.1) of using an empirical formula and assuming a Gaussian beam, even after truncation, are plotted as blue circle and solid grey line, respectively. The former matches the approximate model quite well, whereas the latter can only describe the qualitative behaviour.

4.4.2 *Expected trap frequencies*

Besides the aspect ratio, the trap frequencies play an important role for the physics of the system. They can be calculated within this framework using the quadratic fits of the profiles mentioned in the last section and the formulae in Section 3.3.4[18]:

$$U_{\text{dip, ho}}(\rho, z) = \frac{1}{2} m_{\text{Li}} \left(\omega_\perp^2 \rho^2 + \omega_\parallel^2 z^2\right) \stackrel{!}{=} C \left(k_\perp \rho^2 + k_\parallel z^2\right) \quad \text{with} \tag{4.18}$$
$$C = \frac{3\pi c^2}{2\omega_0^2} \left(\frac{\Gamma}{\omega_0 - \omega} + \frac{\Gamma}{\omega_0 + \omega}\right),$$

such that

$$\omega_{\perp,\parallel}^2 = \frac{2C}{m_{\text{Li}}} k_{\perp,\parallel}. \tag{4.19}$$

When doing the calculations, one has to take the power loss due to the truncation into account, because the actual light power at the focus defines the trap depth. The output power of a Gaussian beam with initial power P_{in}, after truncation with a circular aperture, can be calculated analytically, and is given by

$$P_{\text{out}}(a) = P_{\text{in}} \left[1 - \exp\left(-2\frac{a^2}{w_0^2}\right)\right]. \tag{4.20}$$

The dependence of P_{out} on a is plotted in Figure 4.6 (top). It can be clearly seen that the power drops drastically for truncation ratios $\alpha < 1$ (i. e. $a < w_0$).

[18] *For simplicity we define our coordinate system such that the focus (i. e. the maximum) is at $\rho = 0 = z$.*

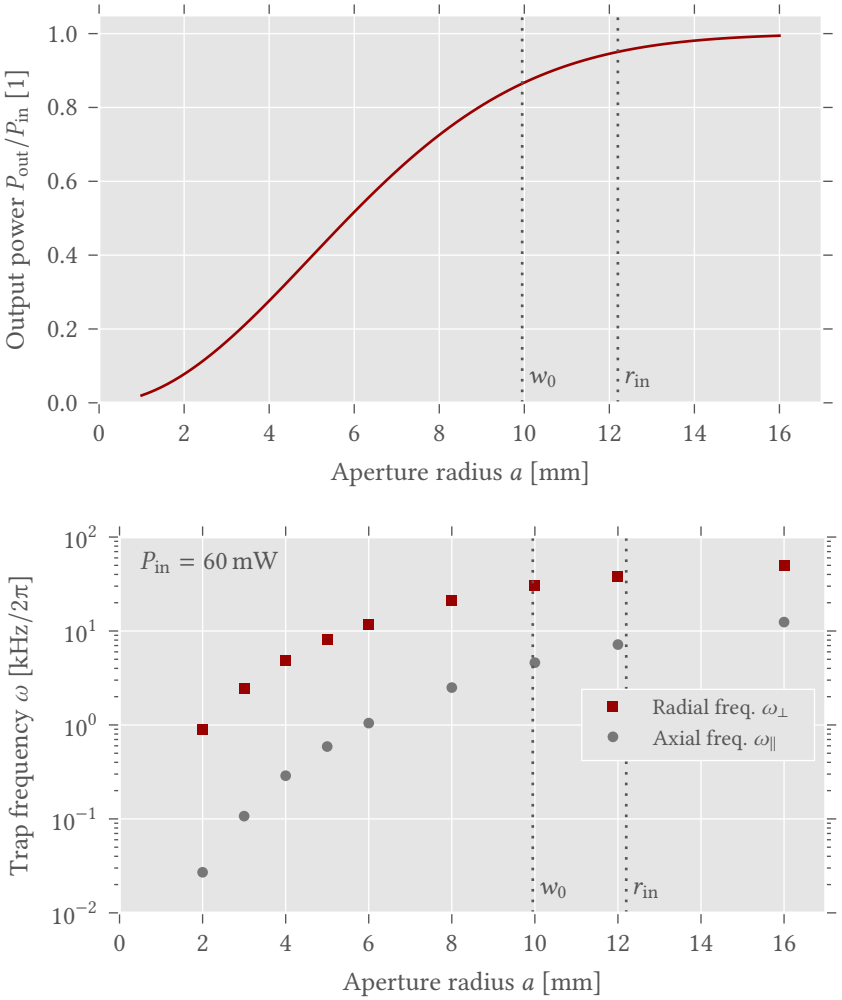

FIGURE 4.6: *Power and trap frequencies of the microtrap potential after truncation with a circular aperture as a function of the aperture radius.* Top: The power of a Gaussian beam after truncation with a circular aperture as a function of the aperture radius. Bottom: Radial and axial trap frequencies as a function of the aperture truncation radius for an input power of $P_{in} \approx 60\,\mathrm{mW}$.

With this in mind, trap frequencies can be calculated for a set of aperture radii and a given power of the incident laser light. The maximum power, we can achieve for our light, is $P_{in} \approx 60\,\mathrm{mW}$, which yields the trap frequencies shown in Figure 4.6 (bottom).

5

MEASUREMENT AND CHARACTERIZATION OF THE BEAM PROFILE

In the last chapter, we have discussed our method to change the aspect ratio of the microtrap by truncating the incident Gaussian beam. To get a feeling, how the shape of the trap and its physical properties change with the truncation, we have done and presented calculations.

In this chapter, we will present the characterization of the profile based on experimental measurements. The aim of these measurements is to get the real dependence of the aspect ratio of the microtrap on the truncation radius and to quantitatively measure the shape of the microtrap potential. Especially, it is interesting to know, how well the presented theory can describe the microtrap. Knowing the exact shape of the trapping potential is important, as emerging asymmetries leading to anharmonicites can alter the physical properties of the system, like the energy spacing of the states in the trap and the wave functions

Before presenting the final results, we will outline how the measurements have been carried out.

5.1 A SETUP FOR BEAM PROFILE ANALYSIS

The detailed optical setup to create the microtrap potential has already been presented in Section 3.3.2. We did the measurements on a test setup, that is almost identical to the experimental setup. Nevertheless, the same objective as in the experiment was used. Furthermore, we checked the expanded laser beam for wave front errors using a *shearing plate interferometer* [Swe90].

To measure the profile, we moved a camera along the axial axis (z-axis) and took images of the radial profile for different positions z around the focus. The optical setup of the measurement is sketched in Figure 5.1.

5.1.1 *The beam truncation*

For the beam truncation, we use an aperture with a variable diameter. A servo motor controls the opening of the aperture, it can open or close the aperture in roughly 0.5 s. This makes it possible to change the aspect ratio of the microtrap during the experimental sequence with an Arduino micro controller. For example, one could prepare the few particle system in the initial trap, with which a high preparation fidelity is ensured, and then change the trap adiabatically with the motor. The main mechanics of the automated aperture consist of two gears, one attached to the servo motor and the second attached to the aperture.

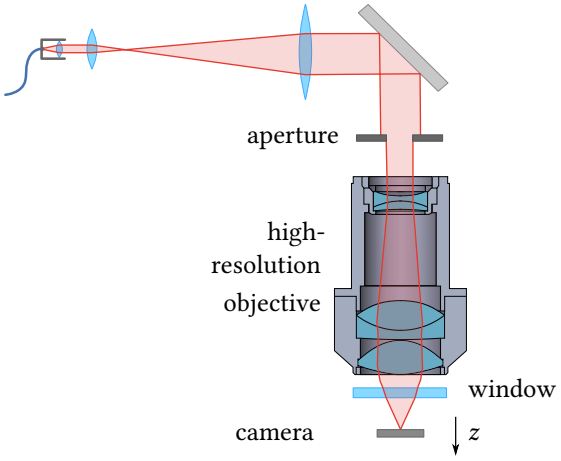

FIGURE 5.1: *Sketch of the simplified setup for the measurement of the microtrap potential with a camera.* An incident Gaussian beam is expanded to a waist of $w_0 = 9.95\,\text{mm}$ using a telescope, truncated by a circular aperture of radius a, and finally focused by our high-resolution objective with an effective focal length $f = 20.3\,\text{mm}$. The profile of the microtrap potential is measured by moving a camera along the propagation axis (z-axis), as illustrated, and taking images of the radial profile for different z positions. Based on a sketch from [Ber13, p. 33].

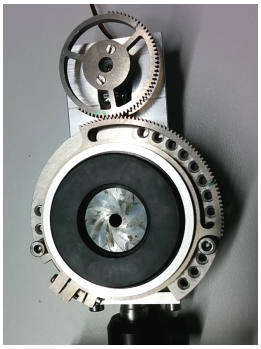

FIGURE 5.2: Image of the fully assembled aperture with mount and servo motor.

To increase stability and reproducibility with respect to the aperture radius, a special mount for aperture and servo motor had to be designed and manufactured. The important part is a ring with holes for common M4 screws, which function as stable start and end stops for the gears. The fully assembled aperture can be seen in Figure 5.2. The details and the sketches of the three designed parts are listed in Section B.1.

There are two types of holes in the ring: On the left side three holes mark the starting point for the open aperture, and on the right side thirteen holes ensure endpoints with different aperture radii. In order to make a fine adjustment of the radii possible, the distances between the starting point holes is 1.25 times as large as the distances between the endpoint holes. A table with the possible aperture radii corresponding to the different holes is found in Section B.2.

The automation of the opening and closing the aperture using an Arduino has not been implemented within the scope of this thesis. As of now, it is not

FIGURE 5.3: Image of the Raspberry Pi in its case with the connected camera module.

TABLE 5.1: *Specifications of the Raspberry Pi camera CMOS chips.* The OmniVision 5647 chip corresponds to version one of the camera and the Sony IMX 219 PQ chip corresponds to version two of the module. Taken from [Omn10; Son14].

	OmniVison 5647	Sony IMX 219 PQ
Pixel size	1.4 µm	1.12 µm
Resolution	5 MP	8 MP
Columns	2592	3280
Rows	1944	2464
Max. data depth	10 bit	10 bit

clear how the dynamic changing of the aspect ratio during the experimental sequence will affect the preparation scheme.

5.1.2 *The Raspberry Pi camera*

For the characterization of the beam profile, one has to take images of the radial profile at different axial positions. Without truncation, the beam waist after focussing is slightly larger than a micrometre (see Section 3.3 and Appendix C). In order to be able to resolve the diffraction patterns, that emerge due to truncation, a camera with sufficiently small pixel size is required. The smallest pixel size of camera chips so far is 1.0 µm [Sam15] but no usable camera with this chip is currently available.

Fortunately, there is an external camera module for the *Raspberry Pi* minicomputer. It offers a camera with a CMOS chip with small pixel size, as an affordable solution with a high degree of control. The second half of April 2016 a version two of the camera module was released, offering a chip with a pixel size of 1.12 µm instead of the previous 1.4 µm [Upt16]. The specifications of the CMOS chips of the two camera modules are listed in Table 5.1. Since the new chip with the small pixel size is better for our purpose, we will always refer to version two of the camera in the following. Both versions of the module are available in two variants: a default version and one without an IR filter („NoIR camera“). To ensure usability at $\lambda = 1064$ nm, we use only the NoIR variant for our measurements. The Raspberry Pi with connected camera is shown in Figure 5.3.

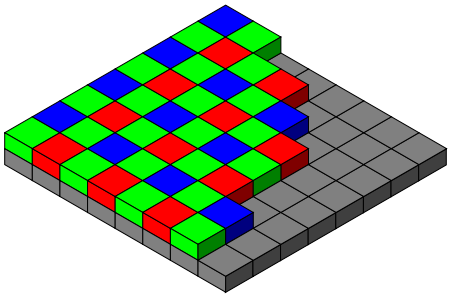

FIGURE 5.4: *Sketch of the BGGR Bayer filter pattern for a camera chip.* Starting from the top left corner, every odd row has alternating BG columns and every even row has GR columns. Taken from [Jona]

5.1.2.1 *Numerical aperture of the camera chip*

Originally, a lens was mounted on the chip, to enable sharp imaging of far objects. As we want to image directly onto the chip, this lens is removed, leaving a mount surrounding the chip, which limits its numerical aperture.

The maximal numerical aperture of the chip at the central region is estimated as

$$\mathrm{NA}_{\mathrm{camera}} = \sin\left(\arctan\left(\frac{5.5\,\mathrm{mm}}{2\times 3.1\,\mathrm{mm}}\right)\right) \approx 0.66, \tag{5.1}$$

which is enough for our objective with a maximum numerical aperture of roughly 0.6.

5.1.2.2 *RGB pattern of the chip*

The CMOS chip of the Raspberry Pi camera is an RGB chip, i. e. the pixels are covered with a filter that creates four types of pixels: one sensitive to red, one to blue, and two differently sensitive to green light. The pixels are arranged in a *BGGR Bayer pattern* as shown in Figure 5.4. In other words, there are two types of rows: odd rows are *BG* with alternating blue and green pixels, starting with blue, and even rows are *GR* with alternating green and red pixels, starting with the former. Importantly, the green pixels in BG are different than those in GR. The reference point is the top left corner of the image and the chip, respectively[19].

[19] *It is important to note that, while images start from the top left corner, 2D plots start from the bottom left corner as this marks the zero-crossing of the ordinate.*

When imaging the microtrap with the camera, we only need the light intensity at each pixel, and no RGB colour information. The unprocessed measured 10 bit data from the chip is obtained, by taking the raw Bayer images.

Since the colour filters on the chip have different sensitivity to infrared light, the four pixel types have to be calibrated with respect to one fixed colour type. As the blue pixels yield the highest intensities, we chose them as reference. In order to calibrate the images, we took a reference image of a Gaussian beam in the centre of the chip and split it into four images, that contain only the data of every pixel type separately. Then each image could be fitted independently with a two-dimensional Gaussian. The quotient of

TABLE 5.2: *RGB calibration ratios of the Raspberry Pi camera.* The calibration of a raw RGB image is done by multiplying the different pixel type data points with the corresponding ratios, whereas the data of the blue pixels stays fixed. Green 1 denotes the green pixel in the BG rows and Green 2 the green pixel in the GR rows.

Pixel type	Calibration ratio $r_{\text{color/B}}$ [1]
Green 1	0.97 ± 0.15
Red	1.09 ± 0.16
Green 2	1.38 ± 0.19

the amplitudes of the obtained Gaussians, with respect to the amplitude of the blue pixel data, gives the calibration, $r_{\text{color/B}} = I_{0,\,\text{color}}/I_{0,\,\text{B}}$. The ratios used for the measurements presented in Section 5.2 are listed in Table 5.2.

5.1.2.3 *Controlling the camera*

The Raspberry Pi is a minimal computer running a Linux system[20]. The connected camera can be accessed and addressed using the Python `picamera` module [Jonb]. A minimal code example, to capture and save an image including raw Bayer data, is shown in Listing D.1. The image is saved in the common JPEG format, with the raw image appended as meta data at the end of the file. Before the raw data can be used for evaluation, the raw bytes have to be extracted from the file and converted to usable data arrays. A recommended Python code is shown in Listing D.2.

[20] *The used Linux distribution is called* Raspbian *and is based on* Debian.

To provide a convenient and self-explanatory way to capture images and save them on the group server, we have developed a very simple and intuitive web front end from scratch. It makes it possible to take single images and whole image sequences from any computer, that is connected to the same network as the Raspberry Pi, just by using the web browser, and without installing any software.

The front end for the single captures is shown in Figure 5.5 (top). When pressing the button „Take image“, an image is fetched from the camera, stored in the buffer, and shown in the area below. By scrolling the mouse wheel over the image, it can be zoomed in and out. Only when pressing the button „Copy“, the current image is copied from the buffer onto the server. All images are saved on the group server under the path

```
//jochim-server/Allgemeines/Michael
Dehabe/camera/yyyy-mm-dd/###_name/,
```

where `yyyy-mm-dd` denotes the current date, `###` the automatically incremented number of the image on that day, and `name` is an explanatory name entered into a popped up input box by the user.

Similarly, a front end exists, to take a whole sequence of images, store it in the buffer, and finally copy it as a whole onto the server.

Due to the simple and basic implementation of the front and the back end, taking an image requires a few seconds. When searching for the focus,

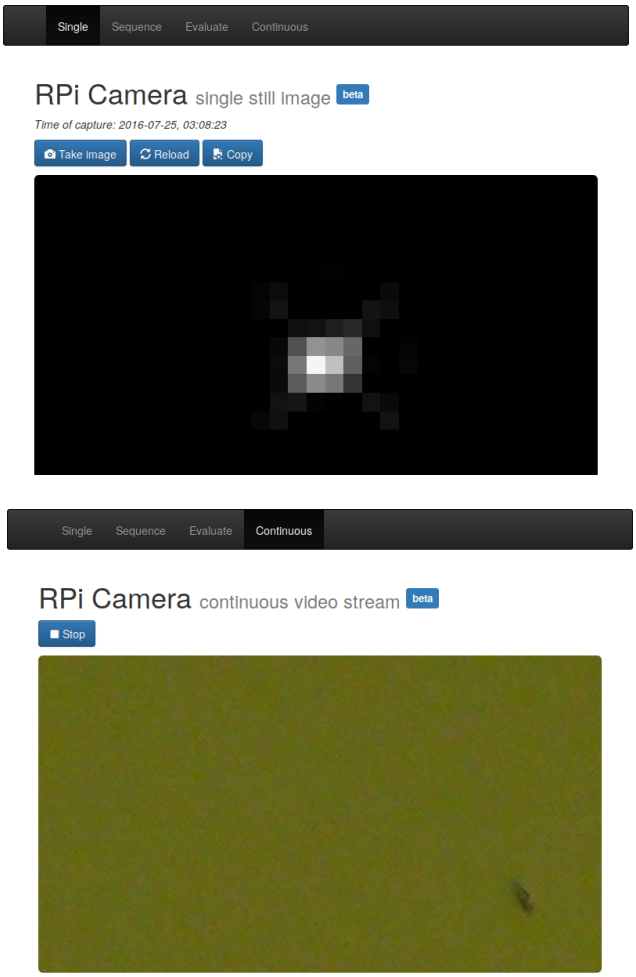

FIGURE 5.5: *Screenshots of the web front ends for using the camera.* Shown are the developed front ends for taking high-resolution raw images (top) and for showing a continuous video stream of the camera (bottom).

this can be a serious drawback. Therefore, a very simple continuous video stream of the camera has been implemented and integrated into the front end (Figure 5.5, bottom). When using it, one has to consider that it can only transfer images in 1080p, i. e. in a resolution of 1920×1080 pixels, which is much less than the full resolution of the raw images.

5.1.2.4 *Scanning the three-dimensional profile*

Having prepared a camera with a small pixel size, the scan of the three-dimensional profile of the focussed beam is fairly simple: The camera is mounted on a translation stage, such that every image taken represents the profile in the radial plane (xy-plane), and moved along the axial axis (z-axis), to obtain the three-dimensional profile around the focus. As translation stage, we used a *New Focus Triple-Divide 9064*, together with a *Newport TRA25CC Actuator*. The latter can be controlled with an accuracy of 0.2 µm, using a computer.

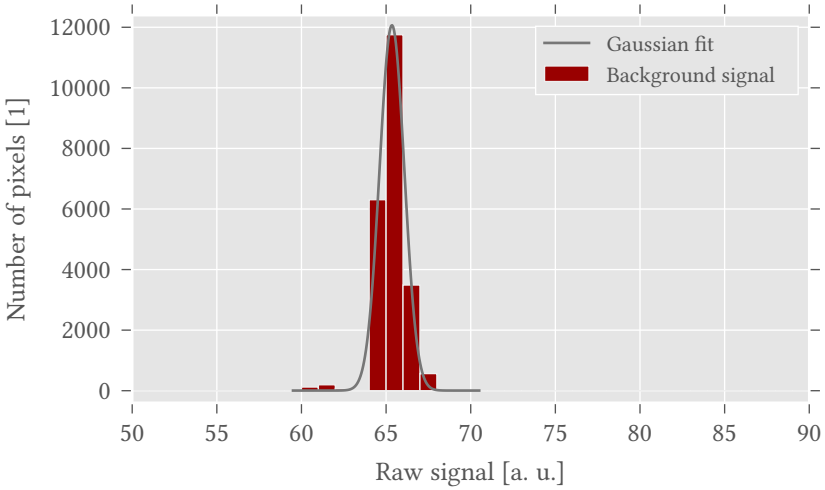

FIGURE 5.6: *Histogram of a background image of the Raspberry Pi camera.* To obtain the histogram, the number of pixels for every value of the unprocessed raw 10 bit signal of the camera chip is counted and plotted. To characterize the readout noise, a Gaussian is fitted to the data which gives an offset of 64.8 with a standard deviation of 0.7.

5.1.3 *Data preparation*

In the preceding subsection, we presented the way of taking raw images. Now, the tools to process and to evaluate them, in order to extract the important information, are necessary. For this purpose, the following steps and methods have to be considered:

- Subtraction of a background image
- RGB calibration
- Calculation of the centre of the profile in the xy-plane
- Increase of the signal-to-noise ratio by merging two datasets with different intensities

When the signal of the pixels on the chip is read and converted to digital data, a constant offset is added to avoid negative values. To take care of this artificial background, we take an image with the light source blocked, and subtract this *background image* from every measured image[21]. The histogram of such an image with the raw 10-bit data is shown in Figure 5.6. A Gaussian fit to the data yields an offset of 64.8 with a standard deviation of 0.7. The latter is a measure of the readout noise of our camera.

The next step is the RGB calibration mentioned and explained in Section 5.1.2.2. The calibration factors are simply multiplied with the data.

The uncertainties of the data have two main contributions: Shot noise and readout noise, whereas the former dominates at high intensities. Shot noise has a Poissonian distribution due to its origin in the discrete nature of the

[21] *Additionally other sources of noise are taken care of by doing this, e. g. fixed-pattern noise.*

photons. Therefore its contribution for every pixel i is given as $\Delta I_{\mathrm{sn},i} = \sqrt{I_i}$, where I_i denotes the calibrated signal of pixel i with subtracted background.

5.1.3.1 *Calculation of the centre of a radial profile*

When measuring a scan along the z axis through the focus, the radial profile moves slightly on the camera. This effect is taken care of, by calculating a measure of the centre of the profile and centring every image with respect to this point.

For light spots with a Gaussian distribution or with a intensity maximum at the centre, this calculation is straightforward. However, the radial profile takes non-trivial distributions at regions further away from the focus (see Section 4.4), such that a more general algorithm is necessary.

The most simple solution is a *centre-of-mass* algorithm: The weighted mean value of the coordinate grid is calculated, with the intensities as the weights, at each data point. It turned out that the performance with low maximum intensity is improved, when additionally a threshold is introduced. E. g. half the maximum intensity of the evaluated image is used as a threshold, and all data points below that are set to zero. Then, only the remaining non-zero data contributes to the weighted average.

This simple algorithm turned out to be very robust and precise. A further improvement with sub-pixel precision is achieved, by up-sampling the data as an additional step. I. e. each pixel is split into sub-pixels to increase the resolution of the data artificially.

The laser beam has shown to exhibit an astigmatism at the focus (see Appendix C), which results in the radial profiles not being radially symmetric, as it would be ideally the case. Therefore, the algorithm cannot produce very accurate results along the whole z axis, especially for spots without an intense maximum at the centre. But undoubtedly there is no simple alternative, without implementing more elaborate pattern recognition algorithms.

5.1.3.2 *Improvement of the signal-to-noise ratio of a profile scan*

When doing a scan, the power of the laser light has been chosen, such that most of the 10 bit range of the chip is used at the most bright spot, but still being well below the maximum value of 1024, to avoid saturation. The profile of the focussed beam along the z axis consists of an intense maximum at the focus and small features, such as fringes, at the outer regions—depending on the beam truncation.

As a consequence, the data points at the outer regions have very low intensity, and hence a small signal-to-noise ratio. To improve the latter, for each scan an additional second dataset with approximately 10 dB more power has been taken, which is be saturated at the focus, but that yields much better data for the small features of the profile.

The two datasets are merged by normalizing the data: The whole data in the evaluated image section is summed up to obtain a measure of the total intensity, with which each pixel is then divided. Furthermore, the data is

multiplied by the total number of pixels to obtain values that are comparable, independently of the size of the chosen image section, and to avoid very small numbers. Additionally, the normalization cancels fluctuations in the power of the laser light.

5.1.4 *The effect of the finite pixel size*

To extract the important information from the prepared data, several fits have to be carried out. The most common routine is a fit with a Gaussian function in the radial plane, to get the waist of the focus. This is done under the assumption, that this model describes the profile of the light. To do this, a general two-dimensional Gaussian function is used:

$$\begin{aligned} f(x,y) = A\,\exp\big(&\alpha\,(x-x_0)^2 + \gamma\,(y-y_0)^2 \\ &- 2\beta\,(x-x_0)(y-y_0)\big) + c, \quad \text{with} \\ \alpha &= 2\,\frac{\cos^2\theta}{\sigma_x^2} + 2\,\frac{\sin^2\theta}{\sigma_y^2}, \\ \beta &= -\frac{\sin(2\theta)}{\sigma_x^2} + \frac{\sin(2\theta)}{\sigma_y^2}, \\ \gamma &= 2\,\frac{\sin^2\theta}{\sigma_x^2} + 2\frac{\cos^2\theta}{\sigma_y^2}, \end{aligned} \tag{5.2}$$

where σ_x, σ_y denote the two beam waists, (x_0, y_0) the position of the centre, A the amplitude, c a constant offset, and θ the angle between the main axes of the Gaussian and the data grid axes. The code of its implementation can be seen in Listing D.3.

We image the beam profile with the camera, which has a waist of comparably the same size of a pixel (without truncation). When imaging such small structures, one has to consider the comparably large size of the pixels and the technical design of each pixel. For simplicity, we assume that all photons impinging on a pixel are collected by the detector at the centre of the pixel[22]. Therefore, the spatial information of the light over the whole area of the pixel is reduced to just the position of the pixel. To take this into account, a modified function $\tilde{f}(x,y)$ is fitted to the measured data, instead of the ordinary Gaussian distribution (5.2). This function does the following: The two-dimensional coordinate grid (x,y), i. e. the input of the function with the same resolution of the data to fit, is firstly sampled up by a factor k (e. g. 15), and then the fitting function (5.2) is applied on this up-scaled array. The hereby obtained data has k-times the resolution of the actual data to be fitted. In the next step, it is down-sampled again by dividing it into bins of size k and then summing up all data points in every bin, yielding the incidental resolution of the data to fit. This procedure mimics the behaviour of the camera chip.

[22] *In reality not all of them can be collected, depending on the technical realisation of the detector, that is not known for the used CMOS chip.*

To compare the two models, a measured image of the radial beam profile (without truncation) near the focal plane has been fitted with both (see Figure 5.7). Apparently, both models produce almost identical fits to the data (in

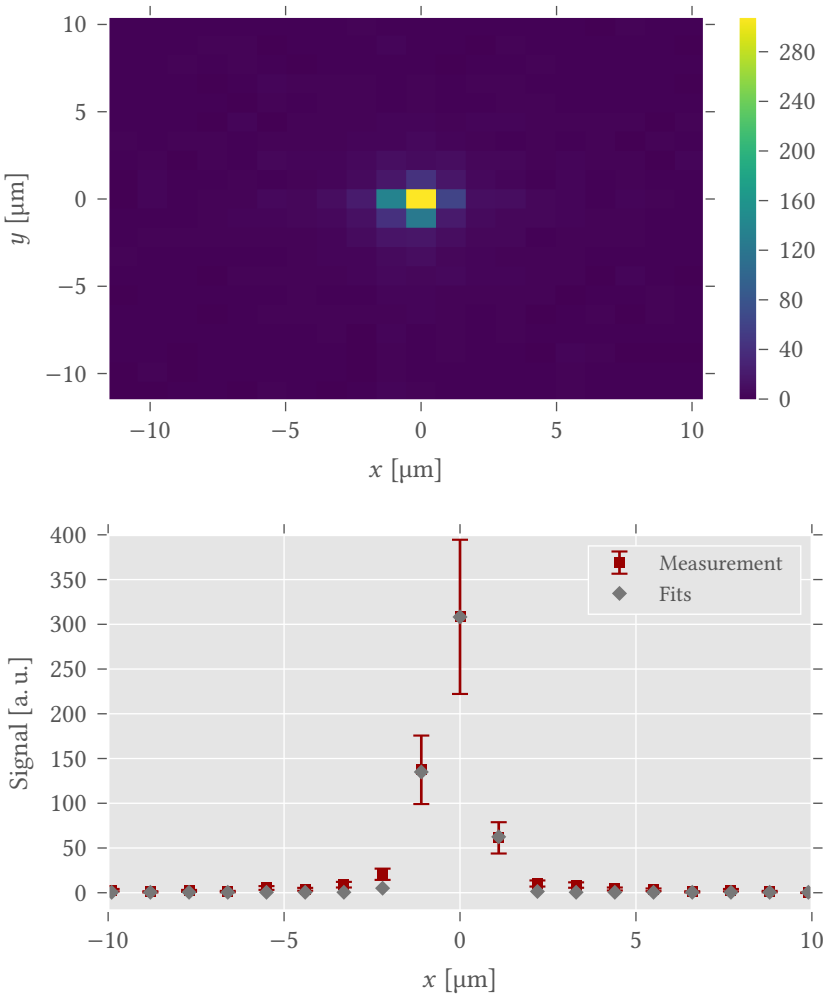

FIGURE 5.7: *Comparison of the advanced fitting procedure with an ordinary Gaussian function by fitting the radial beam profile near the focus.* Top: The image of the two-dimensional radial profile of the untruncated focussed beam near the focal plane, processed as explained in Section 5.1.3. Bottom: The image shows a cut through the x-axis of the experimentally measured radial profile (red rectangles). The data has been fitted with both models. Both lead to almost identical fits (hence both are represented by the grey diamonds, as they are not distinguishable). However, they yield different beam widths: $w_x = (1.41 \pm 0.01)\,\mu\text{m}, w_y = (1.30 \pm 0.01)\,\mu\text{m}$ the ordinary Gaussian and $w_x = (1.25 \pm 0.01)\,\mu\text{m}, w_y = (1.12 \pm 0.01)\,\mu\text{m}$ the advanced model. A measurement with a microscope objective and a CMOS camera, such that the finite pixel size plays almost no role, gave a width of ~1.2 µm (see Appendix C). Hence, the advanced model gives a width, that is nearer to the measured value, where the pixel effect is negligible.

Figure 5.7, bottom, they are both represented by the grey diamonds). However, the beam widths obtained from both models differ significantly: the ordinary Gaussian gives $w_x = (1.41 \pm 0.01)\,\mu\text{m}, w_y = (1.30 \pm 0.01)\,\mu\text{m}$ and the advanced fit yields $w_x = (1.25 \pm 0.01)\,\mu\text{m}, w_y = (1.12 \pm 0.01)\,\mu\text{m}$. The widths in the two radial axes differ, due to an astigmatism, as explained in Appendix C. The beam waist has also bean measured using a microscope objective with a magnification $M = 69 \pm 6$, such that the effect of the finite pixel size becomes negligible. This measurement gave a waist of $\sim 1.2\,\mu\text{m}$ (see Appendix C). The comparison with this value shows, that the advanced fit model yields a beam waist that is nearer to the more trustable value obtained using a microscope objective.

A code example with a general model[23] is given in Listing D.4.

[23] *I. e. a model that can be used for fitting functions other than the Gaussian as well.*

5.2 RESULTS AND COMPARISON WITH THE THEORY

In the last chapter, we discussed the method to modify the trap by truncating the incident Gaussian beam. As we want to study 1D physics, the microtrap needs to have a large aspect ratio η (see Chapter 2). However, we also want to know its actual shape, emerging from the diffraction due to the clipping. How strongly deviates the potential from a harmonic one? And how well can the theory describe the microtrap after clipping? To clear these questions, the intensity distribution around the focus has been measured for a set of aperture radii, with the methods and tools discussed in the preceding section. These results will be presented in the following.

The limiting cases of the aperture radius are 0.5 mm and 12.5 mm, for fully closed and fully opened aperture, respectively. The latter corresponds to the case without truncation, because the entrance aperture radius of the objective $r_{\text{in}} = 12.2\,\text{mm}$ is smaller. In total, the measurement has been carried out for the values 0.5, 1.2, 2.5, 4.0, 6.5, and 12.5 mm.

Cuts of the selected measured profiles in the zx plane are shown in Figure 5.8. Appendix A contains all measured profiles. Qualitatively, the features of the profiles for smaller truncation ratios $\alpha = a/w_0$ clearly resemble those of the simulation, as discussed in Section 4.3.3: Around the main maximum at the focus, side maxima emerge on the axial, on the radial, and on the *diagonal* axes in the zx-plane. The smaller the truncation ratio is, the more pronounced these become. An emerging asymmetry along the axial axis with decreasing aperture radius can also be clearly seen. This becomes even more obvious in logarithmic plots of the zx profiles, as can be seen in Figure 5.9. All profiles in logarithmic scales are shown in Appendix A.

By fitting both profiles—in axial and radial direction—we will now study the shapes quantitatively

5.2.1 *Aspect ratios*

As our aim is to increase aspect ratio of the trap in a controlled way by clipping the incident beam, we are interested in its dependence on the trunca-

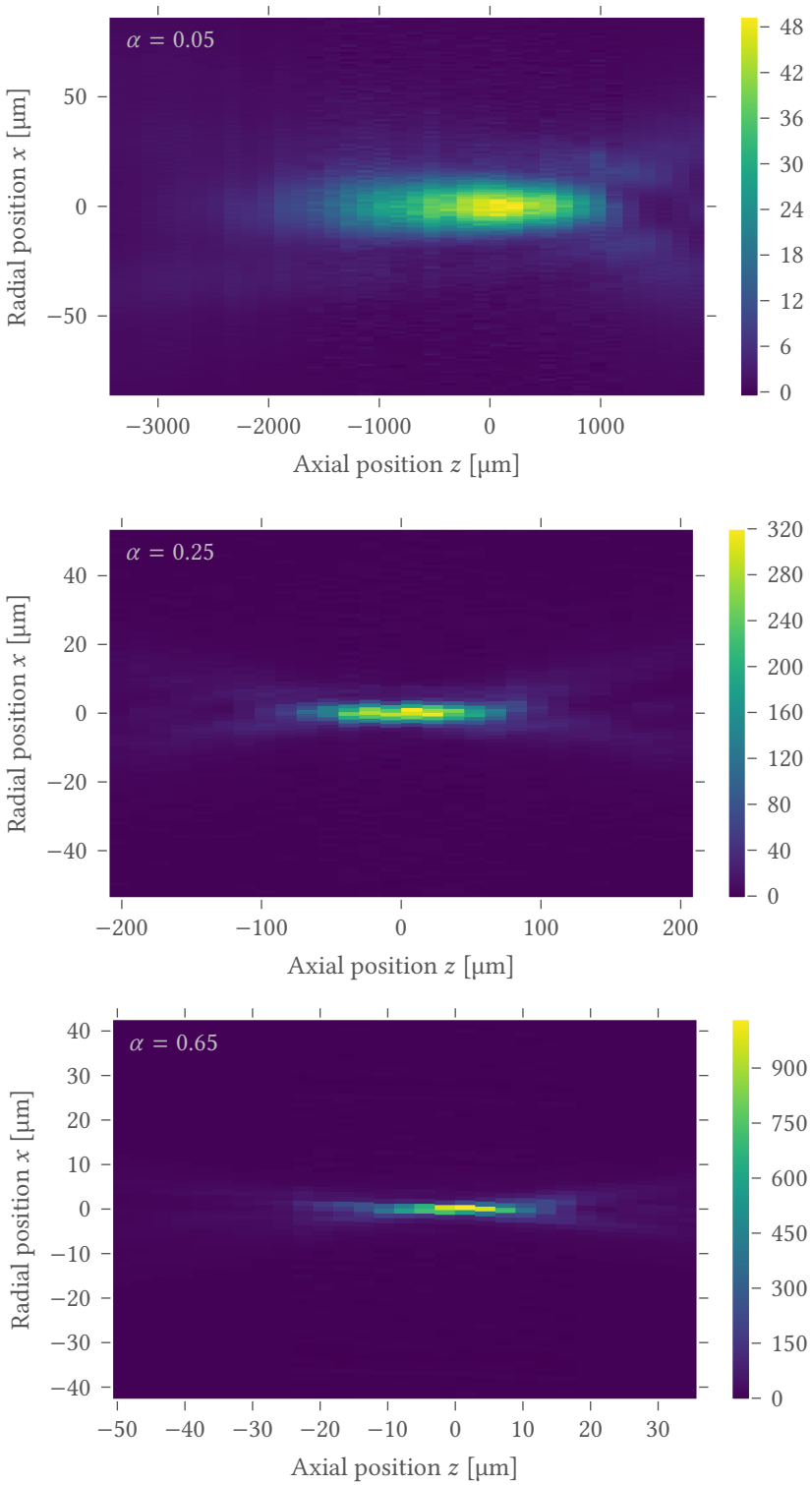

FIGURE 5.8: *Comparison of measured two-dimensional cuts of the beam profiles for* $a = 0.5, 2.5,$ *and* 6.5 mm *(from top to bottom).* The profiles show, how the size of the profile increases quickly with decreasing truncation ratio. Furthermore, the emergence of diffraction patterns and of an asymmetry along z is apparent. Please note the different z and x ranges. All measured profiles are shown in Appendix A.

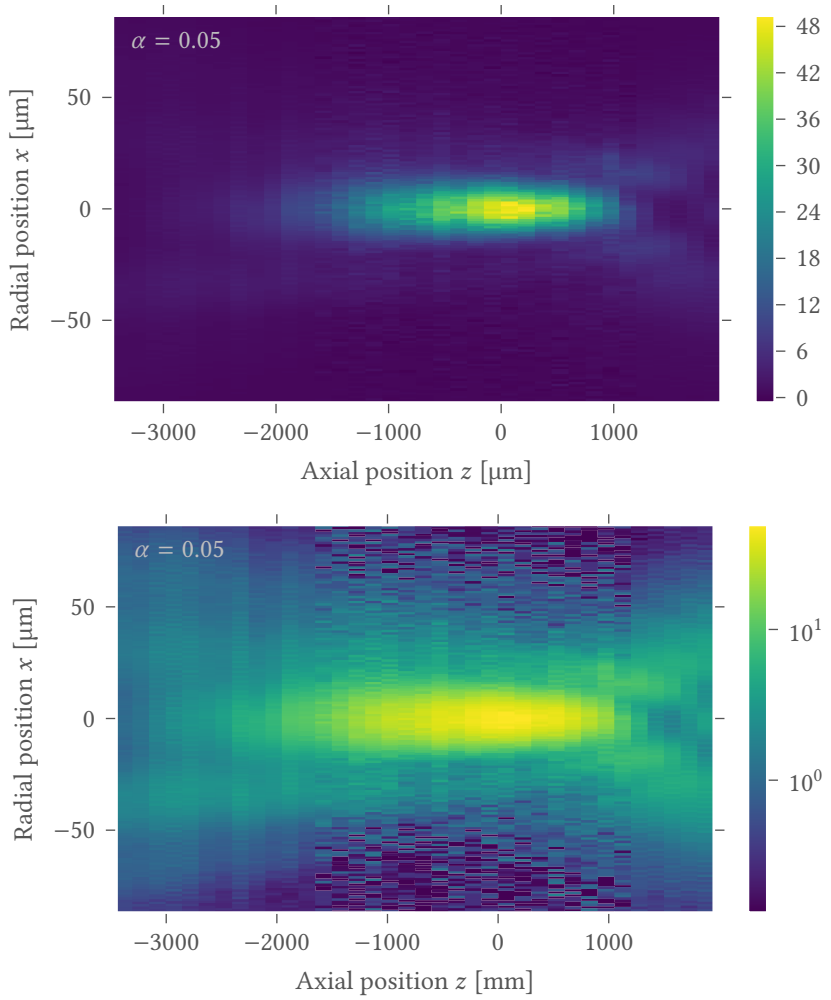

FIGURE 5.9: *Measured two-dimensional cut of the beam profile for* $a = 0.5\,\mathrm{mm}$ *(logarithmic).* The emergence of diffraction patterns and of an asymmetry along z is more obvious, if the zx profile is plotted logarithmically (bottom), in comparison with the linear scaling (top). Please note the different z and x ranges. All logarithmic profiles are shown in Appendix A.

TABLE 5.3: *Measured waists and aspect ratios of the beam profiles.* The waists w_x and w_y of the two radial axes are listed for each measurement with different aperture radius a along with the obtained aspect ratios η.

a [mm]	η [1]	w_x [µm]	w_y [µm]
0.5	113 ± 6	16.65 ± 0.03	15.01 ± 0.03
1.2	57 ± 4	8.059 ± 0.018	8.197 ± 0.018
2.5	28 ± 3	3.794 ± 0.010	3.670 ± 0.010
4.0	16.4 ± 1.2	2.414 ± 0.008	2.510 ± 0.008
6.5	9.6 ± 0.7	1.443 ± 0.005	1.714 ± 0.005
12.5	5.5 ± 0.3	1.253 ± 0.007	1.120 ± 0.007

tion. The aspect ratios are obtained by doing quadratic fits of the radial and axial profiles. However, to also measure the asymmetry quantitatively, i. e. the deviation from a harmonic shape, we fit with a polynomial up to fourth order. This corresponds to a Taylor expansion up to fourth order around the maximum[24]:

$$f(x) = k_2 (x - x_0)^2 + k_3 (x - x_0)^3 + k_4 (x - x_0)^4 + c, \tag{5.3}$$

[24] *At the maximum, the first derivative vanishes and hence the first order term is not needed.*

where x_0 denotes the position of the maximum (i. e. the focus), k_2, k_3, k_4 the coefficients of the respective orders, and c a constant offset. The aspect ratio is then given by $\eta^2 = k_{2,\perp}/k_{2,\parallel}$, similarly to Section 4.4.1.

To get the image for every scan, that is nearest to the focal plane, for the radial fit, the radial profiles on the images around the axial maximum were fitted with a Gaussian for every measurement. The image with the most circular Gaussian is then assumed to be nearest to the focal plane and is used for the radial polynomial fits. 5.10 shows the axial profiles of selected measurements together with the fitted quartic polynomials. The axial profiles of all measurements are shown in Appendix A. The obtained aspect ratios and the waists are listed in Table 5.3. The former are also plotted in Figure 5.11 as a function of the aperture radius.

Unfortunately, the results of the measurement with fully opened aperture, $a = 12.5$ mm, has to be handled with care: The brightest pixel of two images at the focus was slightly saturated. However, the resulting deviation is most likely within the uncertainty of these points.

5.2.2 *Measured anharmonicities*

As presented previously, the profiles have been fitted with a quartic polynomial, in order to get the correction terms to the harmonic potential. When treating the two particles in the trap theoretically, in Chapter 2, we assumed a harmonic potential. This resulted in evenly spaced energy levels, axially and radially. However, if the potential has higher order contributions, the energy spacing will decrease with higher excitations. Additionally, the wave functions will change as well, and with these also the quasi-particle residue.

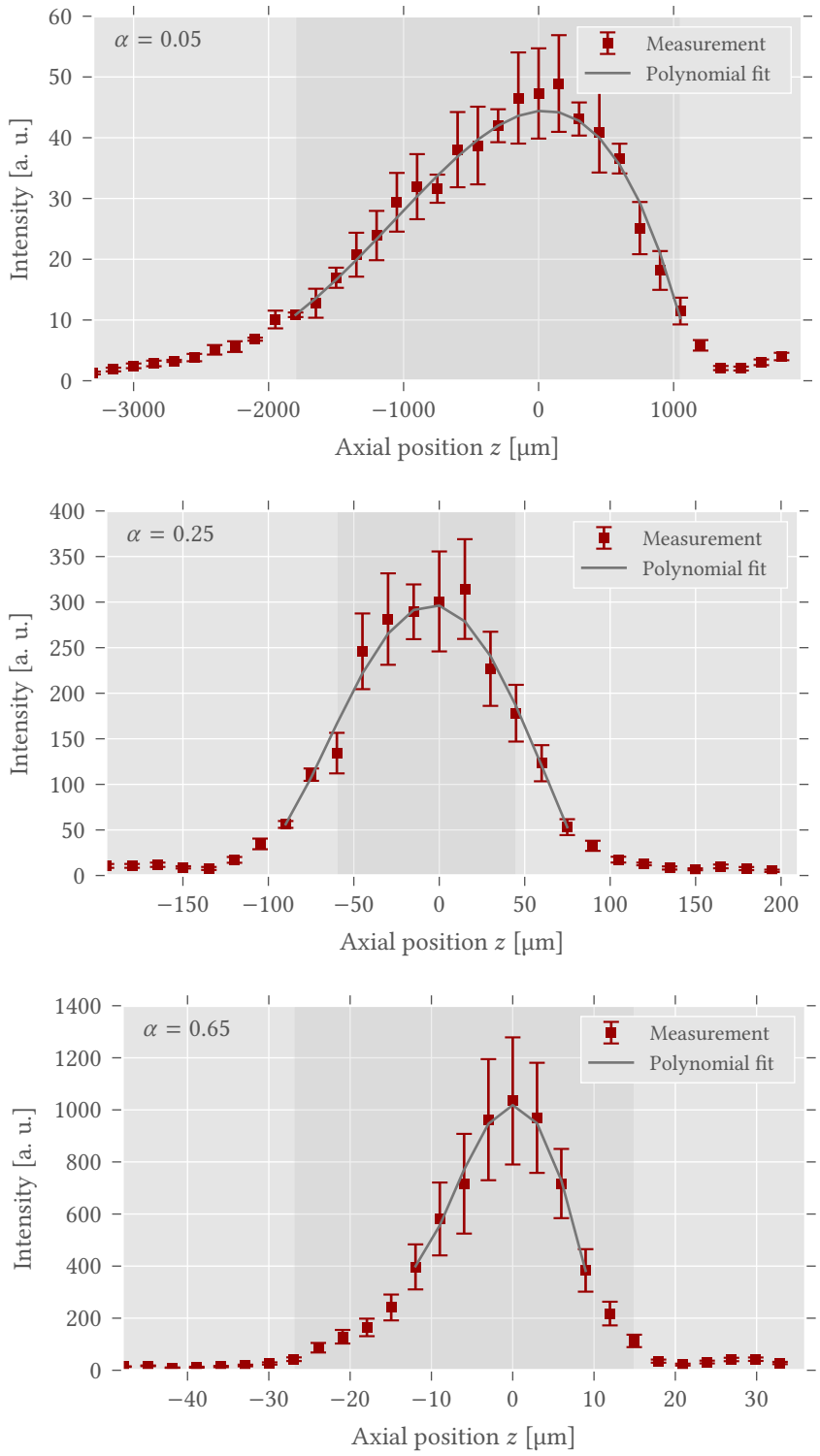

FIGURE 5.10: *Measured axial beam profiles with quartic fit for* $a = 0.5, 2.5,$ *and* 6.5 mm *(from top to bottom).* The axial profiles have been fitted with quartic polynomials, to get the harmonic approximation and higher order corrections. The shaded area marks the first dataset with lower intensity. Please note the different z ranges. All axial profiles are shown in Appendix A.

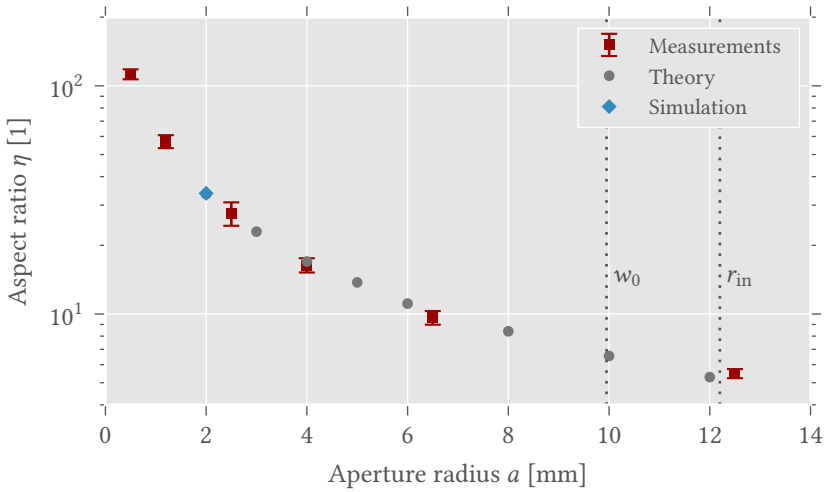

FIGURE 5.11: *Measured aspect ratios of the focussed truncated beam as a function of the aperture radius.* It can be clearly seen, that the aspect ratio of the trap increases very rapidly, when the radius drops below the beam waist w_0 (red rectangles). The results of the approximate theory of Section 4.4 and a data point of the exact simulation (blue diamond) are plotted for comparison as well (grey circles). Astonishingly, the theoretical values matches very well with the measurements for radii below the beam waist. Beam waist w_0 and entrance aperture of the objective r_{in} are marked as vertical dotted lines.

Therefore, it is crucial to know the precise shape of the potential, because we will finally do high-precision measurements with our experiment. The calculated coefficients according to (5.3) of the respective trap profiles are listed in Table 5.4 for the axial fits and in Table 5.5 for the radial fits. These results can be used, to eventually calculate perturbative corrections to the energies and the wave functions of the harmonic predictions.

TABLE 5.4: *Results of the quartic fit of the measured axial profiles.* The quantities k_2, k_3, and k_4 correspond to the coefficients of the different orders in (5.3) and a is the aperture radius.

a [mm]	$k_{2,\parallel}$ [μm^{-2}]	$k_{3,\parallel}$ [μm^{-3}]	$k_{4,\parallel}$ [μm^{-4}]
0.5	$2.37 \pm 0.13 \times 10^{-5}$	$9.3 \pm 1.8 \times 10^{-9}$	$9.8 \pm 8.1 \times 10^{-13}$
1.2	$5.04 \pm 0.43 \times 10^{-4}$	$6.0 \pm 6.4 \times 10^{-8}$	$1.04 \pm 0.41 \times 10^{-9}$
2.5	$4.97 \pm 0.68 \times 10^{-2}$	$2.4 \pm 2.3 \times 10^{-5}$	$2.01 \pm 0.81 \times 10^{-6}$
4.0	$4.13 \pm 0.59 \times 10^{-1}$	$1.38 \pm 0.70 \times 10^{-3}$	$9.9 \pm 4.5 \times 10^{-5}$
6.5	8.1 ± 1.1	$1.35 \pm 0.56 \times 10^{-1}$	$1.52 \pm 0.98 \times 10^{-2}$
12.5	7.88 ± 0.72	$3.2 \pm 2.0 \times 10^{-1}$	$2.3 \pm 1.8 \times 10^{-2}$

TABLE 5.5: *Results of the quartic fit of the measured radial profiles.* The quantities k_2, k_3, and k_4 correspond to the coefficients of the different orders in (5.3) and a is the aperture radius. For the values without uncertainties, the fits did not yield these, due to the small number of data points compared to the number of fit parameters.

a [mm]	$k_{2,\perp}$ [μm^{-2}]	$k_{3,\perp}$ [μm^{-3}]	$k_{4,\perp}$ [μm^{-4}]
0.5	$2.99 \pm 0.25 \times 10^{-1}$	$1.58 \pm 0.73 \times 10^{-3}$	$4.8 \pm 1.6 \times 10^{-4}$
1.2	1.64 ± 0.16	$6.2 \pm 7.0 \times 10^{-3}$	$1.06 \pm 0.32 \times 10^{-2}$
2.5	$3.79 \pm 0.73 \times 10^{1}$	$4.7 \pm 3.4 \times 10^{-1}$	1.45 ± 0.55
4.0	1.11×10^{2}	1.8	8.94
6.5	7.52×10^{2}	2.0	1.14×10^{2}
12.5	2.37×10^{2}	5.0×10^{-1}	3.65×10^{1}

5.2.3 *Comparison between simulation and measurement*

Finally, we want to know, how well the theoretical predictions of the microtrap potential match the experimental measurements. Firstly, we will compare the resulting intensity profiles of theory and experiment.

For an aperture radius $a = 1.2\,\text{mm}$[25] the simulation, as explained in Section 4.3, has been carried out. The exact distance between aperture and lens plane d_1, that is necessary for the simulation, is not easily obtained. The reason is the objective: The simulation assumes for simplicity a thin lens with well defined plane, yet the objective is a complex lens system with more optical components to which an effective focal length can be assigned. Furthermore, it is not clear what impact the interplay of the various optical components has on the resulting profile. Thus, the distance has been roughly estimated and set to $d_1 = 120\,\text{mm}$. The simulation has also been done for the values 100 and 150 mm, but the difference with respect to the main peak was rather negligible and none of the profiles could reproduce the experimentally measured smaller peaks, as will be discussed momentarily.

[25] *This radius has been chosen, as it is still feasible with the simulation and as it has been measured.*

The resulting axial and radial profile is shown in Figure 5.12 (blue circles), together with the profiles of the measurement (red rectangles). Additionally, the resulting profile of the approximate theoretical model (see Section 4.4) is plotted as well (solid grey line), although it uses the paraxial approximation and assumes the aperture to be in the lens plane (i. e. $d_1 = 0$). Even though the theory for the simulation is quite simple and considered only as a rough estimate, its resulting profile matches astonishingly well the experimental measurement within the uncertainties. Especially the symmetry of the main peak of the axial profile is predicted well. The approximate theory model fails to reproduce this feature of the profile. This is not surprising, as it is only valid for $d_1 = 0$, which is clearly not the case. The small features of the diffraction fringes at the sides cannot be fully reproduced by the theory, but in the end these details do not matter for the physics in the trap.

Last but not least, we want to compare the aspect ratios of theory and experiment. As already explained in Section 4.3.3, we could carry out the simulation—with usable results—only for aperture radii smaller than 3 mm,

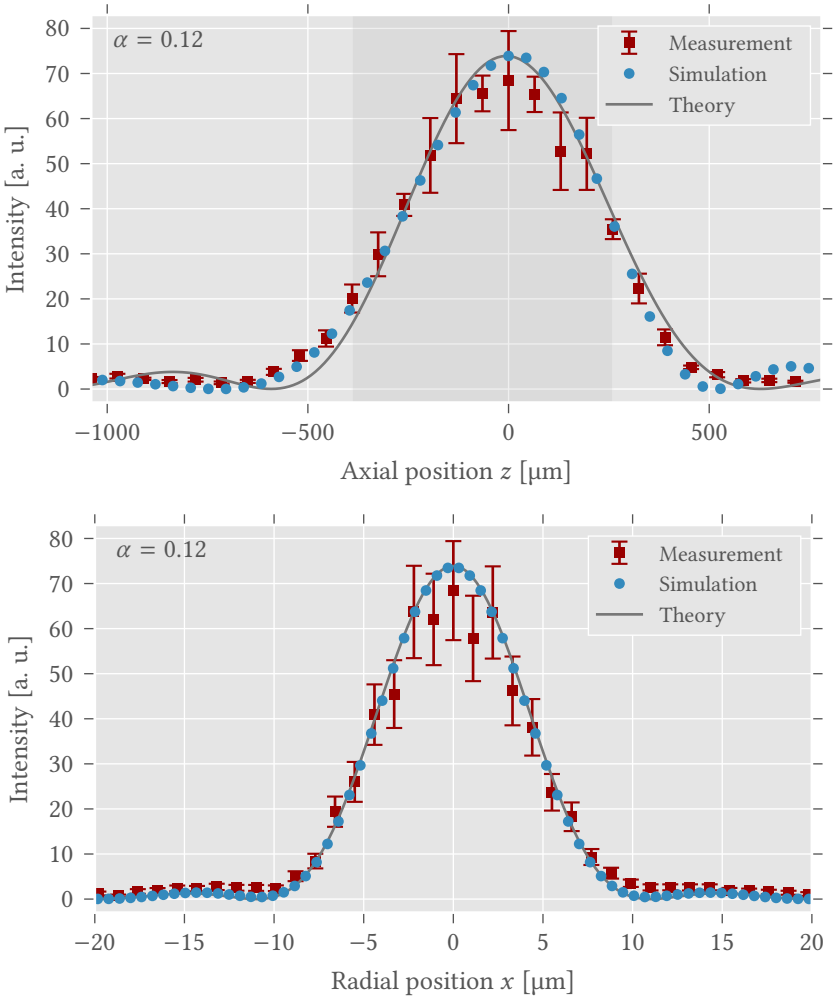

FIGURE 5.12: *Comparison of the axial and radial profile between experimental measurement and theory.* The experimentally measured profiles (red rectangles) along axial axis (top) and radial axis (bottom) are compared for $a = 1.2\,\text{mm}$ with the results of a simulation with the same parameters and a distance between aperture and lens $d_1 = 120\,\text{mm}$ (blue circles). Additionally, the theoretical prediction of the approximate theory, as discussed in Section 4.4 is plotted as a grey line. Considering the simplifying assumptions of the theory, the results match the actual profile astonishingly well. However, the simplified theory model cannot reproduce the symmetry of the profile as it assumes $d_1 = 0$.

such that the interesting region is not fully reachable. Thus, we will only compare the experimental values with the results of the approximate theoretical model of Section 4.4, even though it cannot fully reproduce the actual symmetry of the profile, as discussed previously. The aspect ratios of both, measurements (red rectangles) and calculations (grey circles), are plotted in Figure 5.11. Surprisingly, the results of the theory match very well with those of the experiment within the uncertainties. It seems, that both deviate for radii larger than the beam waist w_0, which could be explained by the breakdown of the paraxial approximation. However, there are to few data points to draw reliable conclusions, especially because the experimental results for $a = 12.5\,\mathrm{mm}$ have to be taken with care.

In total, the measurements yield interesting and satisfactory results for our method to change the aspect ratio of the trap in a controlled way. Furthermore, the theory can describe the shape and the properties of the trap depending on the truncation ratio of the incident beam very well, despite its simplicity. If the exact shape of the potential is not completely important, the approximate model gives very good estimates of the shape and parameters of the trap. This knowledge is very valuable, as this model allows to just write down the full three-dimensional profile with an analytical expression.

And for future experiments to study few-body physics in the quasi-one-dimensional regime, this method can be used, to dynamically increase the aspect ratio of the microtrap.

6 CONCLUSION AND OUTLOOK

We want to study one-dimensional physics on few-Fermion systems with our experiment—especially the emergence of the Anderson orthogonality catastrophe. It allows to deterministically prepare few Fermions in a tight optical dipole trap with high fidelity. However, this trap has a waist of 1.2 µm and thus only an aspect ratio of five. In order to remain in the one-dimensional limit, we have to increase the aspect ratio of the trap.

In this thesis, we presented a method to achieve this, with minor changes to the existing setup: An aperture truncates the Gaussian laser beam, that creates the optical trapping potential, leading to a larger beam at the focus and increasing thereby the aspect ratio. We have studied in detail, how this truncation of the beam affects the properties and the shape of the trap with both, theoretical calculations and experimental measurements of the beam profile.

We have shown, that this method allows to increase the aspect ratio of the trap in a controlled way. Yet, for small truncation ratios diffraction patterns and an asymmetry along the axial direction emerge. The theoretical calculations showed, that the latter arises, when the aperture is placed outside the focal plane of the objective. The shape of the axial profile determines the physics of the system, therefore, the resulting anharmonicities due to an asymmetry will change the wave functions and lead to non-equidistant energy levels in the trap. Due to the size of the objective (~120 mm, focal length ~20 mm), the aperture cannot be placed in the focal plane, such that the distance between these two components has to be as small as possible.

Furthermore, the theory has proven to match the experimental measurements well, despite its simplicity. Even for the approximate theoretical model by [Hor+03], which uses the paraxial approximation and assumes the aperture to be in the lens plane, we observed agreement in the rough shape of the potential and in the aspect ratios. An advantage of this model is, that it gives an analytic expression of the three-dimensional profile around the focus, enabling us to do quick estimates.

In conclusion, we can use this method to change the aspect ratio of the trap and study 1D physics. The limit of this method will be the power loss due to truncation. It lowers the trap depth, leading finally to a strong reduction of the trapping frequencies.

The next step is to mount the truncation setup into the real experiment. There, the trap frequencies can be directly measured by preparing particles in the trap and applying *trap modulation spectroscopy* [e. g., Wen13], and compared with the results of the characterization of the potential shape. This method allows also to measure the energy differences between higher ex-

cited states, which will decrease with higher excitations due to the anharmonicity of the potential.

As mentioned earlier, the power loss due to truncation leads to decreased trapping frequencies, and the total power of the laser beam cannot be increased arbitrarily to compensate this effect. As a consequence, it is not sensible to increase the aspect ratio to very high values, because the resulting small trap frequencies will reduce the precision of our measurements drastically.

Furthermore, the dynamical change of the aspect ratio, by suing the servo motor, has to be implemented in the experimental sequence. The aperture radius can be changed on a timescale of several hundred milliseconds from open to closed aperture with an Arduino microcontroller. However, it is not clear yet, whether this will allow us to achieve an equally good preparation fidelity for a dynamically changed trap.

In the end, we want an aspect ratio between 10 and 20. This will allow us to study, whether the quasi-particle residue approaches zero for an increasing number of majority particles in the system, which would show the emergence of the Anderson orthogonality catastrophe.

A

EXPERIMENTALLY MEASURED PROFILES OF THE MICROTRAP

In this appendix all experimentally measured profiles can be found, as presented in Section 5.2. The two-dimensional profiles in the zx-plane are shown in Figures Figure A.1 and Figure A.2. The same profiles in logarithmic scale are plotted in Figures Figure A.3 and Figure A.4. And finally the axial profiles along with the quartic fits are shown in Figures Figure A.5 and Figure A.6.

In the following, a denotes the radisu of the aperture, truncating the incident beam of waist $w0 = 9.95\,\text{mm}$, and $\alpha = a/w_0$ the truncation ratio. The axial axis z corresponds to the propagation axis of the light beam, and negative values of z point toward the objective.

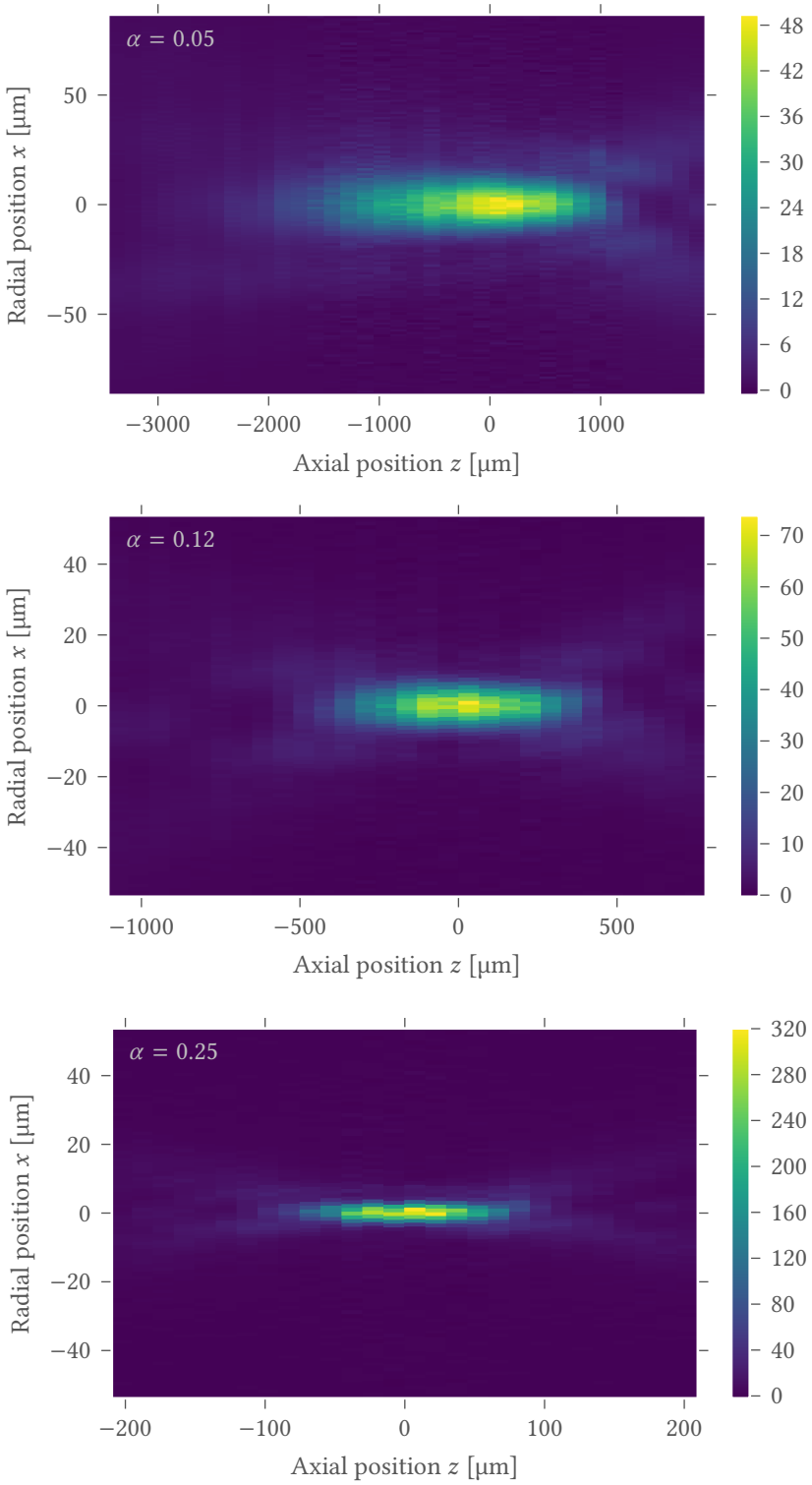

FIGURE A.1: *Measured two-dimensional cuts of the beam profiles for* $a = 0.5, 1.2$ *and* 2.5 mm *(from top to bottom).* Please note the different z and x ranges.

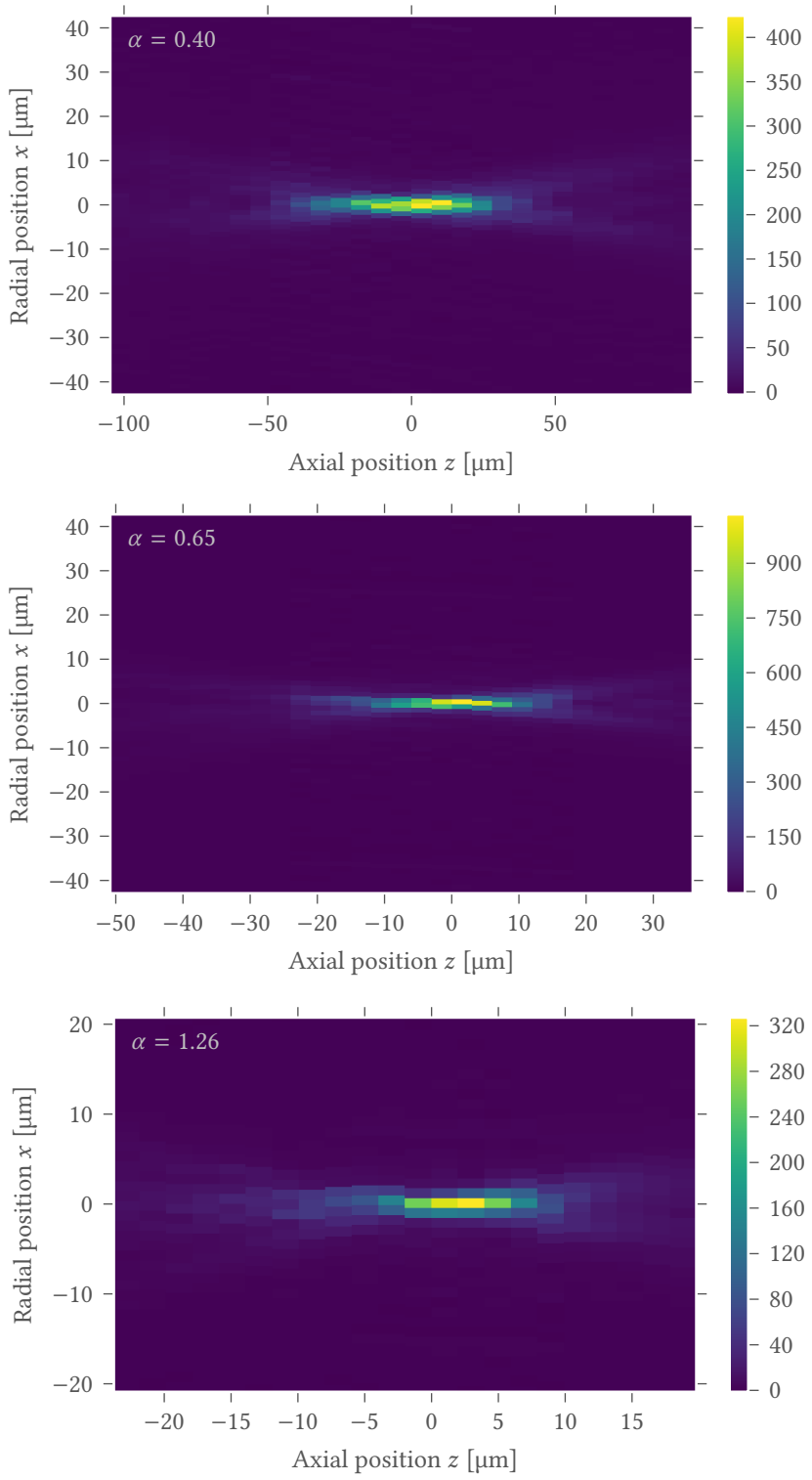

FIGURE A.2: *Measured two-dimensional cuts of the beam profiles for* $a = 4.0, 6.5$ *and* 12.5 mm *(from top to bottom).* Please note the different z and x ranges.

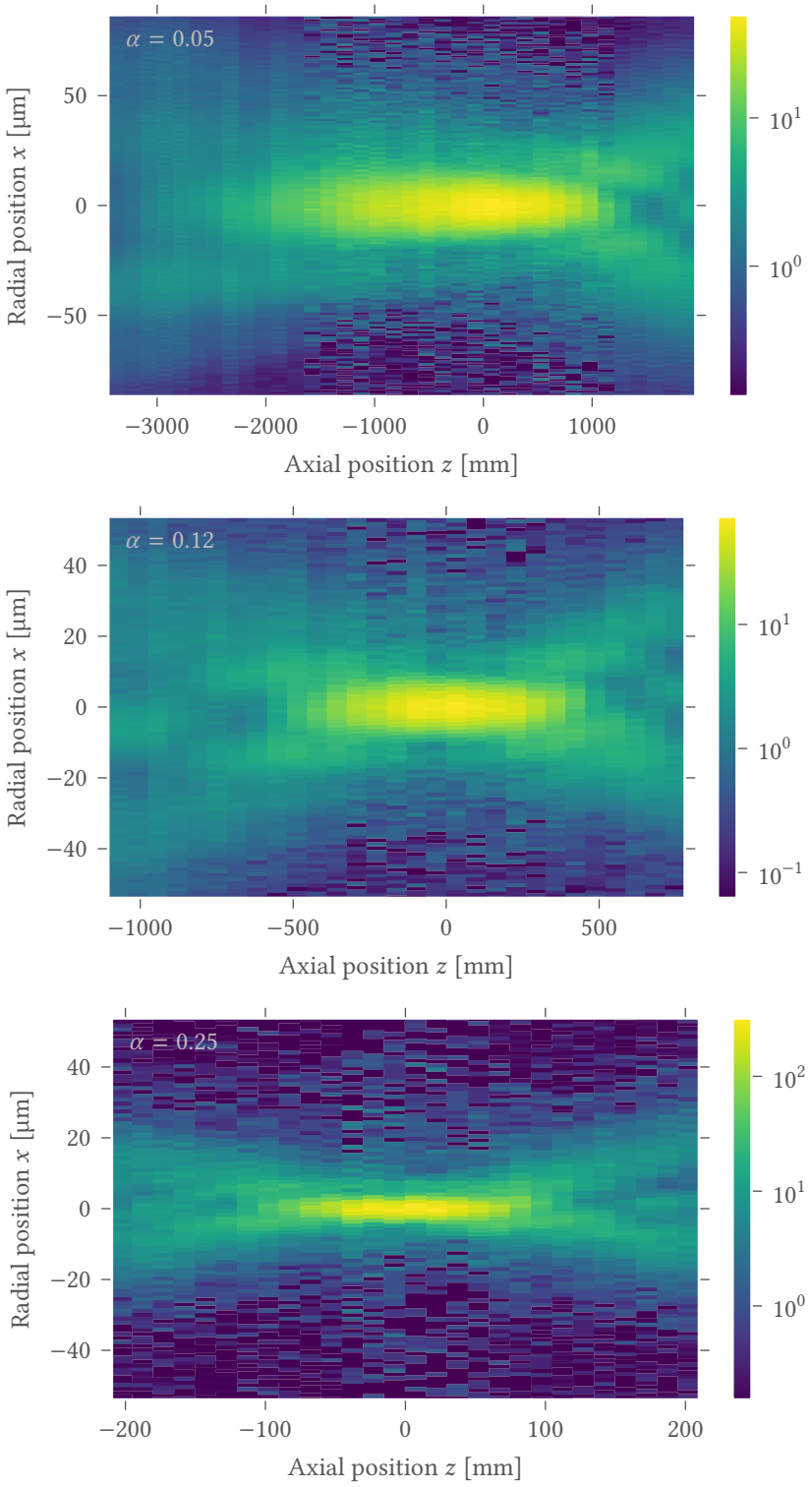

FIGURE A.3: *Measured two-dimensional cuts of the beam profiles for* $a = 0.5, 1.2$ *and* 2.5 mm *(from top to bottom, logarithmic scaling).* Please note the different z and x ranges.

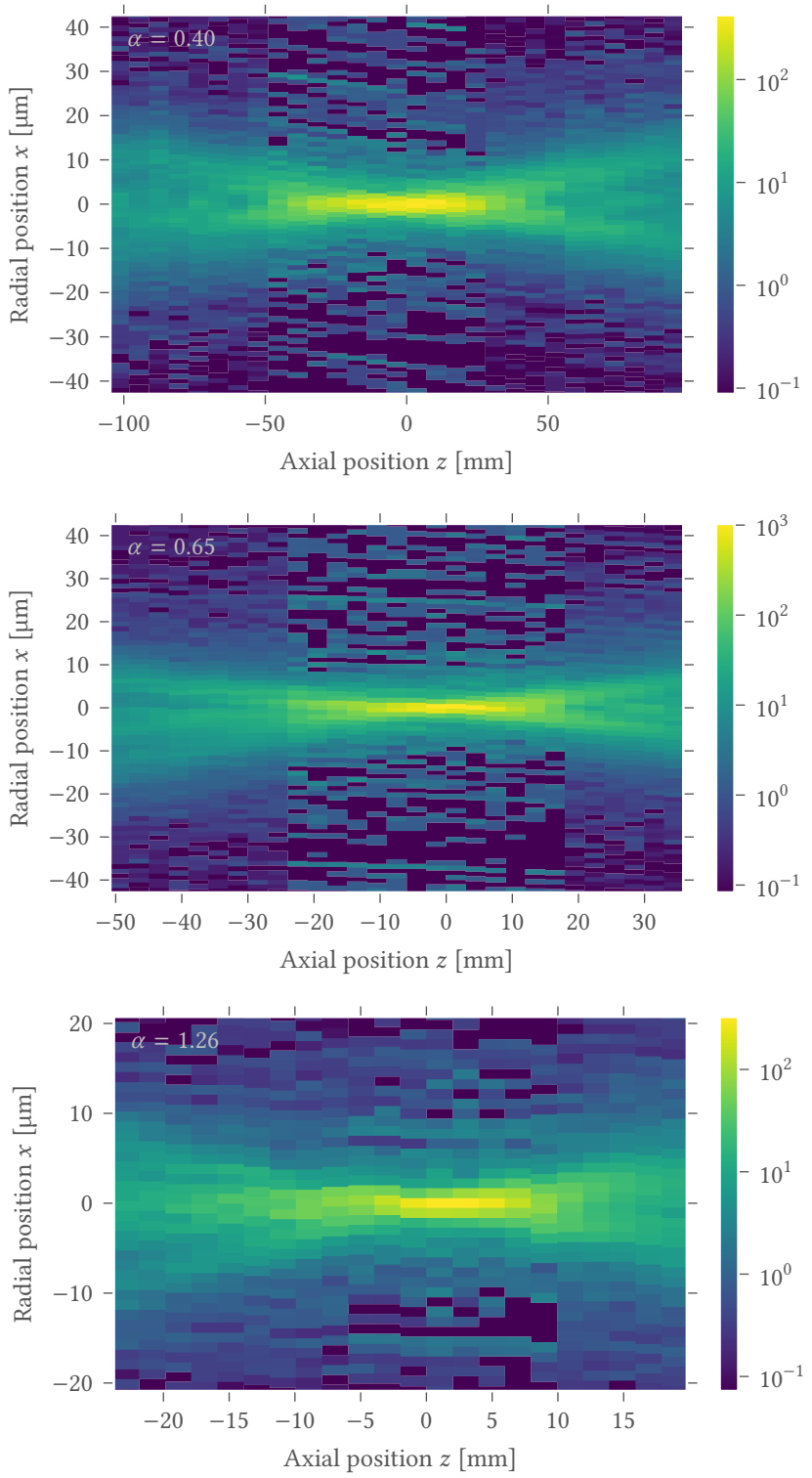

FIGURE A.4: *Measured two-dimensional cuts of the beam profiles for* $a = 4.0, 6.5$ *and* 12.5 mm *(from top to bottom, logarithmic scaling).* Please note the different z and x ranges.

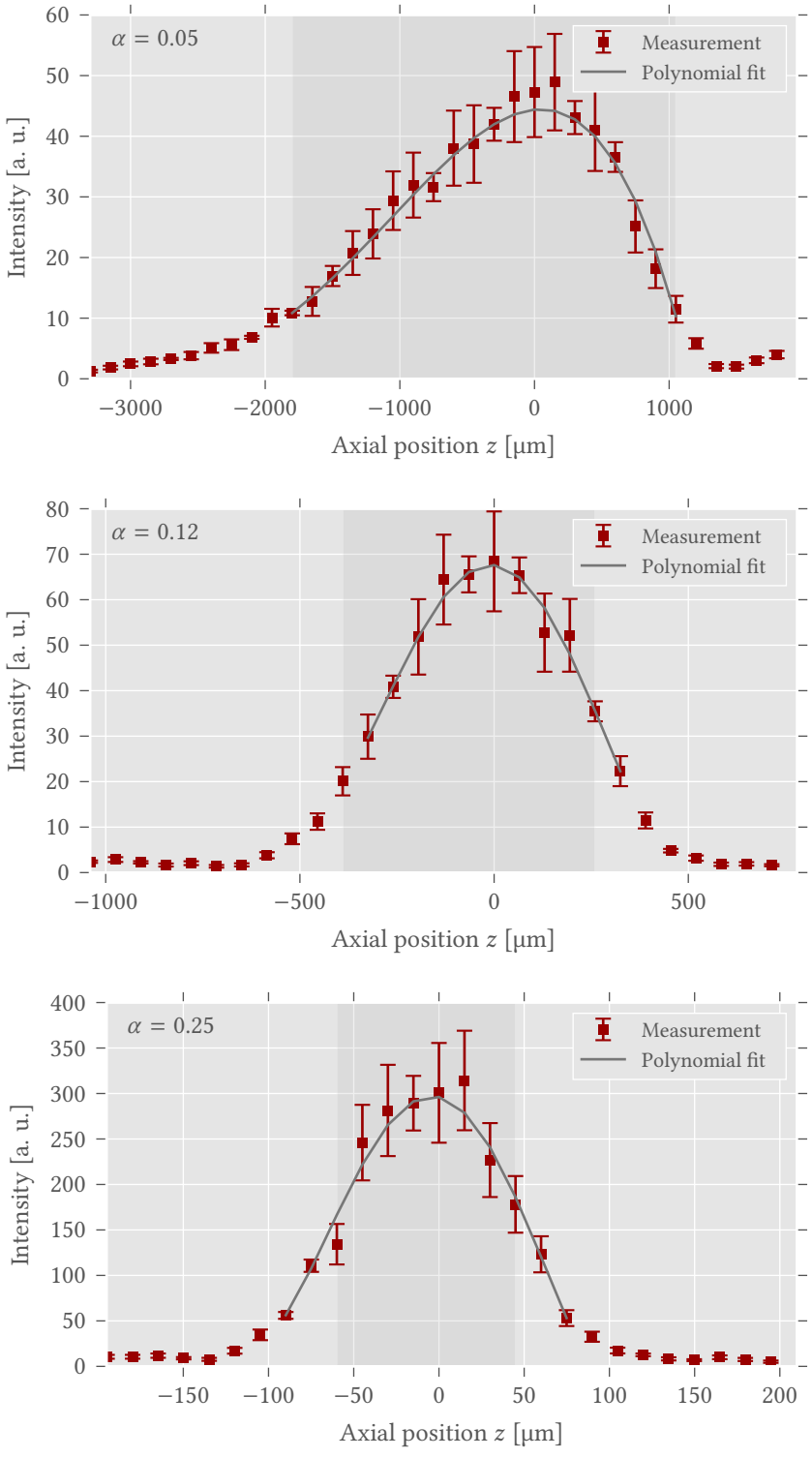

FIGURE A.5: *Measured axial beam profiles with quartic fit for* $a = 0.5, 1.2$ *and* $2.5\,\mathrm{mm}$ *(from top to bottom).* The axial profile has been fitted with quartic polynomial to get the harmonic approximation and higher order corrections. The shaded area marks the first dataset with lower intensity. Please note the different z ranges.

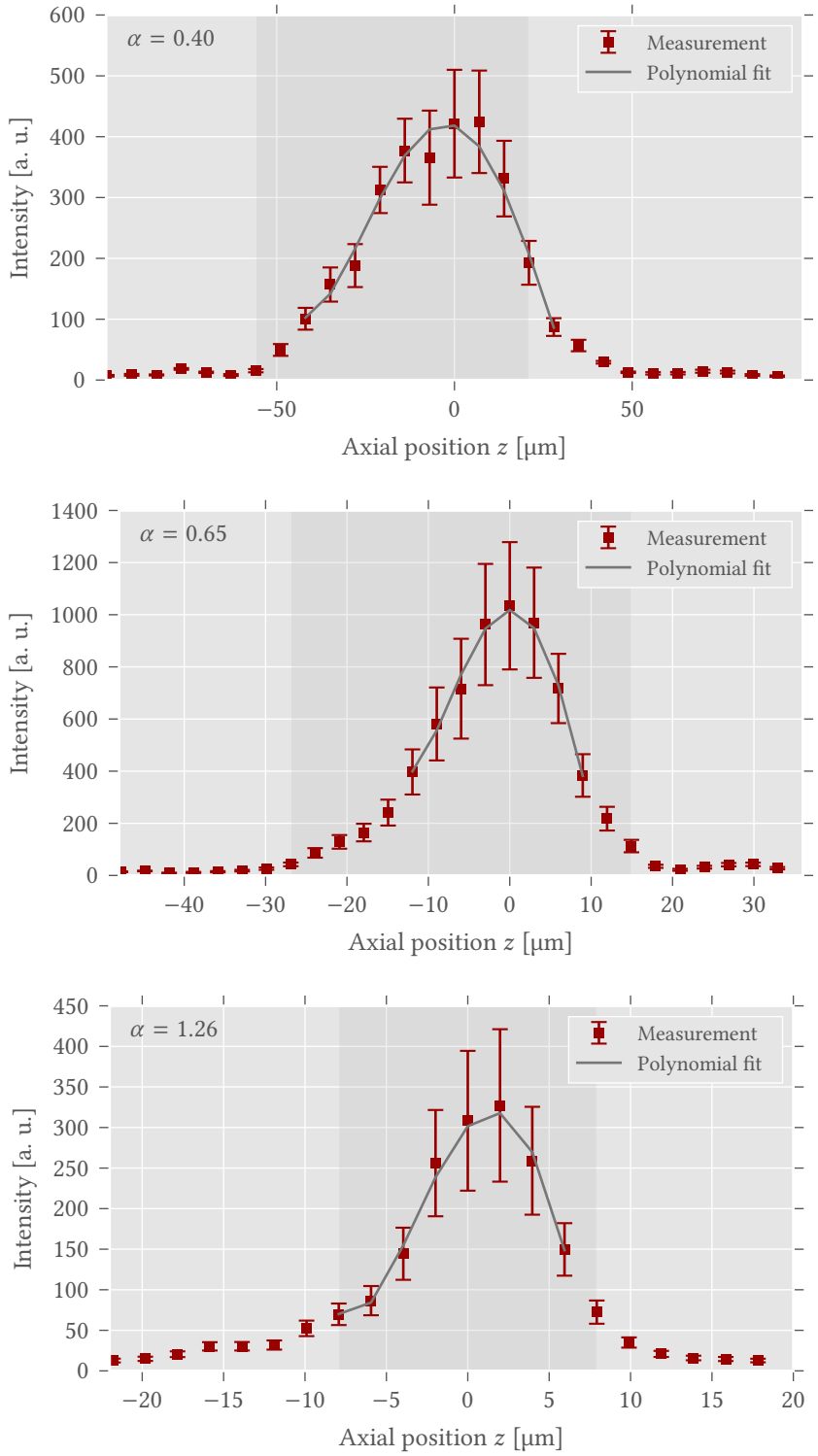

FIGURE A.6: *Measured axial beam profiles with quartic fit for* $a = 4.0, 6.5$ *and* $12.5\,\mathrm{mm}$ *(from top to bottom).* The axial profile has been fitted with quartic polynomial to get the harmonic approximation and higher order corrections. The shaded area marks the first dataset with lower intensity. Please note the different z ranges.

B

APERTURE MOUNT

As explained in Section 5.1.1, an aperture mount has been designed, in order to stably change the aperture radius, and thus the aspect ratio during the experimental sequence.

B.1 SKETCHES OF THE DESIGNED PARTS

In total three additional pieces had to be designed and manufactured. Here you can find the sketches (true to scale) of these three pieces. The ring with the end stops of the gears is sketched in Figure B.1. Figure B.2 shows the sketch of the servo mount, and Figure B.3 shows that of the post adapter.

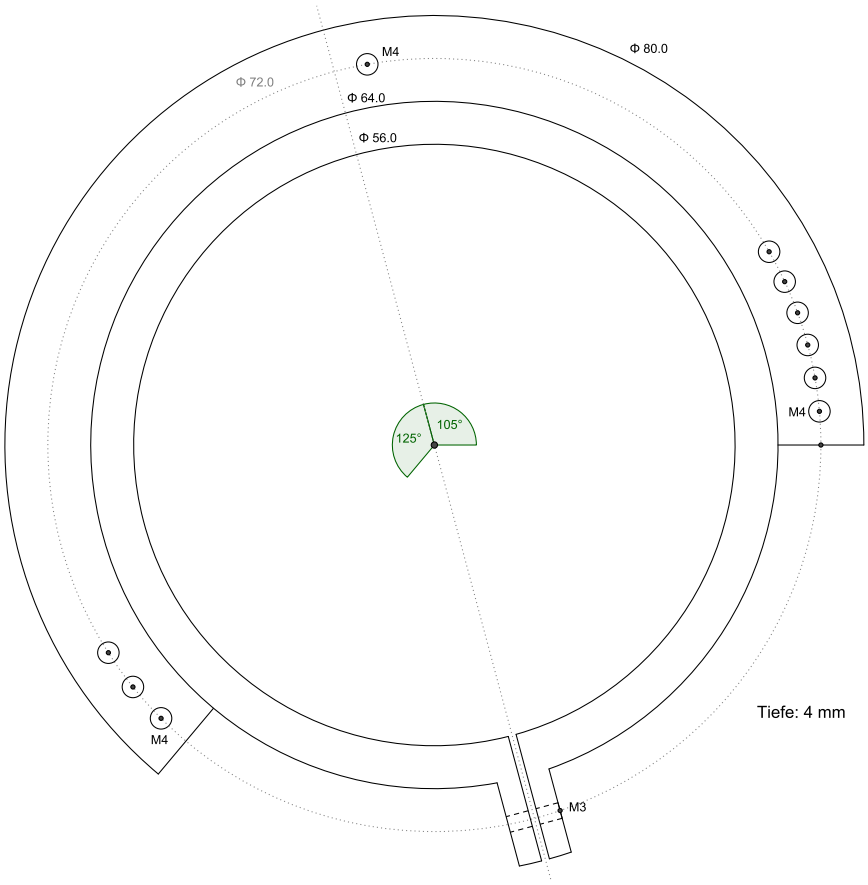

FIGURE B.1: Sketch of ring with the end stops for the aperture mount.

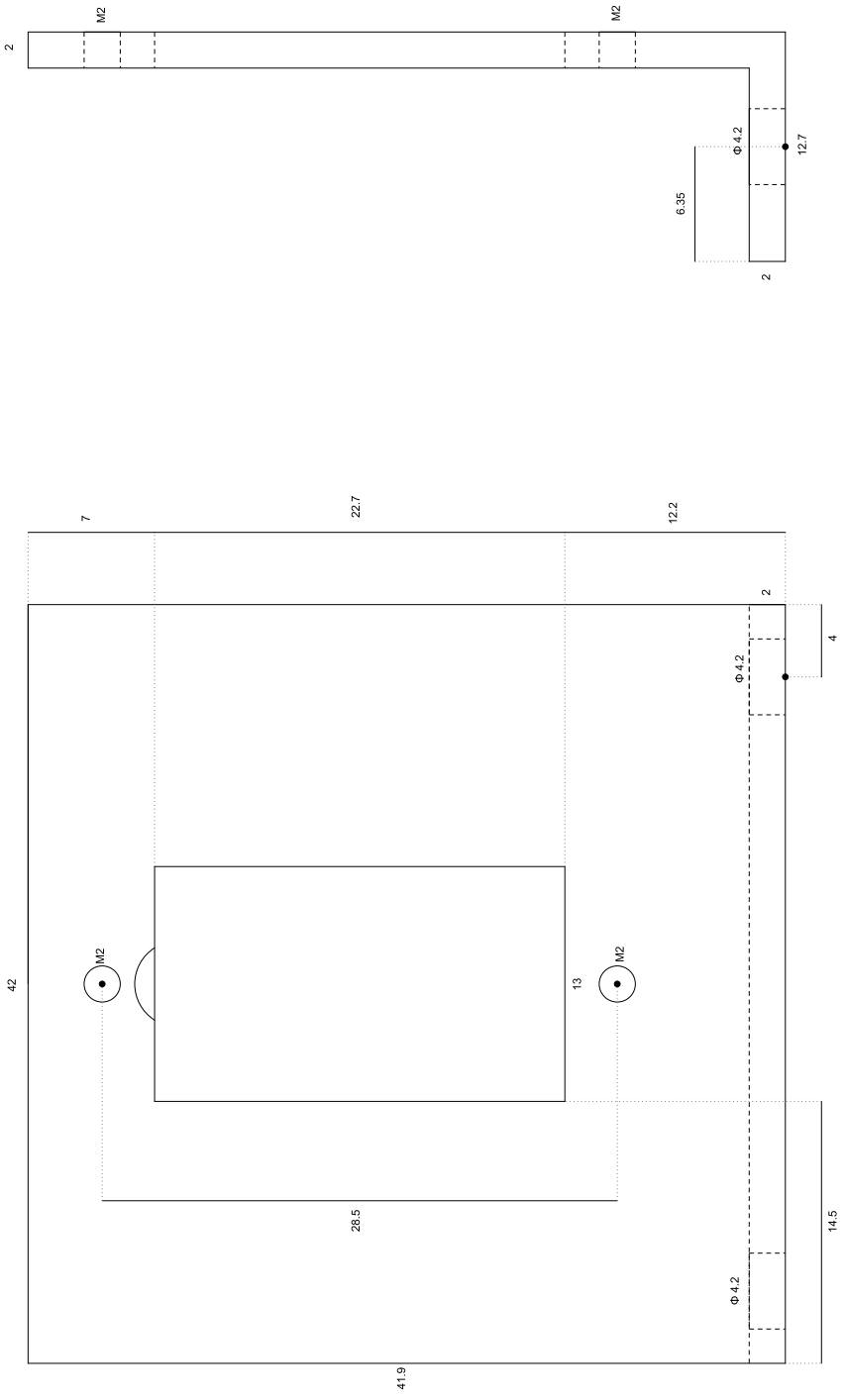

Figure B.2: Sketch of servo motor mount for the aperture mount.

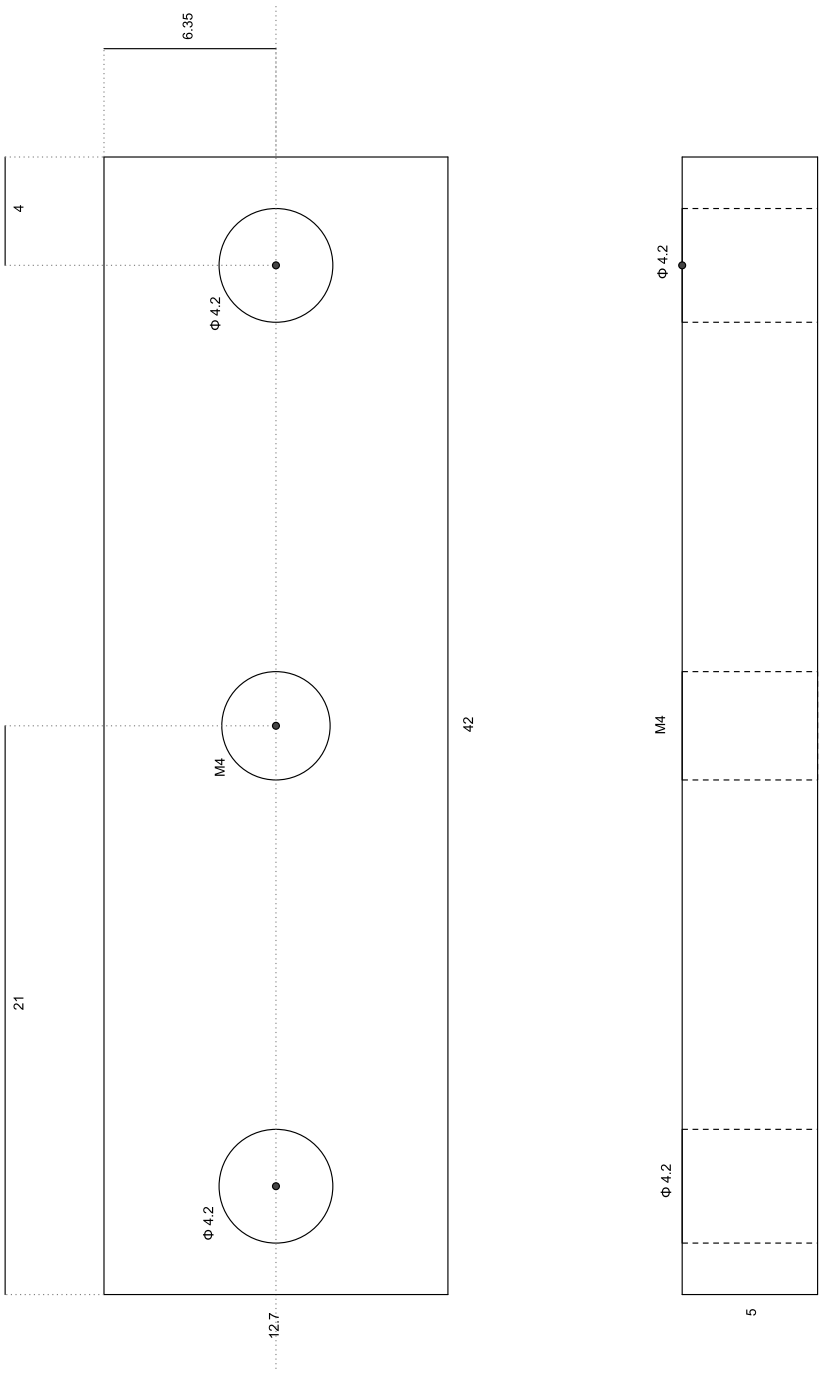

FIGURE B.3: Sketch of the post adapter for the aperture mount.

B.2 APERTURE RADII

Every hole for an endpoint corresponds to a different aperture radius. In the following table, the radii for all holes are listed.

TABLE B.1: *Correspondence between endpoint holes of the mount and aperture radii for the first starting point hole.* The starting point stays fixed for all different endpoint holes. The holes are counted from the end of the mount on the right side.

Hole number	a [mm]	
–	0.50 ± 0.05	Closed aperture
3	1.20 ± 0.05	
4	2.50 ± 0.05	
5	4.00 ± 0.05	
6	5.10 ± 0.05	
7	6.50 ± 0.05	
8	7.60 ± 0.05	
9	8.85 ± 0.05	
10	10.10 ± 0.05	
11	11.40 ± 0.05	
12	12.50 ± 0.05	Open aperture

C

BEAM QUALITY: ASTIGMATISM

The high-resolution objective creating the microtrap has to be very precisely aligned with respect to the window of the vacuum chamber and to the incident light. As reference, we use the axis orthogonal to the window. It has been shown, that the objective performs best, when its axis is tilted by a specific angle with respect to the reference axis, and when the incident light beam is orthogonal to the window. At this optimal alignment, the aberrations on the beam at the focus are minimized. Nevertheless, an observed astigmatism could not be eliminated or even altered by varying these degrees of freedom. The result is the following: The focussed light beam has two different foci in the two radial axes. I. e. the radial profile has an elliptical form, and becomes circular at an effective focus between the two real foci of the two axes.

We have analysed the astigmatism, by taking images of the radial profile at different axial positions around the focus, and fitting them with a two-dimensional Gaussian according to (5.2). The images were taken using a microscope objective with a magnification of $M = 69 \pm 6$ (Melles Griot, $r = (0.92 \pm 0.10)\,\mu\text{m}$ at 1064 nm [Ber13, p. 39]) and a CMOS camera (Guppy Pro F-031B, 5.6 µm pixel size). The obtained beam width of the two axes is plotted in Figure C.1 on the axial position. The results clearly show, that the foci of the two axes are apart by roughly 5 to 6 µm. Furthermore, we observe an effective beam waist of approximately 1.2 µm.

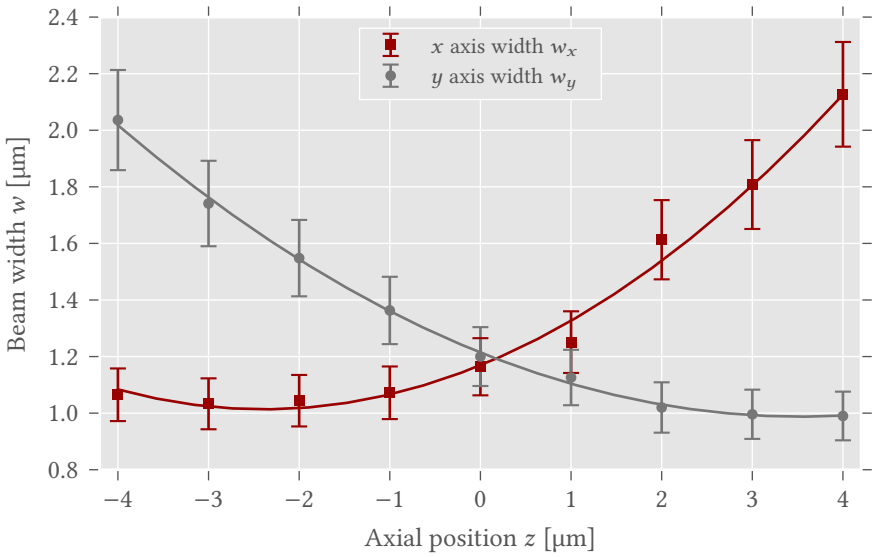

FIGURE C.1: *The beam width of the two radial axes depending on the axial position, demonstrating the astigmatism of the beam at the focus.* An astigmatism between 5 to 6 µm and an effective beam waist of 1.2 µm are apparent. The images are taken with a microscope objective. The solid lines are guides to the eye.

D

PYTHON CODE SNIPPETS

In this appendix, minimal Python code examples of the following applications are listed:

- Image capture with the Raspberry Pi camera (Section 5.1.2.3)
- Raw data extraction from a captured image (Section 5.1.2.3)
- General two-dimensional Gaussian function with angle (Section 5.1.4)
- Fitting function with implemented binning (Section 5.1.4)

LISTING D.1: *Minimal Python code for an image capture with the Raspberry Pi camera.* A JPEG image including the raw Bayer data is captured with fixed exposure and gain settings and saved into a file.

```
#!/usr/bin/python3
# this script assumes the use of the RPi camera module version 2

import picamera as pic

with pic.PiCamera() as camera:
    # set full resolution
    camera.resolution = (3280, 2464)
    camera.exposure_mode = 'off'
    # fix settings
    camera.framerate = 20
    camera.awb_mode = 'off'
    camera.awb_gains = 1.
    camera.shutter_speed = 50000
    # capture image and save it
    camera.capture('/home/pi/camera/single/camera.jpg', 'jpeg', bayer
        =True)
```

LISTING D.2: Minimal Python code to extract the raw data from a captured image.

```
#!/usr/bin/python3
# this script assumes the use of the RPi camera module version 2

import numpy as np


# get filename
filename = '/path/to/image/file.jpg'

# filename of the file to save the data
filename_data = filename[:-4] + '.npy'
```

```
12
13 # open file into Byte Stream
14 stream = open(f, 'rb')
15
16 # Extract the raw Bayer data from the end of the stream, check the
17 # header and strip if off before converting the data into a numpy
       array
18 data = stream.read()[-10270208:]
19 assert data[:4] == b'BRCM'
20 data = data[2**15:]
21 data = np.fromstring(data, dtype=np.uint8)
22
23 # The data consists of 1952 rows of 3264 bytes of data. The last 8
       rows
24 # of data are unused (they only exist because the actual resolution
       of
25 # 1944 rows is rounded up to the nearest 16). Likewise, the last 24
26 # bytes of each row are unused (why?). Here we reshape the data and
27 # strip off the unused bytes
28 data = data.reshape((2480, 4128))[:2464, :4100]
29
30 # Horizontally, each row consists of 2592 10-bit values. Every four
31 # bytes are the high 8-bits of four values, and the 5th byte contains
32 # the packed low 2-bits of the preceding four values. In other words,
33 # the bits of the values A, B, C, D and arranged like so:
34 #
35 #  byte 1   byte 2   byte 3   byte 4   byte 5
36 # AAAAAAAA BBBBBBBB CCCCCCCC DDDDDDDD AABBCCDD
37 #
38 # Here, we convert our data into a 16-bit array, shift all values
       left
39 # by 2-bits and unpack the low-order bits from every 5th byte in each
40 # row, then remove the columns containing the packed bits
41 data = data.astype(np.uint16) << 2
42 for byte in range(4):
43     data[:, byte::5] |= ((data[:, 4::5] >> ((4 - byte) * 2)) & 0b11)
44 data = np.delete(data, np.s_[4::5], 1)
45
46 # save data to file
47 np.save(filename_data, data)
```

LISTING D.3: Python code for a general two-dimensional Gaussian function with angle between its main axes and the data grid axes.

```
1 #!/usr/bin/python3
2
3 import numpy as np
4
5 # Gauss function in 2D
6 def fct_gaussian_2d(r, x0, y0, sigma_x, sigma_y, amplitude, angle,
       offset):
7     """Create a Gaussian profile in 2D.
```

```
8
9       The Gaussian has two separate beam waist
10      in the two axes and allows an arbitrary angle of the axes to the
            axes of
11      the coordinate data.
12
13      Parameters
14      ----------
15      r : ndarray
16          Meshgrid of the x and y coordinate arrays.
17      x0 : float
18          x centre of the Gaussian.
19      y0 : float
20          y centre of the Gaussian.
21      sigma_x : float
22          Waist (1/e^2 width) of the Gaussian in the x axis.
23      sigma_y : float
24          Waist (1/e^2 width) of the Gaussian in the y axis.
25      amplitude : float
26          The amplitude of the Gaussian at the centre.
27      angle : float
28          The angle between one of the main axes of the Gaussian and
                the axes of
29          the data grid.
30      offset : float
31          Constant overal offset.
32      """
33
34      # unpack coordinate arrays
35      x, y = r
36
37      # convert angle from degree to radians
38      angle_rad = np.deg2rad(angle)
39
40      # prefactor
41      factor = amplitude
42
43      # argument of the exponetial
44      a = 2. * np.cos(angle_rad)**2 / sigma_x**2 + \
45          2. * np.sin(angle_rad)**2 / sigma_y**2
46      b = - np.sin(2. * angle_rad) / sigma_x**2 + \
47          np.sin(2. * angle_rad) / sigma_y**2
48      c = 2. * np.sin(angle_rad)**2 / (sigma_x**2) + \
49          2. * np.cos(angle_rad)**2 / (sigma_y**2)
50
51      argument = a * (x - x0)**2 - 2*b * (x - x0) * (y - y0) + c * (y -
             y0)**2
52
53      # whole expression
54      g = factor * np.exp(-argument) + offset
55      return g
```

LISTING D.4: *Python code for a fitting function with binning.* The function implements a binning procedure that up-scales the coordinate grid, evaluates the chosen function and then down-samples the data to the original size. This model accounts for the „pixelization“ of the data, due to the finite pixel size of the camera chip.

```
#!/usr/bin/python3

import numpy as np

# Down-sampling a given data set
def sample_down(data, bin_size):
    """Scale down a given data set by summing up all data in a bin
    with defined size.

    Parameters
    ----------
    data : ndarray
        Two-dimensional data array to sample down.
    bin_size : int
        size of the bins to sum over.
    """

    # number of bins
    num_bins = (
            int(np.ceil(data.shape[0] / bin_size)),
            int(np.ceil(data.shape[1] / bin_size)))

    # split the input data into the bins
    splitted_h = np.array(np.hsplit(data, num_bins[1]))
    splitted = np.array(np.hsplit(splitted_h, num_bins[0]))

    # sum up the bins
    result = splitted.sum((2, 3))

    return result

# 2D binned fitting function
def fct_binned_2d(r, bin_size, fct, *args):
    """Create the profile of a function with binned data.

    For a chosen function the data is sampled up with a given bin
        size and
    then all data points in the bin are summed up.

    Parameters
    ----------
    r : ndarray
        Meshgrid of the x and y coordinate arrays.
    bin_size : int
        Number of sub-points every data pointwill be sampled to.
    fct : str
        Function to use. Currently only 'gaussian' for a Gaussian
        profile is available.
```

```
    args : tuple
        Arguments to pass to the function to create.
    """

    # available functions to bin
    fct_available = ['gaussian']

    # unpack coordinate arrays
    x, y = r

    # get coordinate params
    x_lims = [x[0, 0], x[0, -1]]
    y_lims = [y[0, 0], y[-1, 0]]
    x_step = x[0, 1] - x[0, 0]
    y_step = y[1, 0] - y[0, 0]
    x_size = x.shape[1]
    y_size = y.shape[0]

    # resample coordinates
    x_r, y_r = np.meshgrid(
        np.linspace(
            x_lims[0] - .5 * x_step,
            x_lims[1] + .5 * x_step,
            x_size * bin_size),
        np.linspace(
            y_lims[0] - .5 * y_step,
            y_lims[1] + .5 * y_step,
            y_size * bin_size),
        sparse=True)

    # create data
    if fct == 'gaussian':
        data = fct_gaussian_2d((x_r, y_r), *args)
    else:
        return False

    return sample_down(data, bin_size)
```

BIBLIOGRAPHY

[And+95] M. H. Anderson, J. R. Ensher, M. R. Matthews, C. E. Wieman, and E. A. Cornell. „Observation of Bose-Einstein Condensation in a Dilute Atomic Vapor“. In: *Science* 269.5221 (1995), pp. 198–201. DOI: 10.1126/science.269.5221.198 (cit. on p. 1).

[And67] P. W. Anderson. „Infrared catastrophe in fermi gases with local scattering potentials“. In: *Physical Review Letters* 18.24 (1967), pp. 1049–1051. DOI: 10.1103/PhysRevLett.18.1049 (cit. on pp. 1, 3).

[Bec16] J. H. W. Becher. „Towards Spin and Site-Resolved, Single-Atom Imaging of 6Li Atoms in a Multiwell Potential“. Master thesis. Ruprecht-Karls-Universität Heidelberg, 2016 (cit. on p. 17).

[Ber+03] T. Bergeman, M. G. Moore, and M. Olshanii. „Atom-atom scattering under cylindrical harmonic confinement: Numerical and analytic studies of the confinement induced resonance“. In: *Physical Review Letters* 91.16 (2003), p. 163201. DOI: 10.1103/PhysRevLett.91.163201 (cit. on p. 8).

[Ber13] A. Bergschneider. „Ultracold few-fermion systems in multiwell potentials“. Master thesis. Ruprecht-Karls-Universität Heidelberg, 2013 (cit. on pp. 13, 15, 18, 19, 36, 71).

[Bol+03] E. L. Bolda, E. Tiesinga, and P. S. Julienne. „Pseudopotential model of ultracold atomic collisions in quasi-one- and two-dimensional traps“. In: *Physical Review A* 68 (2003), p. 032702. DOI: 10.1103/PhysRevA.68.032702 (cit. on p. 8).

[Bra+95] C. C. Bradley, C. A. Sackett, J. J. Tollett, and R. G. Hulet. „Evidence of Bose-Einstein condensation in an atomic gas with attractive interactions“. In: *Physical Review Letters* 75.9 (1995), pp. 1687–1690. DOI: 10.1103/PhysRevLett.75.1687 (cit. on p. 1).

[Bus+98] T. Busch, B. G. Englert, K. Rzazewski, and M. Wilkens. „Two cold atoms in a harmonic trap“. In: *Foundations of Physics* 28.4 (1998), pp. 549–559. DOI: 0015-9018/98/0400-0549 (cit. on pp. 3, 5–8).

[Chi+10] C. Chin, R. Grimm, P. Julienne, and E. Tiesinga. „Feshbach resonances in ultracold gases“. In: *Reviews of Modern Physics* 82.2 (2010), pp. 1225–1286. DOI: 10.1103/RevModPhys.82.1225 (cit. on p. 12).

[Cir+12] J. I. Cirac and P. Zoller. „Goals and opportunities in quantum simulation“. In: *Nature Physics* 8.4 (2012), pp. 264–266. DOI: 10.1038/nphys2275 (cit. on p. 1).

[Coo+65] J. W. Cooley and J. W. Tukey. „An Algorithm for the Machine Calculation of Complex Fourier Series“. In: *Mathematics of Computation* 19.90 (1965), pp. 297–301 (cit. on p. 27).

[Dav+95] K. B. Davis, M. O. Mewes, M. R. Andrews, N. J. Van Druten, D. S. Durfee, D. M. Kurn, and W. Ketterle. „Bose-Einstein condensation in a gas of sodium atoms“. In: *Physical Review Letters* 75.22 (1995), pp. 3969–3973. DOI: 10.1103/PhysRevLett.75.3969 (cit. on p. 1).

[DeM99] D. S. DeMarco, B.; Jin. „Onset of Fermi Degeneracy in a Trapped Atomic Gas“. In: *Science* 285.5434 (1999), pp. 1703–1706. DOI: 10.1126/science.285.5434.1703 (cit. on p. 1).

[Fes62] H. Feshbach. „A unified theory of nuclear reactions. II“. In: *Annals of Physics* 19.2 (1962), pp. 287–313. DOI: 10.1016/0003-4916(62)90221-X (cit. on p. 12).

[Fey82] R. P. Feynman. „Simulating physics with computers“. In: *International Journal of Theoretical Physics* 21.6-7 (1982), pp. 467–488. DOI: 10.1007/BF02650179 (cit. on p. 1).

[Geh03] M. E. Gehm. „Properties of 6Li“. In: *Notes* (2003), pp. 1–33 (cit. on p. 12).

[Gri+99] R. Grimm, M. Weidemüller, and Y. B. Ovchinnikov. „Optical dipole traps for neutral atoms“. In: (1999) (cit. on pp. 1, 13, 20).

[Hor+03] Z. L. Horváth and Z. Bor. „Focusing of truncated Gaussian beams“. In: *Optics Communications* 222.1-6 (2003), pp. 51–68. DOI: 10.1016/S0030-4018(03)01562-1 (cit. on pp. 29, 32, 55).

[Hua+57] K. Huang and C. N. Yang. „Quantum-mechanical many-body problem with hard-sphere interaction“. In: *Physical Review* 105.3 (1957), pp. 767–775. DOI: 10.1103/PhysRev.105.767 (cit. on p. 7).

[IDE] IDEX Optics & Photonics. *All about Gaussian Beam Optics. Technical Notes*. URL: http://marketplace.idexop.com/store/SupportDocuments/All_About_Gaussian_Beam_OpticsWEB.pdf (visited on 08/11/2016) (cit. on pp. 19, 20).

[Idz+06] Z. Idziaszek and T. Calarco. „Analytical solutions for the dynamics of two trapped interacting ultracold atoms“. In: *Physical Review A - Atomic, Molecular, and Optical Physics* 74.2 (2006), pp. 1–14. DOI: 10.1103/PhysRevA.74.022712 (cit. on pp. 2, 3, 5, 6, 8).

[Jona] D. Jones. *Picamera module documentation. Raw Bayer data captures*. URL: https://picamera.readthedocs.io/en/release-1.12/recipes2.html#raw-bayer-data-captures (visited on 08/09/2016) (cit. on p. 38).

[Jonb] D. Jones. *Picamera module documentation*. Raspberry Pi Foundation. URL: http://picamera.readthedocs.io/ (visited on 08/09/2016) (cit. on p. 39).

[Ket+08] W. Ketterle and M. W. Zwierlein. „Making, probing and understanding ultracold Fermi gases“. In: *Rivista del Nuovo Cimento* 31.5-6 (2008), pp. 247–422. DOI: 10.1393/ncr/i2008-10033-1 (cit. on pp. 10, 13).

[Kli12] V. M. Klinkhamer. „An apparatus for few-fermion systems in multiple well potentials“. Master thesis. Ruprecht-Karls-Universität Heidelberg, 2012 (cit. on p. 18).

[Lan33] L. D. Landau. „Über die Bewegung der Elektronen in Kristalgitter“. In: *Phys. Z. Sowjetunion* 3 (1933), pp. 644–645 (cit. on p. 1).

[Lev+15] J. Levinsen, P. Massignan, G. M. Bruun, and M. M. Parish. „Strong-coupling ansatz for the one-dimensional Fermi gas in a harmonic potential“. In: *Science Advances* 1.6 (2015), p. 15. DOI: 10.1126/sciadv.1500197 (cit. on pp. 2, 4).

[Met+02] H. J. Metcalf and P. v. Straten. *Laser cooling and trapping*. Corr. 2. print. Graduate texts in contemporary physics. New York ; Berlin ; Heidelberg [u.a.]: Springer, 2002, XVI, 323 S. (Cit. on pp. 10, 13).

[Mur15] S. Murrmann. „Few-particle quantum magnetism with ultracold atoms“. PhD thesis. Ruprecht-Karls-Universität Heidelberg, 2015 (cit. on p. 13).

[Ols98] M. Olshanii. „Atomic Scattering in Presence of an External Confinement and a Gas of Impenetrable Bosons“. In: *Physical review letters* 81.5 (1998), p. 5. DOI: 10.1103/PhysRevLett.81.938 (cit. on pp. 6–8).

[Omn10] OmniVision. *OV5647. 5-megapixel product brief*. 02/08/2010. URL: http://www.ovt.com/uploads/parts/OV5647.pdf (visited on 08/08/2016) (cit. on p. 37).

[Pru+08] C. Pruss, E. Garbusi, and W. Osten. „Testing Aspheres“. In: *Optics and Photonics News* 19.April (2008), pp. 24–29. DOI: 10.1364/OPN.19.4.000024 (cit. on p. 27).

[Qui+09] J. Quintanilla and C. Hooley. „The strong-correlations puzzle“. In: *Physics World* 22.6 (2009), pp. 32–37 (cit. on p. 1).

[Sak+11] J. J. Sakurai and J. Napolitano. *Modern quantum mechanics*. 2. ed., international ed. Boston [u.a.]: Addison-Wesley, 2011, XVIII, 550 S. (Cit. on pp. 10, 12).

[Sal+07] B. E. A. Saleh and M. C. Teich. *Fundamentals of photonics*. eng. 2. ed. Wiley series in pure and applied optics. Hoboken, N.J.: Wiley, 2007, XIX, 1177 S. (Cit. on pp. 19, 20, 25, 26).

[Sam15] Samsung Electronics Company. *Samsung Announces Mass Production of Industry's First Mobile Image Sensor with* 1.0 µm *Pixels*. 07/29/2015. URL: https://news.samsung.com/global/samsung-announces-mass-production-of-industrys-first-mobile-image-sensor-with-1-0%CE%BCm-pixels (visited on 08/15/2016) (cit. on p. 37).

[Ser+11] F. Serwane, G. Zurn, T. Lompe, T. B. Ottenstein, A. N. Wenz, and S. Jochim. „Deterministic Preparation of a Tunable Few-Fermion System“. In: *Science* 332.6027 (2011), pp. 336–338. DOI: 10.1126/science.1201351 (cit. on pp. 14, 17).

[Ser07] F. Serwane. „The setup of a Magneto Optical Trap for the preparation of a mesoscopic degnerate Fermi gas“. Diploma Thesis. Ruprecht-Karls-Universität Heidelberg, 2007 (cit. on p. 14).

[Ser11] F. Serwane. „Deterministic preparation of a tunable few-fermion system“. PhD thesis. Ruprecht-Karls-Universität Heidelberg, 2011 (cit. on pp. 13, 18).

[Son14] Sony Corporation. *IMX219PQ. Diagonal 4.6 mm (Type 1/4.0) 8.08M-Effective Pixel Color CMOS Image Sensor.* 04/25/2014. URL: http://www.sony.net/Products/SC-HP/new_pro/april_2014/imx219_e.html (visited on 08/16/2016) (cit. on p. 37).

[Swe90] W. C. Sweatt. „Rotatable shear plate interferometer“. In: *Optical Engineering* 29.9 (1990), pp. 1157–1160 (cit. on p. 35).

[Upt16] E. Upton. *New 8-megapixel camera board on sale at $25.* Raspberry Pi Foundation. 04/25/2016. URL: https://www.raspberrypi.org/blog/new-8-megapixel-camera-board-sale-25/ (visited on 08/16/2016) (cit. on p. 37).

[Wen+13] A. N. Wenz, G. Zurn, S. Murmann, I. Brouzos, T. Lompe, and S. Jochim. „From Few to Many: Observing the Formation of a Fermi Sea One Atom at a Time“. In: *Science* 342.6157 (2013), pp. 457–460. DOI: 10.1126/science.1240516 (cit. on p. 2).

[Wen13] A. N. Wenz. „From Few to Many: Ultracold Atoms in Reduced Dimensions“. PhD thesis. Ruprecht-Karls-Universität Heidelberg, 2013 (cit. on pp. 5, 8, 12, 13, 16, 55).

[Zür+13] G. Zürn, T. Lompe, A. N. Wenz, S. Jochim, P. S. Julienne, and J. M. Hutson. „Precise characterization of Li6 Feshbach resonances using trap-sideband-resolved RF spectroscopy of weakly bound molecules“. In: *Physical Review Letters* 110.13 (2013), pp. 1–5. DOI: 10.1103/PhysRevLett.110.135301 (cit. on p. 12).

[Zür12] G. Zürn. „Few-fermion systems in one dimension“. PhD thesis. Ruprecht-Karls-Universität Heidelberg, 2012 (cit. on pp. 5, 7, 8, 13, 15).

COLOPHON

This thesis has been typeset, using the open source font family *Linux Libertine* by Philipp H. Poll, provided by the LaTeXpackage *libertine* by Bob Tennent.

http://www.linuxlibertine.org/

Style and layout are based on the LaTeX template *classicthesis* by André Miede, that is inspired by Robert Bringhurst's basic work *The Elements of Typographic Style*.

https://bitbucket.org/amiede/classicthesis/

All graphics have been created using *Inkscape*, if no other source is given, and all plots have been done using Python with the modules *matplotlib* and *numpy*.

Master thesis Version 160929, rev1, compiled on September 29, 2016, (classicthesis 4.2).

ERKLÄRUNG

Ich versichere, dass ich diese Arbeit selbstständig verfasst und keine anderen als die angegebenen Quellen und Hilfsmittel benutzt habe.

Heidelberg, 27 September 2016

Michael Dehabe